VAPOR CONDENSATION ON TURBULENT LIQUID

by

J. Steven Brown

B.M.E. Georgia Institute of Technology
(1987)

SUBMITTED TO THE DEPARTMENT OF MECHANICAL
ENGINEERING IN PARTIAL FULFILLMENT OF THE
REQUIREMENTS FOR THE DEGREE OF

DOCTOR OF PHILOSOPHY

at the

MASSACHUSETTS INSTITUTE OF TECHNOLOGY

May, 1991

Signature of Author ________
Department of Mechanical Engineering
May, 1991

Certified by ________________________________
Ain A. Sonin
Professor, Mechanical Engineering
Thesis Supervisor

Accepted by ________________________________
Ain A. Sonin
Chairman, Departmental Committee on Graduate Studies
Department of Mechanical Engineering

VAPOR CONDENSATION ON TURBULENT LIQUID

by

J. Steven Brown

Submitted to the Department of Mechanical Engineering
on May 15, 1991 in partial fulfillment of the requirements for
the degree of Doctor of Philosophy

Abstract

An empirical correlation is presented for the condensation of pure vapor on a subcooled, turbulent liquid with a shear-free interface. The correlation expresses the dependence of the condensation rate on fluid properties, on the liquid-side turbulence (which is imposed from below), and on the effects of buoyancy in the interfacial thermal layer. Both the liquid-side turbulence and the condensation heat transfer process are in statistically steady states. The correlation is derived from experiments with steam and water, but under conditions which simulate typical cryogenic fluids.

The steady state condensation rate correlation is then used to predict the condensation rate in three different systems: (1) a cylindrical system with turbulent mixing provided by an axial submerged jet for submergences ranging from 0.5D to 4.2D, (2) a channel flow with grid-induced turbulence and (3) a cylindrical system with turbulent mixing provided by an axial submerged jet, when the liquid-side turbulence and the condensation heat transfer process are not in statistically steady states.

Lastly, the critical Reynolds at which a liquid-into-liquid axisymmetric submerged jet, such as those in the systems studied above for jet submergences up to approximately 100 nozzle diameters, undergoes transition from laminar to turbulent flow is experimentally investigated. Fully laminar jets can be maintained up to Reynolds numbers of several hundred ($Re_n \sim 600$) and fully turbulent jets occur at Reynolds numbers of $Re_n > 2500$. For the intermediate Reynolds number range, the jet passes a certain distance (typically between about 5d and 40d) into the liquid as a smooth jet before breaking up into a fully turbulent jet.

Thesis Supervisor: Dr. Ain A. Sonin
Title: Professor of Mechanical Engineering

Table of Contents

Abstract 2

Table of Contents. 3

List of Figures 5

List of Tables 9

Acknowledgements 10

Part I 12

- Nomenclature 13
- 1.1 Introduction 15
- 1.2 Test Cell 17
- 1.3 Turbulence Calibration 21
  - 1.3.1 Video Measurements of Centerline Turbulence Intensity for Large Nozzle Submergences 21
  - 1.3.2 Laser Doppler Velocimetry (LDV) Measurements for Large Nozzle Submergences 24
    - 1.3.2.a Centerline Turbulence Intensity 25
    - 1.3.2.b Radial Turbulence Intensity 28
    - 1.3.2.c Turbulence Macroscale 30
    - 1.3.2.d Turbulence Spectra. 33
  - 1.3.3 Conclusions. 37
- 1.4 Condensation Rate Measurement. 37
- 1.5 Scaling Relations. 41
- 1.6 An Analysis. 51
- 1.7 Condensation Rate Correlation. 57
- 1.8 Concluding Remarks. 71
- References. 76

Part II. 85

- Nomenclature. 86
- 2.1 Introduction. 88
- 2.2 Local Condensation Rate Correlation. 89
- 2.3 Condensation Rate Correlation for Axial Jet System. 91
  - 2.3.a High Nozzle Submergence. 93

2.3.b Low Nozzle Submergence. 94
2.3.c General Correlation. 97
2.4 Comparison with Experiment. 98
2.4.a Thomas' Data. 98
2.4.b The Present Data. 100
2.5 Condensation in Horizontal Channel. 105
2.6 Test Cell for Transient Condensation Experiments. 107
2.7 Scaling Relations for Transient Condensation Experiments. 111
2.8 Transient Condensation Results. 116
2.9 Concluding Remarks. 126
References. 127
Appendix 2.A. 129
Part III. 134
Nomenclature. 135
3.1 Introduction. 136
3.2 Test Cell. 137
3.3 Present Experiments. 138
3.4 Comparison with Other Work. 144
3.5 Conclusions. 149
References. 150

List of Figures

1.1 Schematic of Test cell. 18

1.2 Flow rate calibration. Including data from Helmick (1988). 20

1.3 Calibration of turbulence intensity at centerline of test cell. 23

1.4.a Centerline distribution of r.m.s. fluctuating velocity as a function of depth below the interface for $Re_* = 2.91 \times 10^4$. 26

1.4.b Centerline distribution of r.m.s. fluctuating velocity as a function of depth below the interface for $Re_* = 4.01 \times 10^4$. 26

1.4.c Centerline distribution of r.m.s. fluctuating velocity as a function of depth below the interface for $Re_* = 5.77 \times 10^4$. 27

1.5 R.m.s. and mean horizontal velocities as functions of r at a depth of 0.5 cm below the interface for $Re_* = 4.01 \times 10^4$. 29

1.6.a Eulerian time correlation of the horizontal velocity at the centerline at a depth of 3 cm below the interface for $Re_* = 2.5 \times 10^4$. 31

1.6.b Eulerian time correlation of the vertical velocity at the centerline at a depth of 3 cm below the interface for $Re_* = 2.5 \times 10^4$. 31

1.6.c Eulerian time correlation of the horizontal velocity at the centerline at a depth of 3 cm below the interface for $Re_* = 5.03 \times 10^4$. 32

1.6.d Eulerian time correlation of the vertical velocity at the centerline at a depth of 3 cm below the interface for $Re_* = 5.03 \times 10^4$. 32

1.7.a Eulerian time spectrum of the horizontal velocity at the centerline at a depth of 3 cm below the interface for $Re_* = 2.5 \times 10^4$. 35

1.7.b Eulerian time spectrum of the vertical velocity at the centerline at a depth of 3 cm below the interface for $Re_* = 2.5 \times 10^4$. 35

1.7.c Eulerian time spectrum of the horizontal velocity at the centerline at a depth of 3 cm below the interface for $Re_* = 5.03 \times 10^4$. 36

1.7.d Eulerian time spectrum of the vertical velocity at the centerline at a depth of 3 cm below the interface for $Re_* = 5.03 \times 10^4$. 36

1.8 The effect of steam superheat on the condensation rate measurement. A modest steam superheat eliminates condensation from occurring upstream of the interface. 39

1.9 Data reproducibility checked by repeating a standard test at the beginning and end of each day for ten days. 41

1.10.a Distribution of r.m.s. velocity. Definition of bulk velocity. 43

1.10.b Distribution of mean temperature. Definition of bulk temperature. 43

1.10.c Distribution of turbulent diffusivity. Definition of bulk turbulent

diffusivity. 43
1.11 Viscosity as a function of temperature for water. 46
1.12 Viscosity as a function of temperature for liquid hydrogen. 46
1.13 Condensation mass flow rate vs turbulence intensity for steam and water at $Pr_b = 4.65$ ($T_b = 37°C$). 60
1.14.a Reduced Stanton number vs Reynolds number for $Pr_b = 4.65$. See Table 1.2 for symbols. 61
1.14.b Reduced Stanton number vs Reynolds number for $Pr_b = 3.15$. See Table 1.2 for symbols. 61
1.14.c Reduced Stanton number vs Reynolds number for $Pr_b = 2.55$. See Table 1.2 for symbols. 62
1.14.d Reduced Stanton number vs Reynolds number for $Pr_b = 2.2$. See Table 1.2 for symbols. 62
1.14.e Reduced Stanton number vs Reynolds number for $Pr_b = 1.5$. See Table 1.2 for symbols. 63
1.15.a Reduced Stanton number vs Richardson number for $Pr_b = 4.65$. See Table 1.2 for symbols. 64
1.15.b Reduced Stanton number vs Richardson number for $Pr_b = 3.15$. See Table 1.2 for symbols. 64
1.15.c Reduced Stanton number vs Richardson number for $Pr_b = 2.55$. See Table 1.2 for symbols. 65
1.15.d Reduced Stanton number vs Richardson number for $Pr_b = 2.2$. See Table 1.2 for symbols. 65
1.15.e Reduced Stanton number vs Richardson number for $Pr_b = 1.5$. See Table 1.2 for symbols. 66
1.16 Reduced Stanton number vs Richardson number. See Table 1.2 for symbols. 66
1.17 Reduced Stanton number, extrapolated to $Ri \rightarrow 0$, vs bulk Prandtl number. 69
1.18 Condensation Stanton number as a function of Jakob number. Data obtained by varying saturation temperature. See Table 1.3 for test conditions. 70
2.1 Axial jet system with large jet submergence ($s/D > 3$). 92
2.2 Axial jet system with small jet submergence ($s/D < 1.3$). 92
2.3.a Thomas's axial jet system with $s/D = 1.30$. Solid line represents equation (2.20) with $\beta_1 = 0.16$ and $\beta_2 = 0.20$. 101

2.3.b Thomas's axial jet system with s/D = 1.13. Solid line represents equation (2.20) with $\beta_1 = 0.16$ and $\beta_2 = 0.20$. 101

2.3.c Thomas's axial jet system with s/D = 0.97. Solid line represents equation (2.20) with $\beta_1 = 0.16$ and $\beta_2 = 0.20$. 102

2.3.d Thomas's axial jet system with s/D = 0.73. Solid line represents equation (2.20) with $\beta_1 = 0.16$ and $\beta_2 = 0.20$. 102

2.3.e Thomas's axial jet system with s/D = 0.50. Solid line represents equation (2.20) with $\beta_1 = 0.16$ and $\beta_2 = 0.20$. 103

2.3.f Thomas's axial jet system with s/D = 0.32. Solid line represents equation (2.20) with $\beta_1 = 0.16$ and $\beta_2 = 0.20$. 103

2.4 "Universal" submerged jet correlation. 104

2.5 Thomas' horizontal channel flow with grid-induced turbulence. Solid line represents equations (2.1) and (2.2) with average turbulence intensity taken as $0.13U_g$. 106

2.6 Schematic of test cell. 108

2.7 Differential pressure transducer calibration. 110

2.8 Flow rate calibration. 111

2.9 Broken line is a typical trace of system pressure vs. time when the wall heaters were not used and solid line is the predicted curve calculated using equation (2.25) with $\dot{Q} = 0$. See Tables 2.1 and 2.2 for conditions. 118

2.10 Experiment of Figure 2.9 repeated with the wall heaters turned on. See Tables 2.1 and 2.2 for conditions. 118

2.11 Data of Figure 2.10 where the predicted pressure curve has been corrected using equation (2.32). See Tables 2.1 and 2.2 for conditions. . 122

2.12 Data of Figure 2.11 plotted as $\dot{m}_{av}$ vs. time. See Tables 2.1 and 2.2 for conditions. 122

2.13 Broken line is a typical system pressure vs. time for $\Delta T \cong 38°C$. Solid line is the predicted pressure curve corrected using equation (2.32). See Tables 2.1 and 2.2 for conditions. 123

2.14 Data of Figure 2.13 plotted as $\dot{m}_{av}$ vs. time. See Tables 2.1 and 2.2 for conditions. 123

2.15 Broken line is a typical system pressure vs. time for $\Delta T \cong 6°C$. Solid line is the predicted pressure curve corrected using equation (2.32). See Tables 2.1 and 2.2 for conditions. 124

2.16 Data of Figure 2.15 plotted as $\dot{m}_{av}$ vs. time. See Tables 2.1 and 2.2 for conditions. 124

2.17 Broken line is another typical system pressure vs. time for $\Delta T \cong 38°C$. Solid line is the predicted pressure curve corrected using equation (2.32).

See Tables 2.1 and 2.2 for conditions. 125

2.18 Data of Figure 2.17 plotted as $\dot{m}_{av}$ vs. time. See Tables 2.1 and 2.2 for conditions. 125

3.1 Schematic of test cell. 137

3.2 Fully laminar jet issuing from "long" nozzle with $Re_n \cong 460$, $D/d = 48$ and $s/D = 1.0$. Distance between markings on scale: 1 cm. 140

3.3 Semi-turbulent jet issuing from "long" nozzle with $Re_n \cong 1550$, $D/d = 48$ and $s/D = 1.0$. Distance between markings on scale: 1 cm. 141

3.4 Fully turbulent jet issuing from "long" nozzle with $Re_n \cong 5980$, $D/d = 48$ and $s/D = 1.0$. Distance between markings on scale: 1 cm. 142

3.5 Laminar length vs. Reynolds number for "short" nozzles. 143

3.6 Laminar length vs. Reynolds number for "long" nozzles. 143

3.7 Intermittency at $Re_n \cong 1990$, $D/d = 24$ and $s/D = 1.0$. Time between frames approximately 0.25 seconds. Distance between markings on scale: 1 cm. 145

List of Tables

1.1 LDV measurements of integral time scale ($\bar{t}$) and integral length scale ($\Lambda = v\bar{t}$) in 15.3 cm diameter test cell at a depth of 3 cm below the interface. v and $\bar{t}$ are based on centerline values. 34
1.2 Test matrix for condensation tests (see Figures 1.14 – 1.16). 59
1.3 Test conditions for Figure 1.18. 70
1.4 Raw data for Figures 1.14 – 1.16. 80
2.1 Initial conditions for Figures 2.9 – 2.18. 117
2.2 τ_c/τ_{mix} for Figures 2.9 – 2.18. 117
2.3 Raw data for Figure 2.4. 133

Acknowledgements

My deepest thanks go to my advisor Professor Ain A. Sonin. Without his help and guidance I would never have been able to complete this work. What I know about fluid mechanics I attribute to him. His incredible ability to model a complicated problem simply and to ask the right questions has truly been an inspiration to me. Lastly, I must recognize his outstanding abilities as an instructor. I had the extreme fortune of having had Professor Sonin as an instructor in two fluid mechanics courses and I also served as a teaching assistant for his turbulence course.

I thank the other members of my committee, Professors Anthony Patera and Bora Mikic, for their guidance and suggestions.

I thank in a special way Boo-Cheong Khoo, Mike Helmick and Professor Sonin. This thesis draws heavily from two papers co-authored with them: J. Steven Brown, Boo-Cheong Khoo and Ain A. Sonin, "Rate Correlation for Condensation of Pure Vapor on Turbulent, Subcooled Liquid," *International Journal of Heat and Mass Transfer*, Vol. 33, pp. 2001-2018, 1990 and J.S. Brown, M.R. Helmick and A.A. Sonin, "Vapor Condensation at a Turbulent Liquid Surface in Systems with Possible Space-Based Applications," AIAA-Paper 89-2846, 1989. The LDV results presented here in Section 1.3.2 are taken from Boo-Cheong Khoo's thesis. The contribution of Mike Helmick to the second paper does not appear here in this thesis.

I would like to acknowledge the NASA Lewis Research Center who provided support for this research under Grant NAG3-731, and the contract monitors: J.C. Aydelott, D.M. DeFelice and M.M. Hasan.

I thank Leslie Regan for her friendship and of course for her knowledge of the intricacies of the M.I.T. bureaucracy and how to circumvent them.

The members of the fluid mechanics laboratory, both current and former, have made my stay here much more enjoyable. In particular I would like to acknowledge Mike Helmick, Boo-Cheong Khoo, Hamdi Kozlu, Chris Atkinson, Andrew Poutiatine, Andy Shapiro and Sourav Bhunia for teaching me about experimental techniques, but more importantly, for their friendship. I would like to thank my office mates: Jian Shen, Marticia Barsotti and Fuquan Gao for tolerating me. To the other current students in the Fluids Lab who have made the Lab a much more enjoyable place: HL, MC, CM (i.e.

Chris Marx who asked me to specifically mention his name), BS, DO, CW, JS, EO, MW, MG, FE, JF and KF. I thank Dick Fenner for his help in the construction of the experimental apparatus. I thank Claire Sasahara for her help.

I thank my roommates Michal, Piero and Raffaele for everything, but particularly for their friendship.

I thank my brothers and sister for all the great years of growing up together, but especially I thank my parents for their love and support . To them I dedicate this thesis.

To Donatella.

And lastly, I thank God for having giving me all that I have.

Part I

Nomenclature

c_p	specific heat at constant pressure (J kg^{-1} K^{-1})
d	nozzle exit diameter (m)
D	test cell inner diameter (m)
f	frequency (Hz)
g	acceleration due to gravity (m s^{-2})
Gr	Grashof number, equation (1.45)
h_{fg}	latent heat of condensation (J kg^{-1})
Ja	Jakob number, equation (1.23)
k	turbulence intensity in k-ε turbulence model (m^2 s^{-2})
l	turbulence macroscale (m)
L	length scale in k-ε turbulence model, $k^{3/2}/\varepsilon$ (m)
$\dot{m}$	condensation mass flux across interface (kg s^{-1} m^{-2})
Pr	Prandtl number, equation (1.23)
Q	volume flow rate circulating through system, Figure 1.1 (m^3 s^{-1})
r	radial coordinate (m)
R(t)	Eulerian autocorrelation function measured at a fixed point, equation (1.9)
Re	Reynolds number, equation (1.23)
Re_*	system Reynolds number, $Q/d\nu$
Ri	Richardson number, equation (1.23)
s	nozzle submergence, Figure 1.1 (m)
St	Stanton number, equation (1.23)
St_o	Reduced Stanton number, equation (1.34)
t	time (s)
T	absolute temperature (K)
T_b	value of T_B extrapolated to the interface, Figure 1.10.b (K)
T_B	temperature in bulk of liquid, outside the interfacial layer, Figure 1.10.b (K)
T_s	liquid saturation temperature (K)
ΔT	liquid subcooling, $T_s - T_b$ (K)
u_c	condensation induced bulk flow, $\dot{m}/\rho_b$, equation (1.26) (m s^{-1})
v	r.m.s. value of either the horizontal or vertical component of turbulent velocity (m s^{-1})
V	voltage output from pressure transducer (Volts)
v_b	value of v extrapolated from the bulk liquid to the surface disregarding the interfacial layer, Figure 1.10.a (m s^{-1})
y	coordinate measured vertically downward from the surface into the bulk liquid, Figure 1.1 (m)
z	coordinate measured vertically upward from the nozzle exit into the bulk liquid, Figure 1.1 (m)

Greek symbols

α	thermal diffusivity ($m^2\ s^{-1}$)
α_T	turbulent thermal diffusivity ($m^2\ s^{-1}$)
α_{TB}	turbulent thermal diffusivity outside of the thermal layer, Figure 1.10.c ($m^2\ s^{-1}$)
β	coefficient of thermal expansion (K^{-1})
δ	thermal layer thickness (m)
δ_v	viscous layer thickness (m)
ε	viscous dissipation rate in $k\text{–}\varepsilon$ turbulence model ($m^2\ s^{-3}$)
λ	thermal conductivity ($kg\ m\ s^{-3}\ K^{-1}$)
Λ	integral turbulence length scale, equation (1.10) (m)
μ	viscosity ($kg\ m^{-1}\ s^{-1}$)
ν	kinematic viscosity ($m^2\ s^{-1}$)
ρ	density ($kg\ m^{-3}$)
τ	characteristic time (s)
$\phi(Re_*)$	function defined in equation (1.4)
$\Phi(f)$	Eulerian time spectrum, equation (1.12) ($m^2\ s^{-1}$)

Subscripts

b	liquid at bulk temperature (extrapolated to the interface)
g	vapor
s	liquid at saturation temperature

1.1. Introduction

Condensation of pure vapor at a turbulent liquid interface is a liquid-side dependent heat transfer process, the rate being limited by the turbulent transport of the latent heat from the interface to the bulk of the liquid. Theoretically, this is still an unsolved problem, largely because the structure of the turbulence very near the free surface is still open to speculation. At lower turbulence intensities the condensation problem is further complicated by stable thermal stratification at the interface, with attendant turbulence damping. Simplistic models have been proposed for the analogous gas absorption problem, where thermal stratification is absent [Kishinevsky (1955); Levich (1962); King (1966); Fortescue and Pearson (1967); Lamont and Scott (1970); Theofanous et al. (1976); Henstock and Hanratty (1979); Theofanous (1984)]. However, each of these models is tailored largely to specific experimental conditions. The models disagree with each other, and there is no consensus on a unified model which expresses the condensation rate in terms of the local turbulence parameters and fluid properties [e.g. see Sonin et al. (1986)]. Progress toward such a model has been hindered not only by the lack of understanding of the interfacial turbulence structure, but also by the fact that accurate comparison with experiment has been difficult: the turbulence parameters which appear in a general model (e.g. turbulence intensity and turbulence macroscale) have not been directly measured in most investigations of condensation.

Simultaneous data on vapor condensation rate and liquid-side turbulence are relatively scarce. Thomas (1979) made measurements with steam and water in several different systems in which turbulence was imposed on the liquid from below, without shear on the interface. Jensen and Yuen (1982) report measurements in a channel flow in which the liquid-side turbulence was induced largely by interfacial shear from the steam side. Ueda et al. (1977), Mizushina et al. (1978), Komori et al. (1982, 1983), and Ogino (1986) have published significant basic data on the turbulence structure in a channel flow with interfacial heat transfer. They did not, however, report simultaneous measurements of the heat transfer rate at the interface, and their measurements of turbulent diffusivity do not cover the very thin region near the free surface where most of the temperature drop occurs when buoyancy effects are not dominant.

More recently, Sonin et al. (1986) investigated the condensation of pure steam on a shear-free water interface, on which a calibrated turbulence was imposed from below. Using relatively high turbulence intensities where buoyancy effects were negligible, they concluded that the condensation rate could be correlated in terms of a constant Stanton number based on the liquid-side turbulence intensity.

Here a more general empirical correlation for the rate of pure vapor condensation on a turbulent subcooled liquid is presented. The correlation accounts not only for the dependence on the interfacial conditions, but also establishes the dependence on liquid-side Prandtl number and buoyancy. One of the major objectives of this work has been to obtain a rate correlation that can be applied to predict the condensation rate of cryogenic fluids under a broad range of turbulence conditions.

The present work is based on experiments with steam and water, and generalized to other fluids by means of scaling laws (see Section 1.5). The apparatus is similar to the one used by Sonin et al. (1986), but experimental accuracy has been improved, the system has been modified to operate over a range of saturation conditions, and the data correlation is based on more precise information on the turbulence structure in the system (see Section 1.3). The correlation covers the scaling parameters characteristic of most cryogenic fluids, and establishes the dependence of the condensation rate on the liquid and vapor properties, the liquid-side turbulence intensity and turbulence macroscale, and the effects of buoyancy.

1.2. Test Cell

Experiments were performed in a test cell (Figure 1.1) which is geometrically similar to the ones used by Chun (1983), Shimko (1985), Sonin et al. (1986), Helmick (1988) and Khoo (1988). It consists of a pyrex tube of inside diameter D partially filled with a working fluid (tap water in this study) with the fluid's vapor (steam in this study) occupying the rest of the test volume. The water is circulated in a closed loop by means of a centrifugal pump and is cooled (warmed) to the desired operating temperature by means of a tube and shell heat exchanger. A statistically steady turbulence is generated by means of an axisymmetric nozzle of exit diameter d located at a submergence s ($d \ll s$) below the interface. Sufficiently far from the nozzle ($z > 3D$), this system produces an essentially bulk-flow-free turbulence which is approximately isotropic in a horizontal plane but decays with increasing elevation z from the nozzle. The turbulence integral length scale is "locked" to the tube diameter (see Section 1.3) and can be controlled via the system size. All the condensation measurements reported

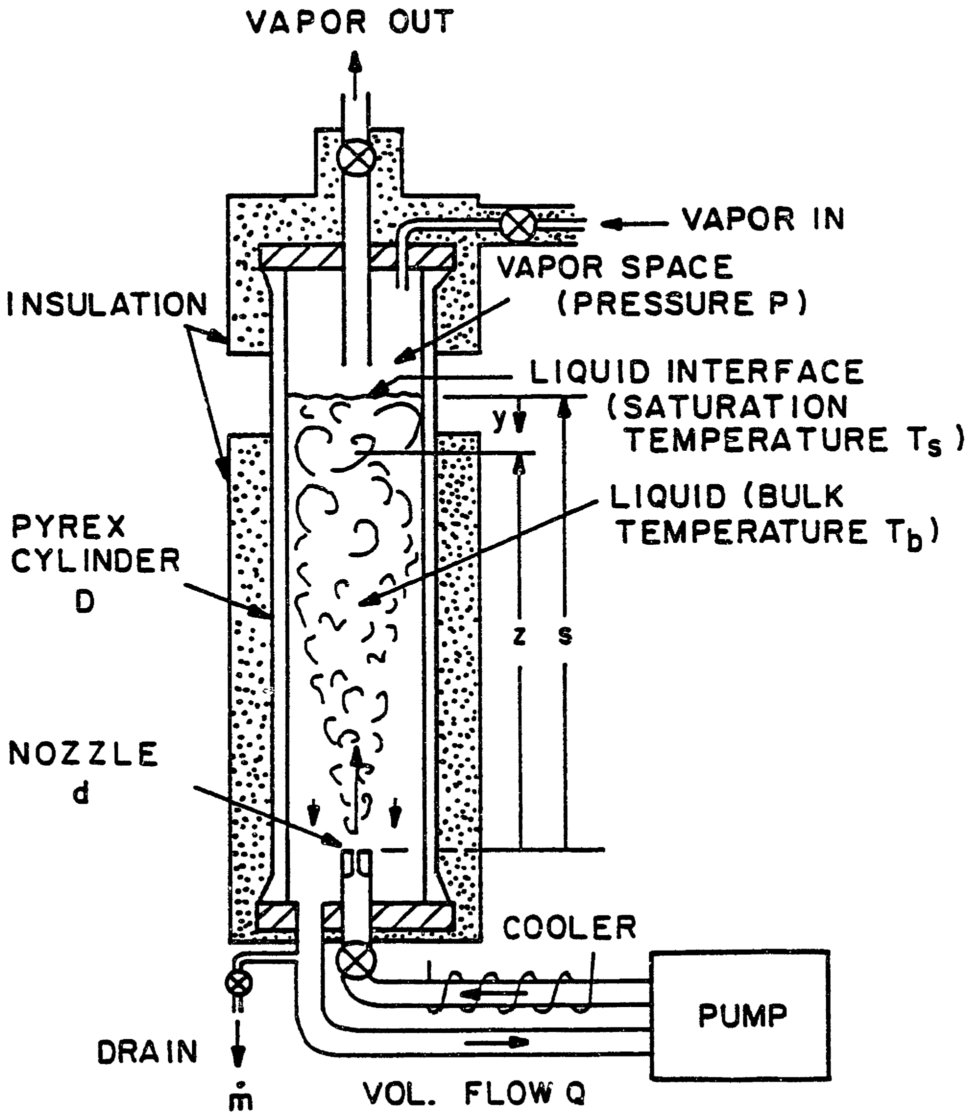

Figure 1.1. Schematic of test cell.

here were made with the water elevation at 3.67 system diameters above the nozzle exit, i.e. with $s/D = 3.67$.

Two different cells were used for the condensation tests, with diameters D of 3.8 cm and 10.2 cm and nozzle exit diameters d of 0.16 cm and 0.42 cm, respectively, so that the ratio D/d was 24 as in the previous studies. A larger 15.3 cm diameter cell was used for the turbulence measurements taken with a laser Doppler velocimeter. The smaller systems were needed to obtain the higher pressures and temperatures at which water has the low Prandtl numbers of liquid cryogens. All three test cells were geometrically similar, including the nozzle diameter (D/d = 24) and the nozzle geometry (length/d = 6.3, with the inlet lip rounded with a radius of curvature of approximately 0.5d).

Pure steam was taken from the M.I.T. steam supply and admitted to the test cell and was allowed to exhaust slowly from the cell via a central port located near the interface. The steam was passed through a commercial steam-water separator and into a 75 dm^3 settling tank before being routed to the test cell. The settling tank was vented slowly at the bottom to help remove residual moisture, air, etc. All parts of the steam supply system, from upstream of the settling tank to the top part of the test cell, were heated with strip heaters and insulated. Operating pressures ranged from 0.11 to 0.37 MPa, corresponding to saturation temperatures from 103 to 141°C, and bulk water temperatures ranged from 37 to 118°C.

Type T (copper-constantan) thermocouples enclosed in inconel sheaths (diameter 0.16 cm) with an accuracy of ±0.5 K were used to measure both the water and steam temperatures. A Bourdon tube gauge (0.1 - 0.79 MPa) was used to measure the system pressure.

The volume flow rate Q circulating through the nozzle was measured using a differential pressure transducer whose output was directly proportional to the pressure drop across the nozzle. Figure 1.2 shows the results of the calibration and the data can be fitted with

$$\frac{Q}{Dd} = 0.196\sqrt{V} \tag{1.1}$$

where V is the output of the transducer in volts and Q/Dd has units of m/s.

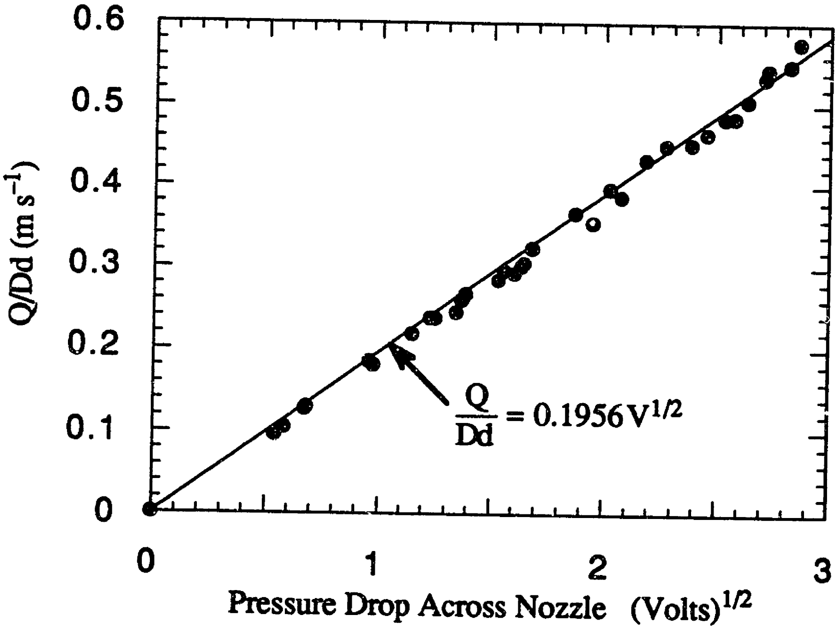

Figure 1.2. Flow rate calibration. Including data from Helmick (1988).

1.3. Turbulence Calibration

1.3.1. *Video Measurements of Centerline Turbulence Intensity for Large Nozzle Submergences*

Consider the turbulent flow field in the liquid at an elevation z which is sufficiently far from the nozzle to be in the far field of the jet (i.e. $z \gg d$), but not so close to the surface that z is in the interfacial layer. Sonin et al. (1986) argued that, at the high Reynolds numbers where the jet is fully turbulent, the r.m.s. value v of a component of the velocity fluctuation will obey the scaling law

$$v(r,z) = \frac{Q}{Dd} f(Re_*, r/D, z/D) \tag{1.2}$$

where Q is the volume flow rate circulating through the nozzle, and

$$Re_* = \frac{Q}{d\nu} \tag{1.3}$$

is a system Reynolds number based on the characteristic flow speed Q/Dd. Experiments showed that at $3.1 < z/D < 4.2$, the r.m.s. velocity near the system centerline is given by

$$v(0,z) \cong \phi(Re_*) \frac{Q}{Dd} \exp(-1.2z/D) \tag{1.4}$$

Sonin et al. (1986) seeded the flow with 3 mm diameter polypropylene beads (specific gravity 0.91), filmed the ensuing motion at 120 frames per second using a high speed video camera, and deduced the vertical and horizontal velocity components of the particles by measuring particle displacements between successive frames. Their measurements in a 15.3 cm diameter cell showed that $\phi(Re_*) \cong 21.8$ for $Re_* > 2.5 \times 10^4$. Data taken in a 3.8 cm diameter cell at lower Reynolds numbers indicated higher values of $\phi(Re_*)$, of the order 30 – 35, suggesting that $\phi(Re_*)$ increases at lower Reynolds numbers. The nozzle in their smaller cell was, however, not exactly similar in length and inlet shape to the one in the larger, and the seed particles were fairly sizable (8% of D) relative to the smaller cell's diameter.

The video measurements have been repeated in a 3.8 cm cell which is completely similar to the larger one, using smaller polystyrene beads (average diameter 0.4 mm, actual diameter 0.1 – 0.8 mm) with specific gravity 1.05. The high speed video camera was focused on the test cell axis and data were taken near the centerline, in a "window" with horizontal boundaries at $z/D = 3.67 \pm 0.13$ and vertical boundaries at $r/D = \pm 0.13$. The interface was set at a height $s/D = 5.8$, i.e. well above the test window, so that the velocity measurements would represent data in the bulk of the liquid far below the interface.

Figure 1.3 shows data for the r.m.s. values of the fluctuating vertical and horizontal velocity components, expressed in the dimensionless form $\phi(Re_*)$ defined by equation (1.4). The new data for the smaller system are in the region $Re_* < 2.5 \times 10^4$; the data for $Re_* > 2.5 \times 10^4$ are those taken by Sonin et al. in their larger system. Each point in the new data set is derived from a minimum of 200 velocity measurements, vs. 60 in the

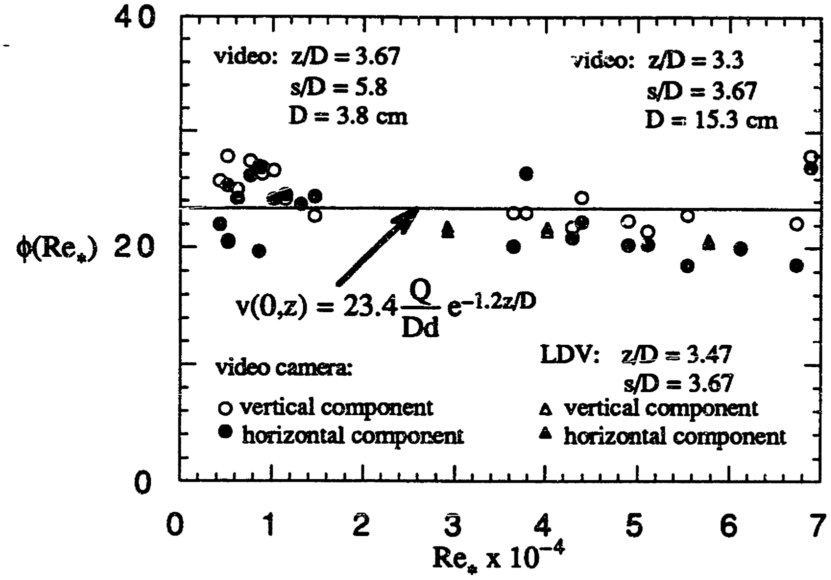

Figure 1.3. Calibration of turbulence intensity at centerline of test cell.

data of Sonin et al.

The new data do not show a clear rise in $\phi(Re_*)$ at lower system Reynolds numbers. The average value based on all data points in both data sets is

$$\phi(Re_*) \cong 23.4 \quad \left(4 \times 10^3 < Re_* < 7 \times 10^4\right) \tag{1.5}$$

The standard deviation of the data is 2.70, or 12% of the mean, which is reasonably consistent with the inverse square root of the number of measurements on which each data point is based. Taken separately, the lower Reynolds number data set does show a somewhat higher average value of $\phi(\mathrm{Re}_*)$ than the higher Reynolds number set, 24.5 vs. 21.8. This might suggest a slight decline in $\phi(\mathrm{Re}_*)$ with increasing Re_*. However, the difference is within the standard deviation of the data taken as a whole, and equation (1.5) is adopted in what follows.

The r.m.s. values of the vertical and horizontal fluctuating velocities differ by less than one standard deviation of the data scatter. The mean velocity components were found to be smaller than the standard deviation of the r.m.s. values. In the new data set, the average mean horizontal velocity was 0.7 cm s^{-1}, while its standard deviation was 0.9 cm s^{-1}. This is to be compared with an average r.m.s. fluctuating velocity component of 9 cm s^{-1}. The average value of the mean vertical velocity measurements was 0.5 cm s^{-1} (downward), with a standard deviation of 0.5 cm s^{-1}. The data are thus consistent with the view that at higher elevations ($z/D > 3$, say), turbulent fluctuations dominate over any remaining mean circulatory flow, and the turbulence is approximately isotropic.

1.3.2. *Laser Doppler Velocimetry (LDV) Measurements for Large Nozzle Submergences*

Laser Doppler velocimetry [the LDV measurements were performed by Khoo (1988)] was used in a cell which was essentially identical to the larger ($D = 15.3$ cm) one of the two used by Sonin et al. (1986) except that a flat plexiglass window was mounted on its side between the elevations $z = 39.5$ and 72.5 cm, at a (minimum) distance of 7.2 cm from the axis. Since the test cell's nominal radius was 7.6 cm, the window did not cause a significant perturbation in the cylindrical geometry.

The LDA was a back-scattered two-color system consisting of a Lexel model 95 ion laser and DISA made optics, with the counter linked to a portable DEC MINC-11 mini-computer. The use of two beam expanders in series resulted in a very small measuring volume, 40 x 40 x 600 μm. Traverses through the cell were made by moving the test cell, which was mounted on a test table with vernier movements in three orthogonal directions as well as rotation in a horizontal plane. The effect of pump vibration on the test cell and the optics was minimized by resting the pump on vibration absorbers and connecting it to the test cell via an 2.4 m long stainless steel flexible hose. Preliminary tests of the LDA system were carried out with the test cell replaced by a plexiglass disc which was filled with water and rotated at a known angular velocity. LDA readings of velocity were recorded with the pump turned off, and were found to agree with the imposed velocity to within 3%. The r.m.s. value of the velocity fluctuations (in this case caused by system noise) was about 5% of the mean. This figure did not change significantly when the centrifugal pump was turned on, which suggested that pump vibration was not a problem.

Aluminum particles of size 3 μm were used as seedlings, which gave a signal-to-noise ratio of about 5; 1μm particles were also tested, but were found to give a poorer signal-to-noise ratio.

1.3.2.a. *Centerline Turbulence Intensity*

Figure 1.4 shows data for the distribution of r.m.s. fluctuating velocity as a

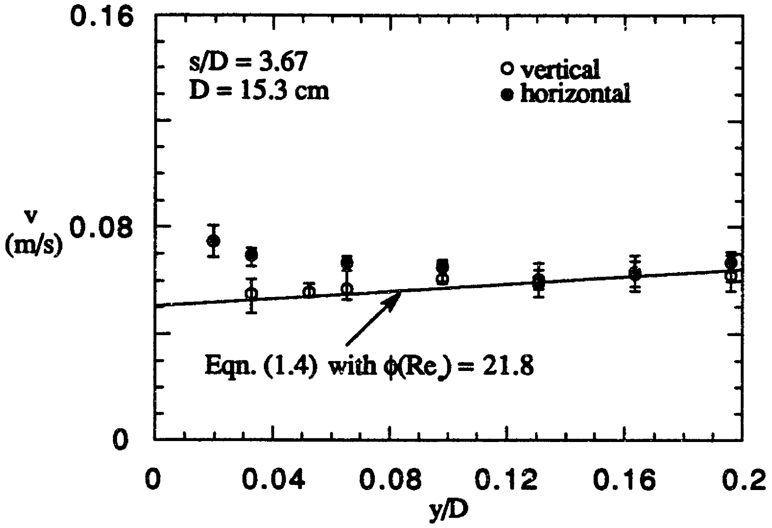

Figure 1.4.a. Centerline distribution of r.m.s. fluctuating velocity as a function of depth below the interface for $Re_* = 2.91 \times 10^4$.

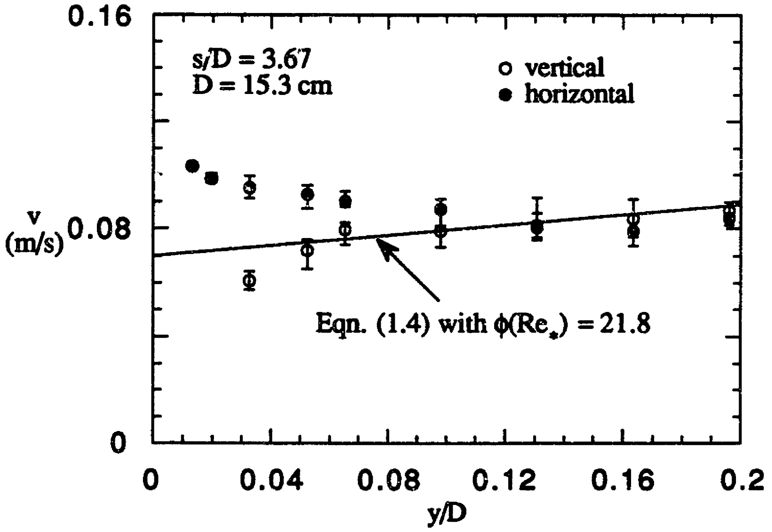

Figure 1.4.b. Centerline distribution of r.m.s. fluctuating velocity as a function of depth below the interface for $Re_* = 4.01 \times 10^4$.

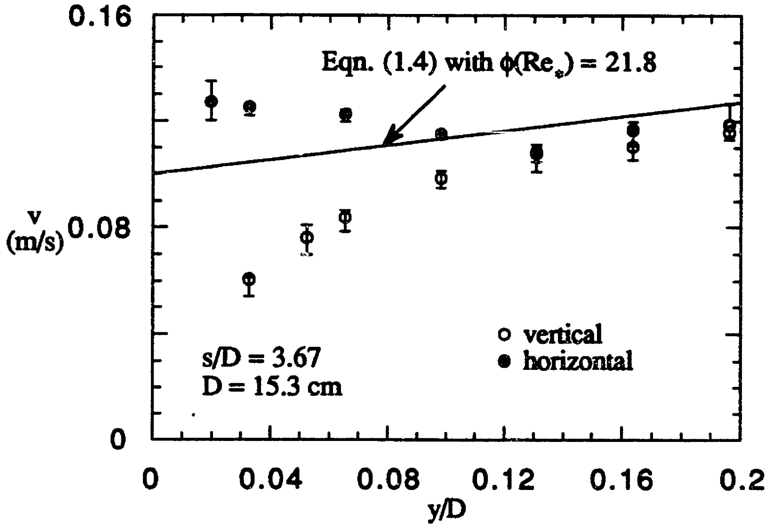

Figure 1.4.c. Centerline distribution of r.m.s. fluctuating velocity as a function of depth below the interface for $Re_* = 5.77 \times 10^4$.

function of depth below the interface, taken along the system's axis. The surface was at an elevation of s/D = 3.67. Each data point is the average of five measurements of r.m.s. velocity, with each measurement derived from 10^4 velocity samples. The bars show the maximum and minimum values of the five measurements. Also shown on the figures is the correlation equation (1.4) with $\phi(Re_*)$ taken as 21.8, the average value of the data taken in this system.

At sufficient depths, the turbulence distribution is approximately isotropic and decays gradually with increasing elevation z (decreasing y), in agreement with equation (1.4). Closer to the surface one enters the interfacial layer, in which the vertical velocity fluctuations are damped (the surface maintained an approximately horizontal state in all these tests) and their kinetic energy is imparted to the velocity components parallel to the surface, which are not constrained at the interface (see also Komori et al., 1982). Figure 1.4 suggests that the interfacial layer has a depth of about 0.1D in this type of system. The mean velocity components are not shown, but are bounded by –0.01 and 0.01 m s^{-1}, that is, they are small compared with the r.m.s. velocity fluctuations.

Figure 1.3 shows six LDV data points for $\phi(Re_*)$. These data points are derived by fitting equation (1.4) to each of the six data sets in Figure 1.4, using only those points which are below the interfacial layer. The results are in reasonably good agreement with $\phi(Re_*) = 21.8$, the average of the video data taken in this system, although they fall somewhat below the line $\phi(Re_*) = 23.4$ which represents the average for all the video data.

1.3.2.b. *Radial Turbulence Intensity*

Figure 1.5 shows an example of both the radial distribution of the horizontal r.m.s. velocity and the mean horizontal velocity taken at a depth of 0.5 cm. The mean horizontal velocity is everywhere less than about 10% of the horizontal r.m.s. velocity, once again supporting the assumption of Sonin et al. of an essentially bulk-flow-free velocity above elevations of $z/D \sim 3$. As expected, the r.m.s. velocity tends to decrease as one approaches the wall. The data in Figure 1.5 can be fitted approximately with

$$v \cong v(0)[1 + 0.06(r/R) - 0.29(r/R)^2] \qquad (1.6)$$

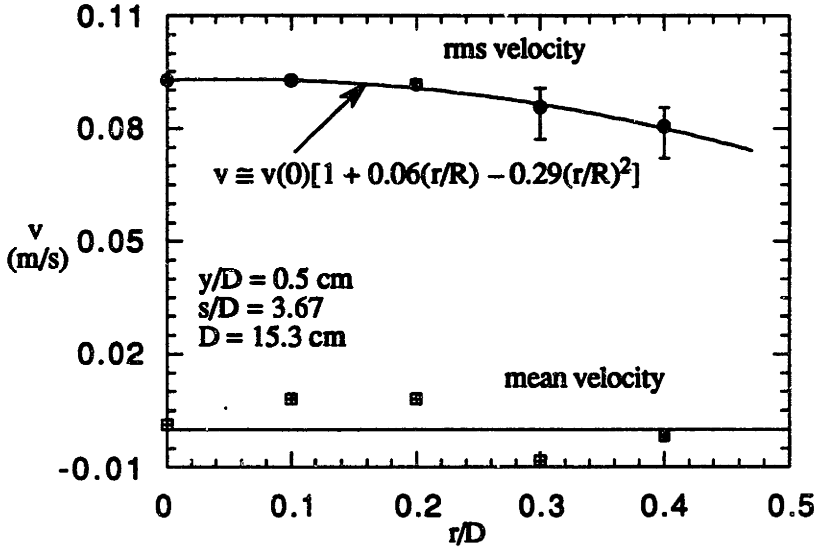

Figure 1.5. R.m.s. and mean horizontal velocities as functions of r at a depth of 0.5 cm below the interface for $Re_* = 4.01 \times 10^4$.

where v(0) is the centerline velocity and $R \equiv D/2$. This equation may be viewed as an "outer" turbulence distribution, analogous to Coles' (1956) "law of the wake" in shear flows and must break down sufficiently close to the wall, where viscous effects must set in. By analogy with shear flows, the viscous layer thickness δ_v near the wall can be estimated from $v(0)\delta_v/\nu \sim 10$, say, where ν is the liquid kinematic viscosity. This yields $\delta_v/R \sim O(10^{-3})$, which suggests that equation (1.6) may be extended fairly close to the wall before a significant departure occurs. Hence, the *average* r.m.s. velocity over the interface can be estimated as

$$v_{av} = \frac{1}{\pi R^2}\int_0^R v 2\pi r dr \cong 0.90 v(0) \tag{1.7}$$

1.3.2.c. *Turbulence Macroscale*

Since the measurements were restricted to a single point at a given time, an integral time scale can be defined as

$$\bar{t} \equiv \int_0^\infty R(t)dt \qquad (1.8)$$

where

$$R(t) \equiv \frac{\langle v'(t'+t)\ v'(t') \rangle}{v^2} \qquad (1.9)$$

is the Eulerian time correlation of the velocity at a given point. Here v' represents the fluctuating component in a particular direction (we shall see that the time scale is approximately independent of the choice of direction), < > represents an ensemble average, and v is the r.m.s. value of v'. An integral length scale can then be defined as

$$\Lambda \equiv (v\bar{t})_{r=0} \qquad (1.10)$$

Figure 1.6 shows some examples of the function R(t) measured at the system centerline at a depth of 3 cm, with the interface at s/D = 3.67. Each correlation was derived from four samples of 10^4 data points each, collected at about 100 Hz. The

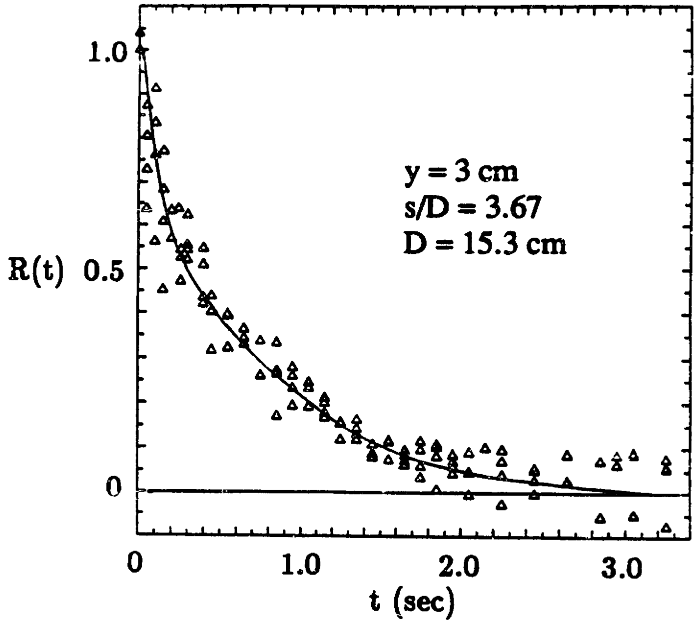

Figure 1.6.a. Eulerian time correlation of the horizontal velocity at the centerline at a depth of 3 cm below the interface for $Re_* = 2.5 \times 10^4$.

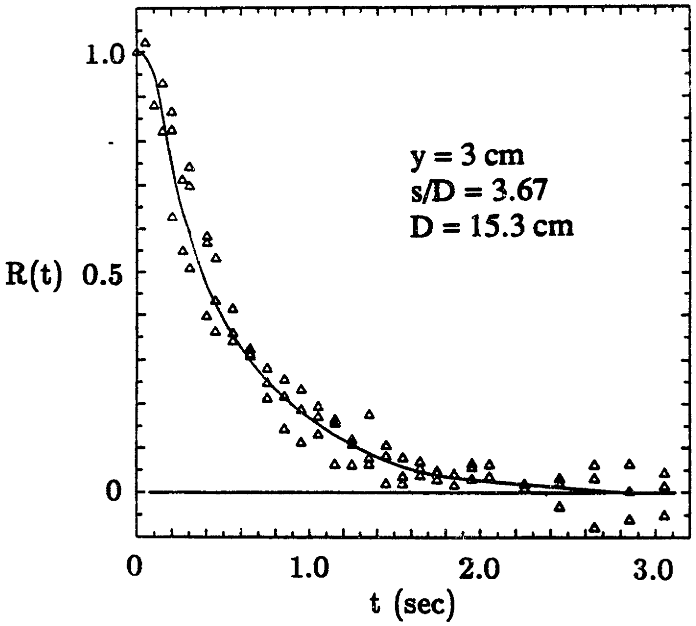

Figure 1.6.b. Eulerian time correlation of the vertical velocity at the centerline at a depth of 3 cm below the interface for $Re_* = 2.5 \times 10^4$.

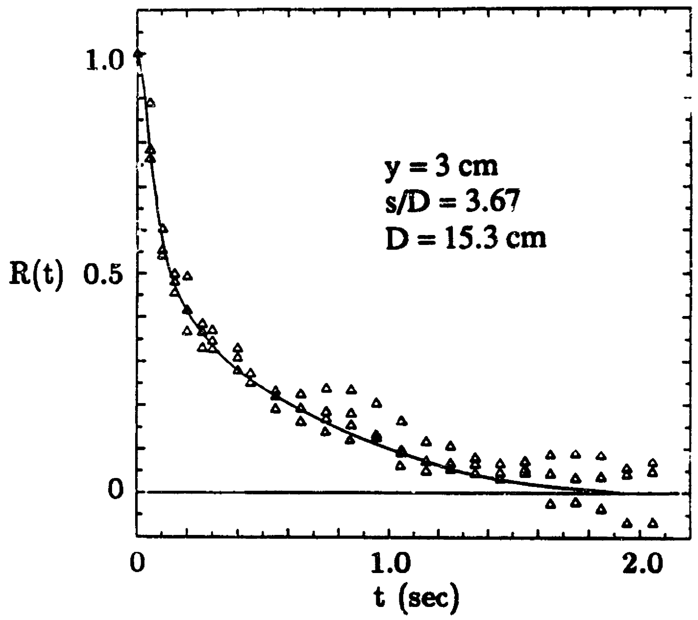

Figure 1.6.c. Eulerian time correlation of the horizontal velocity at the centerline at a depth of 3 cm below the interface for $Re_* = 5.03 \times 10^4$.

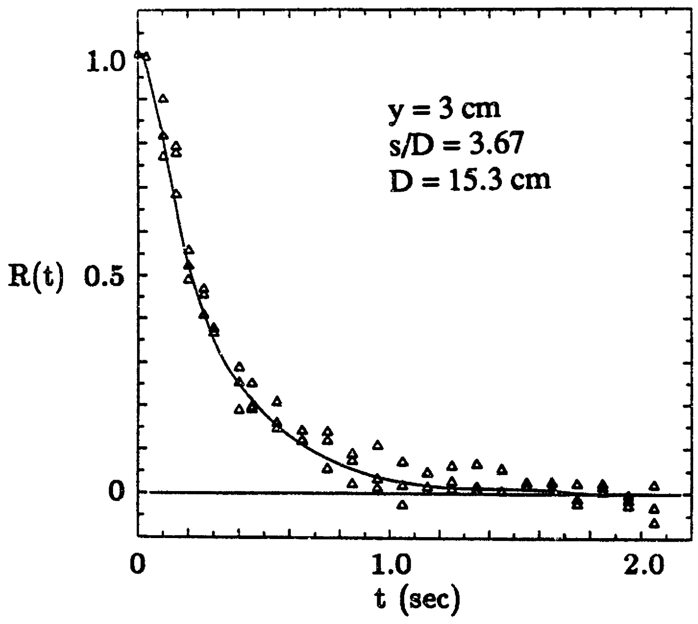

Figure 1.6.d. Eulerian time correlation of the vertical velocity at the centerline at a depth of 3 cm below the interface for $Re_* = 5.03 \times 10^4$.

Doppler frequency counter was adjusted to the "combined mode", so that each Doppler burst yielded only one datum after validation. Table 1.1 summarizes all the results for R(t), $\bar{t}$ and Λ. These data imply that, in the neighborhood z/D ~ 3.5, the integral length scale near the system centerline is approximately independent of Reynolds number, isotropic in direction (at least below the interfacial layer) and given by

$$\Lambda \cong 0.24D \tag{1.11}$$

Equation (1.11) is used as the characteristic macroscale at elevations in the neighborhood of z/D ~ 3.5. Note that the jet spreads to fill the entire cross section of the cell at z/D ~ 3, and that the macroscale should become "locked" to the system diameter at higher elevations. Equation (1.11) should therefore not depend on z.

1.3.2.d. *Turbulence Spectra*

Figure 1.7 shows some examples of Eulerian time spectra which is defined [Tennekes and Lumley (1972)] as

$$\Phi(f) = \int_{-\infty}^{\infty} \exp(-i2\pi f t)\langle v'(t'+t)v'(t')\rangle dt \tag{1.12}$$

where v' is either the vertical or horizontal component of the fluctuating velocity, $i = \sqrt{-1}$ and f is the frequency in hertz.

Table 1.1. LDV measurements of integral time scale ($\bar{t}$) and integral length scale ($\Lambda = v\bar{t}$) in 15.3 cm diameter test cell at a depth of 3 cm below the interface. v and $\bar{t}$ are based on centerline values.

v (m s^{-1})	$\bar{t} \equiv \int_0^\infty R(t)\,dt$ (s)	$\Lambda = v\bar{t}$ (m)
Horizontal components:		
0.062	0.58	0.0360
0.082	0.44	0.0363
0.116	0.34	0.0393
0.160	0.24	0.0283
Vertical components:		
0.062	0.58	0.0360
0.088	0.42	0.0370
0.131	0.31	0.0405
0.191	0.20	0.0382

Average: $\Lambda = 0.0365 \text{ m} \cong 0.24D$

At a given Reynolds number, the spectra of the vertical and horizontal velocity components are approximately identical, consistent with an isotropic turbulence, and

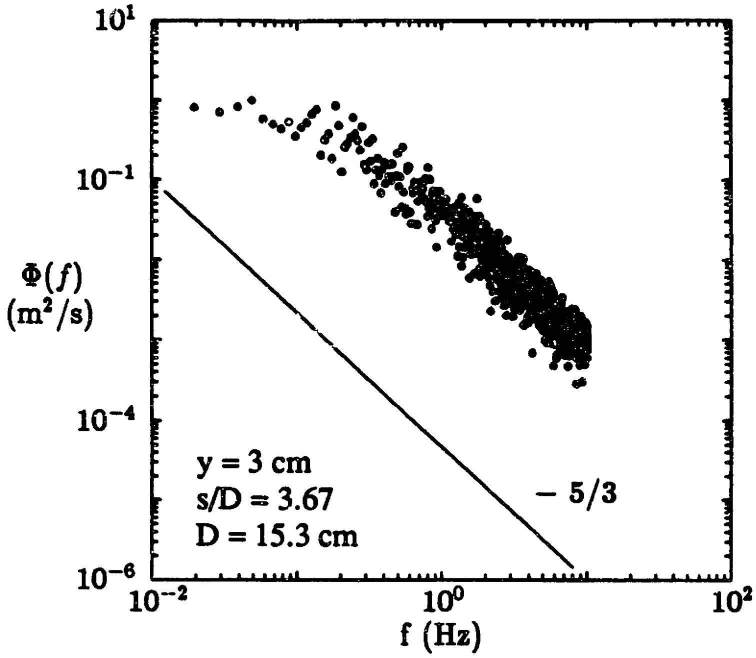

Figure 1.7.a. Eulerian time spectrum of the horizontal velocity at the centerline at a depth of 3 cm below the interface for $Re_* = 2.5 \times 10^4$.

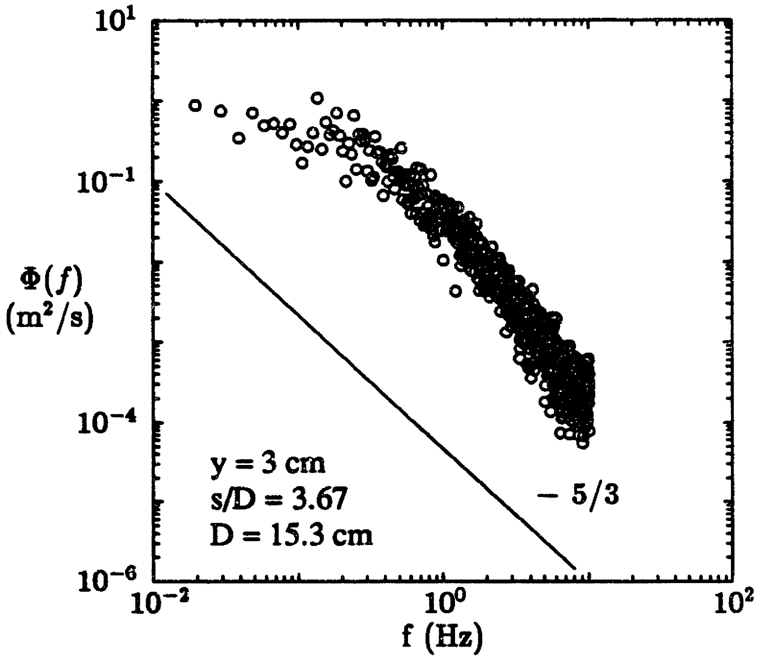

Figure 1.7.b. Eulerian time spectrum of the vertical velocity at the centerline at a depth of 3 cm below the interface for $Re_* = 2.5 \times 10^4$.

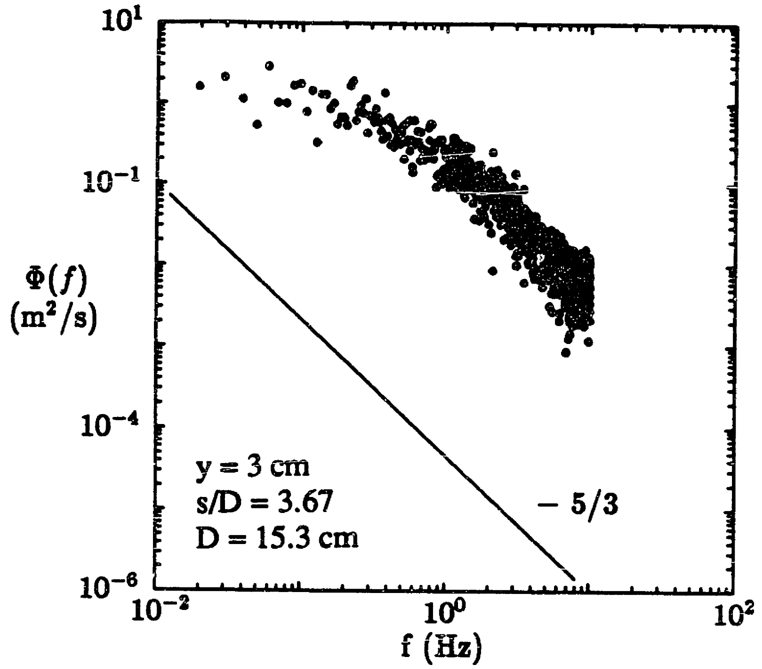

Figure 1.7.c. Eulerian time spectrum of the horizontal velocity at the centerline at a depth of 3 cm below the interface for $Re_* = 5.03 \times 10^4$.

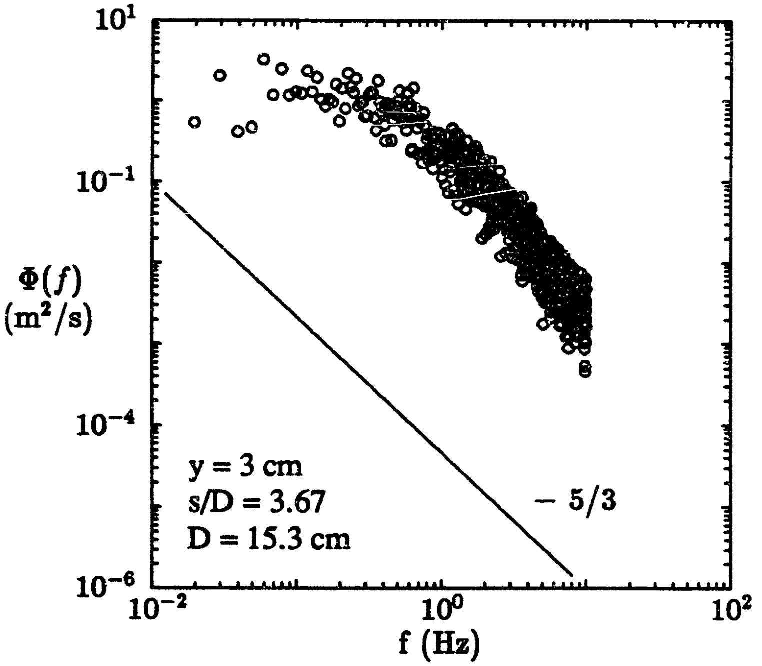

Figure 1.7.d. Eulerian time spectrum of the vertical velocity at the centerline at a depth of 3 cm below the interface for $Re_* = 5.03 \times 10^4$.

decay at high f approximately as $f^{-5/3}$, as expected in the inertial subrange [Tennekes and Lumley (1972)]. The points at which the spectra "break" from the inertial subrange at low frequencies are approximately consistent with the integral time scales of Table 1.1.

1.3.3. *Conclusions*

The turbulence intensity at the centerline of the system of Figure 1.1 is given by equation (1.4), with $\phi(Re_*)$ given in Figure 1.3. A constant value of $\phi(Re_*) \cong 23.4$ provides an adequate fit of the data for $4 \times 10^3 < Re_* < 70 \times 10^3$. Equation (1.4) describes the r.m.s. value v of a single component of the fluctuating velocity at a point below the interfacial layer, where the turbulence is approximately isotropic, and can be used to define an extrapolated value v_b (see Section 1.5) of v from the bulk region to the interface.

The average value of v over the cross section is 0.90 times the centerline value.

In the central region of the test cell, the integral length scale Λ based on the product of v and the Eulerian integral time scale is 0.24D, where D is the system diameter.

1.4. Condensation Rate Measurement

The test cell was operated in steady state, with constant water level, by continuously draining water at a slow rate. To begin with, the condensation rate was measured by two independent methods, a "thermal" method and a "mass" method. The thermal method [Sonin et al. (1986)] is based on measuring the circulating volume flow rate and the temperature rise between the outlet and the inlet, and determining the condensation heat transfer rate from the First Law, assuming negligible heat losses from the sides and bottom of the test section (a good assumption in these tests). The mass method is based on measuring the drainage mass flow rate under steady state conditions, and assuming that it is due entirely to condensation at the interface.

These two methods generally agreed well at the high subcoolings typical of most of the data of Sonin et al. (1986), but were found to depart from each other as the subcooling was decreased (bulk temperature increased), with the discrepancy being somewhat erratic. Part of this discrepancy was traced to the thermistors which were used to measure the temperature difference. A "matched" pair were used as in Sonin et al., but tests showed that the pair tended to become increasingly mismatched as the absolute temperature rose, and errors as large as 30% could result in the measurements of the lowest temperature differentials, which occurred at the highest bulk temperatures. For this reason, all the condensation rates reported here were measured using the mass method.

The major source of error in the mass method is water carried into the test section either by "wet" steam, or as a result of condensation upstream of the main condensation interface. (The thermal method is not prone to such an error, at least if the water inflow is not too large, because it is based on a heat rather than a mass balance and the sensible heat of any incoming water is typically very small compared with the latent heat of condensation.) These errors were eliminated by lining the walls of the steam settling tank, the steam inflow lines, and the test section walls above the water level with strip heaters and insulation, and running all tests with these surfaces superheated, so that no condensation would occur and all droplets would be vaporized before passing into the test section. Tests showed that with no wall heating (zero steam superheat), the mass method tended to overestimate the true condensation rate somewhat, but that the true value would be obtained provided the superheat was maintained at a level higher than a few °C. An example is show in Figure 1.8. Note that a modest steam superheat (a few tens of degrees, say) does not affect the condensation rate at the liquid surface because the added enthalpy which is associated with the superheat is small compared with the

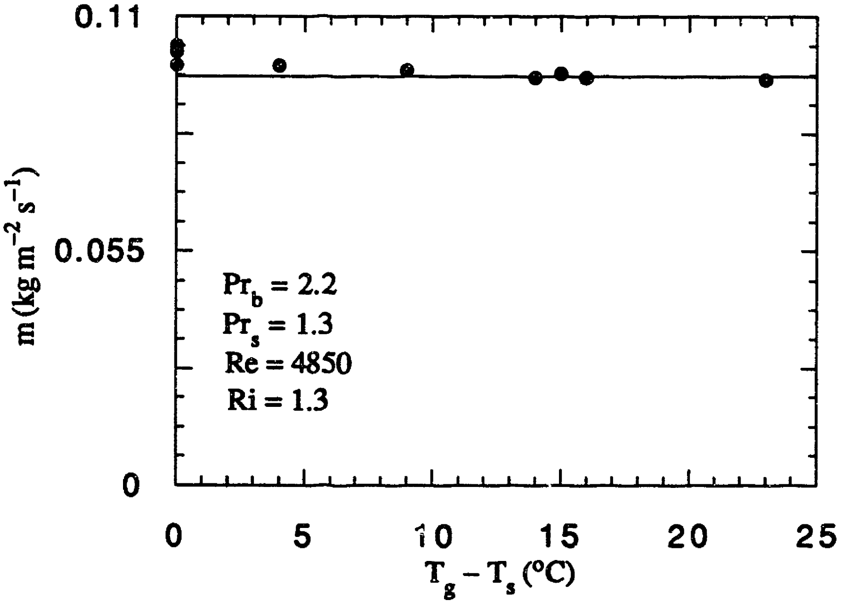

Figure 1.8. The effect of steam superheat on the condensation rate measurement. A modest steam superheat eliminates condensation from occurring upstream of the interface.

latent heat of condensation. As a final test for the absence of condensation upstream of the bulk water surface, the pump was turned off and a steady state was attained with no turbulence on the liquid side, but with the steam exhausting slowly from the vent in the test cell (see below). No measurable condensation was detected.

Air or other noncondensables in the steam are also potential sources of error in all condensation measurements. These were eliminated in two ways. First, data were taken only after the system, including the settling tank, had been thoroughly flushed with at least 50 system volumes of steam, and the readings were invariant with time. Secondly, to prevent the gradual buildup of noncondensables which might result from even very small mass fractions of air in the steam, a small amount of steam was continuously exhausted from the test cell via a central tube fairly close to the water surface. The exhaust rate was set empirically in a range where its magnitude had no effect on the condensation rate (the concern here being that excess steam flow rate might increase the liquid-side turbulence by shear at the surface, while too low a steam flow rate might allow noncondensables to accumulate). The second measure proved to be unnecessary, since tests with the steam exhaust closed for up to an hour showed no decrease in the condensation rate. Nevertheless, all data reported here were taken while a small amount of steam was exhausted from the cell.

Data reproducibility was checked by recording the condensation rate at a standard condition at the beginning and end of each day of runs. The data is shown in Figure 1.9 and the r.m.s. value of the scatter in this data set is 3% of the mean.

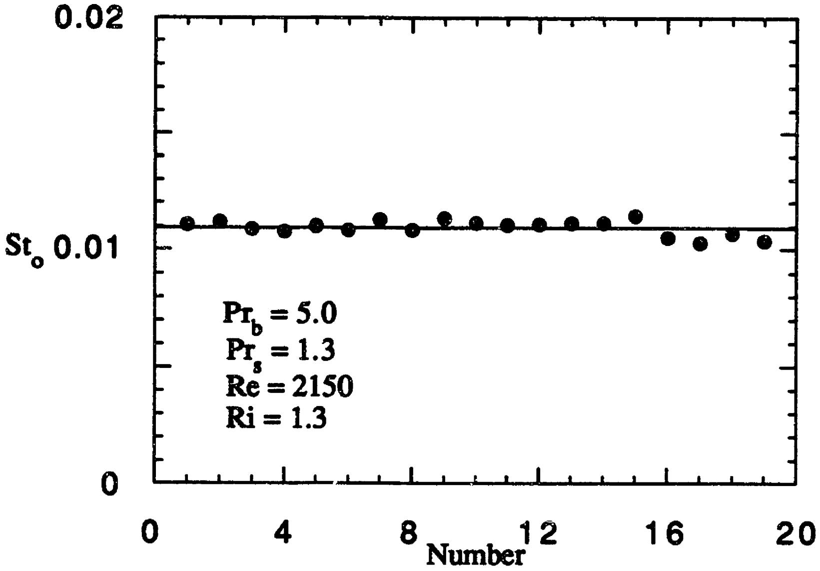

Figure 1.9. Data reproducibilty checked by repeating a standard test at the beginning and end of each day for ten days.

1.5. Scaling Relations

Consider a pure vapor, with temperature T_g and saturation temperature T_s, in contact with its subcooled autogenous liquid. The vapor is quiescent but drifts toward the liquid surface, where it condenses and releases it latent heat h_{fg} to the liquid. The liquid is in turbulent agitation. Attention is restricted to cases where the turbulence near the interface is the result of some mixing process or shear flow in the bulk of the liquid, deep below the surface, and not due to surface shear exerted by a horizontal vapor flow. Solid boundaries are remote from the interface (i.e. many turbulent macroscales away) and do not affect the local condensation rate directly, although they may play a role in the energy balance that controls the "bulk" liquid subcooling. Both the liquid-side turbulence and the condensation heat transfer process are assumed to have reached statistically steady states.

Below the free surface there will be an interfacial layer, about one turbulence macroscale thick, in which the turbulence and temperature distributions are strongly affected by the interfacial boundary conditions. As the interface is approached from below, the vertical velocity fluctuations will tend to be damped and the horizontal velocity fluctuations amplified, and the mean temperature will rise rapidly from the bulk to the saturation value. The premise is that the local condensation rate can be completely specified in terms of the fluid properties and the turbulence conditions "imposed" on the interface just below the interfacial layer. This is a high Reynolds number (and not too low Prandtl number) modeling approximation made in the spirit of dealing with interfacial layers in terms of inner and outer expansions. It leaves the question, however, of what constitutes a suitable definition of the "imposed" turbulence. The turbulence in the bulk region, being generated from below, will necessarily decay in intensity with elevation even below the interfacial layer, but at a rate which is lower than in the interfacial region, as sketched in Figure 1.10.a (see also Section 1.3 and Komori et al., 1982).

The following assumptions are made:

(1) The turbulence "at the surface" may be characterized by (i) the extrapolated value v_b of the turbulence intensity $v(y)$ from the bulk liquid region to the interface, ignoring the interfacial layer (Figure 1.10.a), (ii) a similarly extrapolated turbulence macroscale

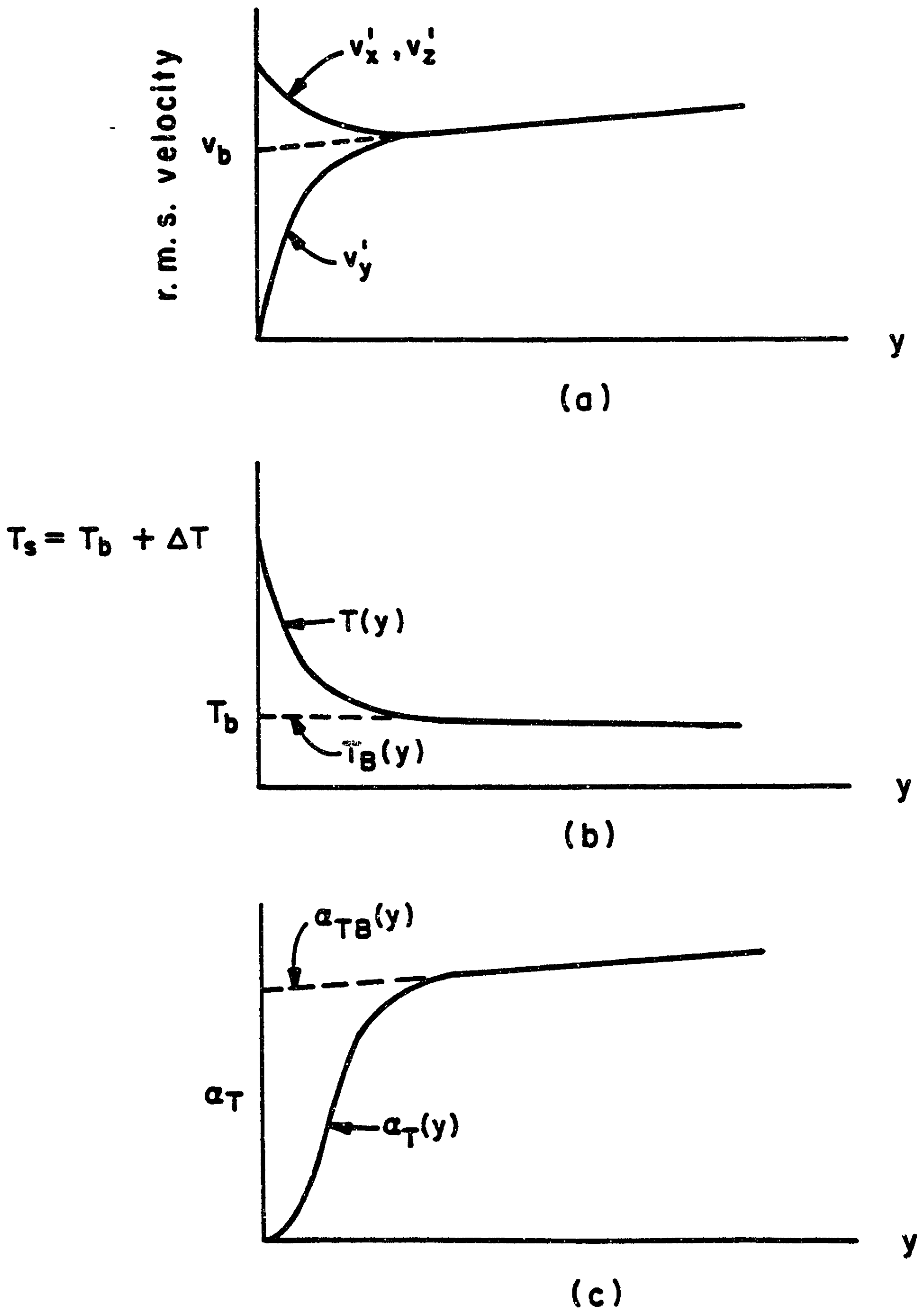

Figure 1.10. Distributions of (a) r.m.s. velocity, (b) mean temperature and (c) turbulent diffusivity. Definition of bulk values.

Λ_b, (iii) the liquid viscosity and (iv) the liquid density. The first two define the large scales of the imposed turbulence; the last two, which are more specifically defined below, affect the energy cascade process and the small dissipative scales.

In these experiments, the turbulence below the interfacial layer is approximately isotropic, and the quantity v_b is defined as the extrapolated r.m.s. value of any *single component* of the fluctuating velocity from the bulk to the surface.

(2) The liquid subcooling is defined as

$$\Delta T \equiv T_s - T_b \tag{1.13}$$

where T_s is the vapor saturation temperature and T_b is the temperature obtained by extrapolating the mean temperature in the bulk of the liquid to the surface, ignoring the interfacial layer (Figure 1.10.b). The temperature gradient in the bulk liquid region is usually small compared with the gradient near the interface, and T_b can be interpreted as simply the local bulk temperature.

(3) The liquid properties which affect the condensation rate are the density, the specific heat at constant pressure, the thermal conductivity and the viscosity. The density, the specific heat at constant pressure and the thermal conductivity of most liquids are relatively temperature insensitive, and these quantities are modeled as being uniform at their "bulk" values ρ_b, c_{pb} and λ_b. (In water, for example, these properties change by –7, +2 and +11%, respectively, as the bulk temperature increases from 37 to 135°C, the maximum bulk to saturation temperature range in the present experiments.)

Liquid viscosity is highly temperature dependent, however, and may vary significantly in the interfacial layer. In water the viscosity decreases by a factor of three as the temperature increases from 37 to 135°C. This temperature dependence should strictly speaking be accounted for in the scaling laws, since reduced viscosity in the hot interfacial layer may in principle affect the turbulence structure in that critical region, and hence influence the condensation rate. This is done by noting that the free volume theory of Hildebrand (1971, 1977) suggests that the viscosity of a liquid can be fitted over some range of temperatures and pressures with an equation of the form

$$\frac{1}{\mu} = A + BT \tag{1.14}$$

where A and B are constants. For all liquids in which equation (1.14) applies between the bulk temperature T_b and the saturation temperature T_s, the viscosity can be expressed between those temperature limits as

$$\frac{1}{\mu} = \frac{1}{\mu_b} + \left(\frac{1}{\mu_s} - \frac{1}{\mu_b}\right)\frac{T - T_b}{\Delta T} \tag{1.15}$$

where μ_b and μ_s are the liquid viscosities at bulk and saturation conditions, respectively. Figure 1.11 shows that equation (1.15) is a very good approximation for water over the temperature range from 37 to 135 °C. Equation (1.15) is also usually a good approximation for typical cryogenic liquids. (For example, Figure 1.12 shows equation (1.15) plotted for liquid hydrogen over the temperature range from 20 to 24 K, which

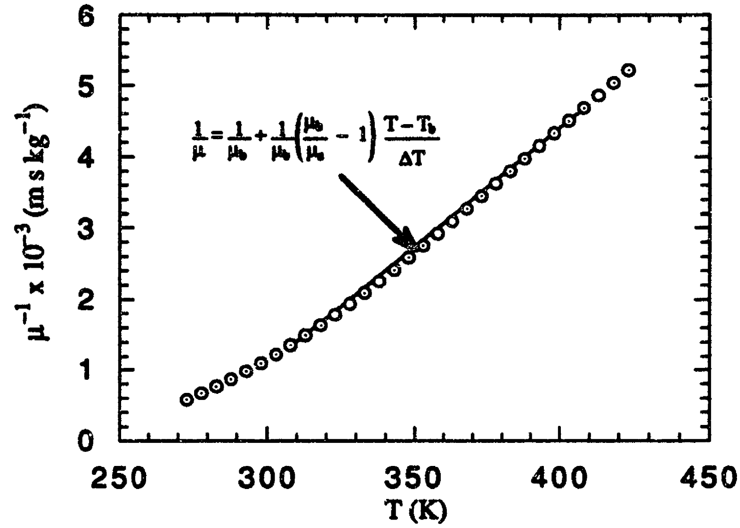

Figure 1.11. Viscosity as a function of temperature for water.

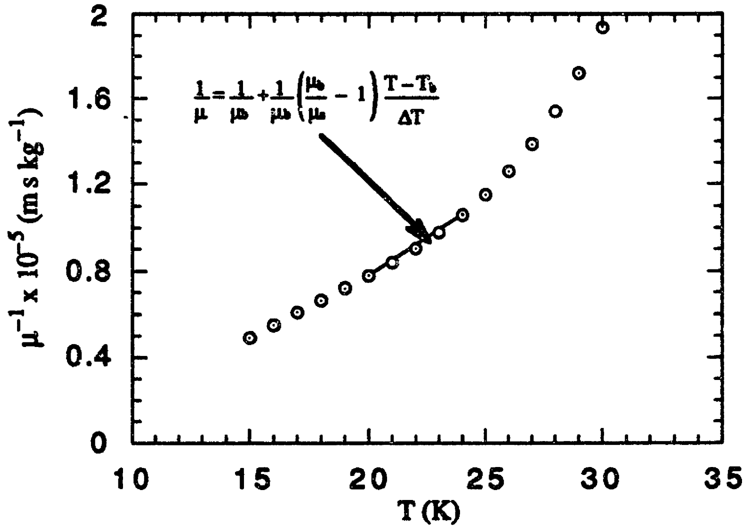

Figure 1.12. Viscosity as a function of temperature for liquid hydrogen.

is a typical temperature range of interest to NASA.)

Equation (1.15) implies that the viscosity is completely specified by the temperature difference $T - T_b$ and the quantities μ_b, μ_s and ΔT.

(4) Buoyancy effects will be accounted for in the Boussinesq approximation, where the buoyancy force in the equation of motion is expressed as

$$g\beta_b(T - T_b) \tag{1.16}$$

where g is either the acceleration of gravity or an acceleration applied normal to the interface and β_b is the liquid's bulk coefficient of thermal expansion. β is characterized by its bulk value (an approximation), even though β depends significantly on temperature in many liquids and may have a different value in the hotter region near the interface. The bulk value is chosen because we are mainly interested in being able to properly scale the onset of buoyancy effects, and less concerned with accurately scaling conditions where a hot stagnant layer has developed on the surface.

(5) Surface waviness, always present to some degree on a turbulent surface, is assumed not to affect the condensation mass flux. This is true if the amplitude of the turbulence-induced waviness is small compared with the turbulence macroscale (wavelength), that is,

$$\frac{v_b^2}{g\Lambda_b} \ll 1 \tag{1.17}$$

Under these conditions, the surface is approximately horizontal, at least in the sense that its radius of curvature is large compared with the thermal layer thickness at the interface, and the condensation process will not depend on g except via the product $\beta_b g$ which characterizes the buoyancy effects.

(6) The condensation is assumed to be controlled by the rate at which the latent heat h_{fg} is transferred from the interface to the bulk of the liquid, and unaffected by any other vapor phase property. This is true if (i) the vapor's superheat enthalpy and kinetic energy do not add significantly to the energy flux from the interface into the liquid, that is,

$$\frac{c_{pg}(T_g - T_s)}{h_{fg}} \ll 1 \tag{1.18}$$

and

$$\frac{\dot{m}^2}{\rho_g^2 h_{fg}} \ll 1 \tag{1.19}$$

and (ii) the momentum flux associated with the vapor's impact on the surface does not alter the liquid-side turbulence, that is,

$$\frac{\dot{m}^2}{\rho_g \rho_b v_b^2} \ll 1 \qquad (1.20)$$

Here $\dot{m}$ is the condensation mass flux and the subscript g refers to vapor phase properties.

These criteria are satisfied in typical condensation problems unless the vapor is very highly superheated. Chun et al. (1986) have shown that violations may also occur at very high turbulence intensity and/or subcooling, where the condensation can become unstable, and transient, very high-intensity condensation bursts can occur. Such condensation bursts are not covered by the scaling laws discussed here.

Based on the model presented above, the condensation mass flux is given by

$$\dot{m} = \dot{m}(v_b, \Lambda_b, \mu_b, \mu_s, \rho_b, \lambda_b, c_{pb}, \Delta T, h_{fg}, \beta_b g) \qquad (1.21)$$

It follows immediately from dimensional analysis that

$$St = f(Re, Ri, Pr_b, Pr_s, Ja) \qquad (1.22)$$

where

$$\begin{aligned}
\mathrm{St} &\equiv \frac{\dot{m}h_{fg}}{\rho_b c_{pb} \Delta T v_b} = \text{condensation Stanton number} \\
\mathrm{Re} &\equiv \frac{\rho_b v_b \Lambda_b}{\mu_b} = \text{turbulent eddy Reynolds number} \\
\mathrm{Ri} &\equiv \frac{g\beta_b \Delta T \Lambda_b}{v_b^2} = \text{Richardson number} \\
\mathrm{Pr}_b &\equiv \frac{\mu_b c_{pb}}{\lambda_b} = \text{bulk Prandtl number} \\
\mathrm{Pr}_s &\equiv \frac{\mu_s c_{pb}}{\lambda_b} = \text{saturation Prandtl number} \\
\mathrm{Ja} &\equiv \frac{c_{pb} \Delta T}{h_{fg}} = \text{Jakob number}
\end{aligned} \tag{1.23}$$

Strictly speaking there should be in equation (1.23) another parameter which can be taken as $v_b^2/c_{pb}\Delta T$. It can be shown that this parameter is essentially a ratio of the heat input which results from turbulent viscous dissipation to the heat input which results from the latent heat. Heating due to turbulent viscous dissipation is negligible in most condensation problems, and hence this parameter should not affect the Stanton number.

The Stanton number is a ratio of the heat transferred at the interface to that which can be transported by the liquid. The eddy Reynolds number is a ratio of the inertia forces to viscous forces and will be large in all cases where the liquid side is fully turbulent. The Richardson number scales buoyancy effects. In a gravitational field buoyancy effects tend to dampen the turbulence near a condensation interface, and to reduce the condensation rate. Based on analogous mixing processes [Hopfinger and

Toly (1976); Hopfinger and Hopfinger (1986)], one expects that the effect will be negligible if the Richardson number is smaller than some critical value of order unity, and significant at higher Richardson numbers. The bulk Prandtl number scales the thermal and viscous diffusivities. The saturation Prandtl number Pr_s must be included if the viscosity difference between saturation and bulk conditions has a significant effect on the smaller scale turbulence structure near the interface. The effect of the Jakob number is discussed in Section 1.6 below.

1.6. An Analysis

One impediment to a purely empirical determination of the functional form of equation (1.22) is the fact that both the Richardson and the Jakob numbers depend on ΔT. These dependencies will be attempted to be separated by means of the following analysis for the Jakob number dependence, which is an elaboration of the one used by Sonin et al. (1986).

The Jakob number scales the feedback effect of the condensation-induced bulk flow on the condensation rate. This can be seen by noting that the thermal layer thickness δ, i.e. the effective thickness of the region in which the temperature drops from T_s to T_b, is by definition

$$\dot{m} h_{fg} \equiv \frac{\lambda_b \Delta T}{\delta} \qquad (1.24)$$

Using equations (1.23) and (1.24), we can write the Jakob number as

$$Ja = \frac{u_c \delta}{\alpha_b} \tag{1.25}$$

where

$$u_c = \dot{m}/\rho_b \tag{1.26}$$

is the bulk flow speed induced on the liquid side by the condensation. The Jakob number is thus essentially the Peclet number based on the condensation-induced flow speed and the thermal layer thickness. This suggests that the condensation rate should decrease as the Jakob number increases, the flow velocity being in the direction of the heat flux.

A more quantitative idea of the Jakob number effect can be obtained by the following relatively simple theory. In the absence of mean liquid flow parallel to the surface (as in our experiments), the Reynolds-averaged temperature T(y) in the liquid is given by

$$u_c \frac{\partial T}{\partial y} = \frac{\partial}{\partial y}\left[\left(\alpha + \alpha_T\right)\frac{\partial T}{\partial y}\right] \tag{1.27}$$

where y is the distance measured from the interface toward the bulk of the liquid, u_c the condensation-induced flow speed given by equation (1.26), and

$$\alpha_T \equiv -\frac{\langle v'T' \rangle}{(\partial T/\partial y)} \tag{1.28}$$

is the turbulent thermal diffusivity, $\langle v'T' \rangle$ being the Reynolds-averaged turbulent heat flux divided by $\rho_b c_{pb}$.

Equation (1.27) is subject to the boundary conditions

$$\begin{gathered} T(0) = T_s \\ \rho_b u_c h_{fg} = -\rho_b c_{pb} \alpha_b \left(\frac{\partial T}{\partial y}\right)_{y=0} \end{gathered} \tag{1.29}$$

An integration of equation (1.27) yields

$$\ln\left[1 + \frac{c_{pb}(T_s - T)}{h_{fg}}\right] = u_c \int_0^y \frac{dy}{\alpha + \alpha_T} \tag{1.30}$$

The distribution of the "bulk" liquid temperature $T_B(y)$ satisfies equation (1.27) with α_T equal to the thermal diffusivity α_{TB} in the bulk (see Figure 1.10.c). Integrating this equation from $y = 0$, where $T_B \equiv T_b$ (Figure 1.10.b), gives

$$\ln\left[\frac{1+\dfrac{c_{pb}(T_s-T_B)}{h_{fg}}}{1+Ja}\right]=u_c\int_0^y\frac{dy}{\alpha+\alpha_{TB}} \tag{1.31}$$

The difference between equations (1.30) and (1.31) yields

$$\ln\left[\frac{\left(1+\dfrac{c_{pb}(T_s-T)}{h_{fg}}\right)}{\left(1+\dfrac{c_{pb}(T_s-T_B)}{h_{fg}}\right)}(1+Ja)\right]=u_c\int_0^y\frac{(\alpha_{TB}-\alpha_T)}{(\alpha+\alpha_T)(\alpha+\alpha_{TB})}dy \tag{1.32}$$

Now, for y larger than the interfacial layer thickness, $T(y)\rightarrow T_B(y)$ and $\alpha_T(y)\rightarrow\alpha_{TB}(y)$, and equation (1.32) reduces to an equation for u_c, which can be converted to an equation for St via equations (1.23) and (1.26). The result is

$$St=St_o\frac{\ln(1+Ja)}{Ja} \tag{1.33}$$

where

$$St_o^{-1}\equiv v_b\int_0^\infty\frac{(\alpha_{TB}-\alpha_T)}{(\alpha+\alpha_T)(\alpha+\alpha_{TB})}dy \tag{1.34}$$

If it were now possible to argue that the condensation-induced flow speed u_c does not affect the turbulent diffusivity $\alpha_T(y)$ significantly, at least at small Jakob numbers, one could conclude that the function St_o should be independent of Jakob number, i.e.

$$St_o = f(Re, Ri, Pr_b, Pr_s) \tag{1.35}$$

Equations (1.33) and (1.35) would then give the Jakob number dependence of St. For Ja « 1, one has

$$St \cong St_o\left(1 - \frac{Ja}{2}\right) \tag{1.36}$$

which shows that St_o represents the Stanton number in the limit $Ja \rightarrow 0$, and that the Jakob number effect is small as long as Ja « 1.

Equations (1.35) and (1.36) are based on the assumption that the turbulent diffusivity is not significantly affected by the condensation drift speed u_c if Ja « 1. More specifically, the assumption is that the first-order correction term due to the dependence of St_o on Ja be small compared with Ja/2. Whether this is in fact so cannot be proved conclusively until there is a better understanding of the turbulence near the free surface. In the present study, the Jakob number was small (of order of 0.1) and its effect on the condensation was also small. However, it turns out that the present data correlates somewhat better with the assumption that St_o is independent of Jakob number than with the assumption that the Jakob number effect on St is negligible. Equations (1.35) and (1.36) are therefore adopted as a working hypothesis.

Some further insight into the condensation process may be obtained by noting that when equation (1.28) is expanded in Taylor series about $y = 0$, and the boundary conditions at the free surface applied (zero shear, zero vertical velocity, uniform temperature at the surface), one finds that the first non-zero term is of the order of y^2

$$\alpha_T = \frac{y^2}{\tau} + O(y^3) \tag{1.37}$$

where τ is a statistical property, with dimension time, of the turbulent velocity and temperature fluctuations at the interface

$$\tau^{-1} \equiv \left\langle \frac{\partial T'}{\partial y}\frac{\partial v'}{\partial y} \right\rangle_{y=0} \left(-\frac{\partial T}{\partial y} \right)^{-1} \tag{1.38}$$

If we take as a working approximation for $\alpha_T(y)$ for all y the equation

$$\frac{1}{\alpha_T(y)} = \frac{\tau}{y^2} + \frac{1}{\alpha_{TB}(y)} \tag{1.39}$$

which gives the correct results for both the limits of small and large y, and if it is assumed that $\alpha_{TB} \gg \alpha$ everywhere, equation (1.34) simplifies to

$$St_o^{-1} \equiv v_b \int_0^{\infty} \frac{dy}{\alpha + \frac{y^2}{\tau}} \tag{1.40}$$

or

$$St_o = \frac{2}{\pi v_b}\left(\frac{\alpha}{\tau}\right)^{1/2} \tag{1.41}$$

This does not solve the problem, but simply reduces it to that of determining the time scale τ as a function of turbulence characteristics and fluid properties. Results similar to equation (1.41) have been derived by King (1966), Ledwell (1984), and others. The current derivation emphasizes the point that, provided the molecular diffusivity α is everywhere small compared with the turbulent diffusivity α_{TB} associated with the bulk liquid, the quantity St_o is unaffected by $\alpha_{TB}(y)$, regardless of the thickness of the interfacial thermal layer. Equations (1.37) and (1.41) link the condensation rate to the turbulent diffusivity distribution near the interface.

1.7. Condensation Rate Correlation

The experimental variables over which control was exercised were four: bulk temperature T_b (via the heat exchanger), saturation temperature T_s (via system pressure), liquid-side turbulence intensity v_b (via nozzle momentum flux) and turbulence macroscale Λ_b (via system size). v_b is taken as the *average* value over the free surface [see equations (1.4) and (1.7)]

$$v_b \equiv (v_b)_{av} = 21.1 \frac{Q}{Dd} \exp(-1.2s/D) \qquad (1.42)$$

The macroscale is given in terms of system diameter by equation (1.11).

Table 1.2 summarizes the bulk and saturation temperatures chosen for the test matrix and lists the corresponding liquid Prandtl and Jakob numbers.

Figure 1.13 shows typical data of condensation mass flux vs. liquid-side turbulence intensity v_b, taken in the larger system (D = 10.2 cm) at constant bulk and saturation conditions. The upper bound of v_b is controlled by the requirement that the amplitude of the surface waves remain small (below about 1/2 cm in the larger system, as determined by visual inspection), so that the interfacial area can be approximated as $\pi D^2/4$. Note that the two data sets have different saturation conditions and therefore different subcooling.

In what follows all data is presented in terms of the modified Stanton number

$$St_o = St\left(1 + \frac{Ja}{2}\right) \qquad (1.43)$$

which is assumed to be independent of Jakob number. Some support for this independence may be deduced from the data correlation (see the discussion at the end of this section).

Table 1.2. Test matrix for condensation tests (see Figures 1.14 – 1.16).

(a) Symbols for test conditions

	T_s (°C)	
T_b (°C)	135	103
4.65	●	○
3.15	■	□
2.55	▲	△
2.2	◆	◇
1.5	⊞	

With line through data points: D = 3.8 cm.
Without line through data points: D = 10.2 cm.

(b) Prandtl number

	Pr_s	
Pr_b	1.3	1.7
4.65	●	○
3.15	■	□
2.55	▲	△
2.2	◆	◇
1.5	⊞	

With line through data points: D = 3.8 cm.
Without line through data points: D = 10.2 cm.

(c) Jakob number

	Pr_s	
Pr_b	1.3	1.7
4.65	0.19	0.12
3.15	0.15	0.09
2.55	0.13	0.06
2.2	0.11	0.04
1.5	0.03 – 0.06	

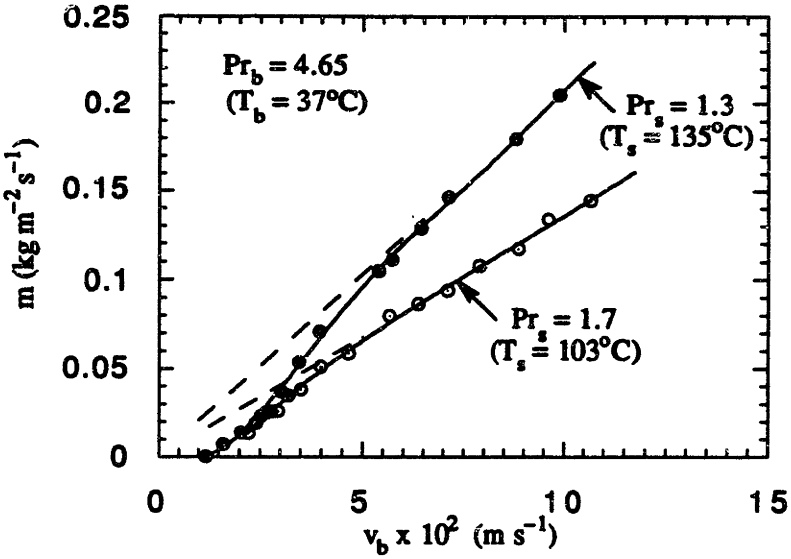

Figure 1.13. Condensation mass flow rate vs turbulence intensity for steam and water at $Pr_b = 4.65$ ($T_b = 37°C$).

The Reynolds and Richardson number dependencies are at first sight difficult to separate because both these numbers vary with the experimental variables. It appears, however, that the condensation Stanton number is insensitive to Reynolds number. Figures 1.14 and 1.15 show all the present data for St_o, plotted first against Reynolds number and then against Richardson number. Re and Ri are related by

$$Ri = Gr\, Re^{-2} \tag{1.44}$$

where the Grashof number

$$Gr \equiv \frac{g\beta_b \Delta T \Lambda_b^3}{\nu_b^2} \tag{1.45}$$

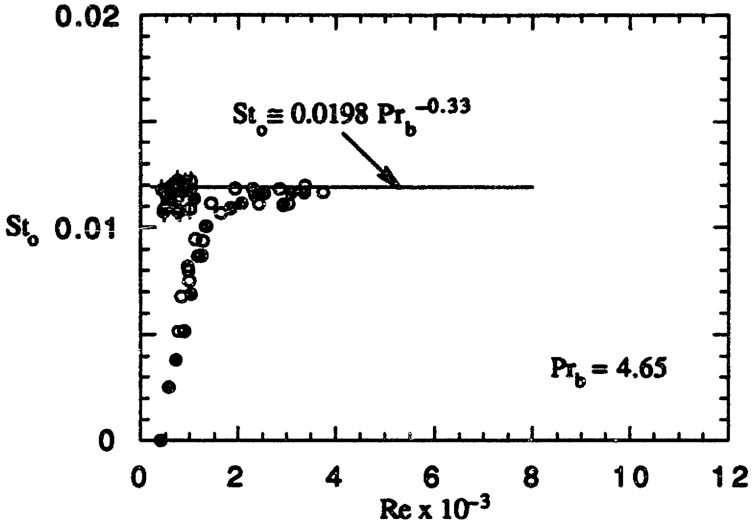

Figure 1.14.a. Reduced Stanton number vs Reynolds number for $Pr_b = 4.65$. See Table 1.2 for symbols.

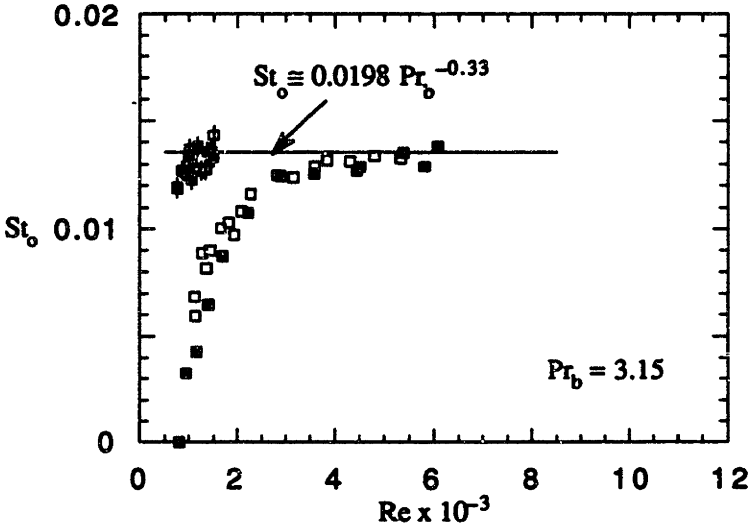

Figure 1.14.b. Reduced Stanton number vs Reynolds number for $Pr_b = 3.15$. See Table 1.2 for symbols.

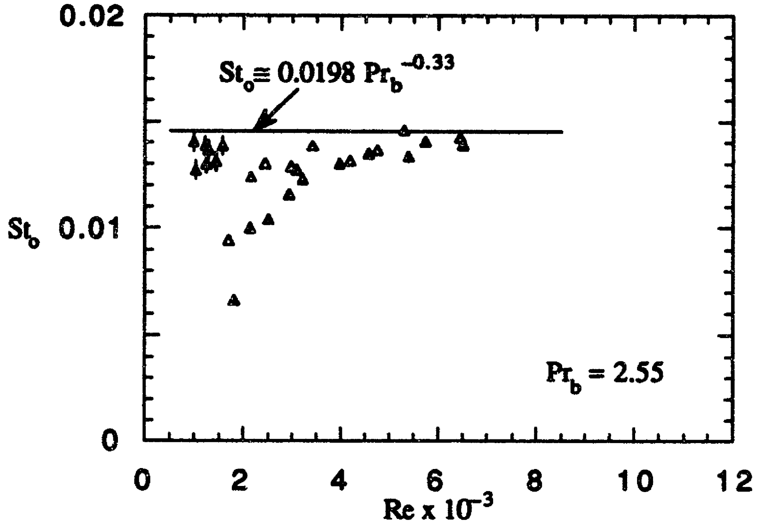

Figure 1.14.c. Reduced Stanton number vs Reynolds number for $Pr_b = 2.55$. See Table 1.2 for symbols.

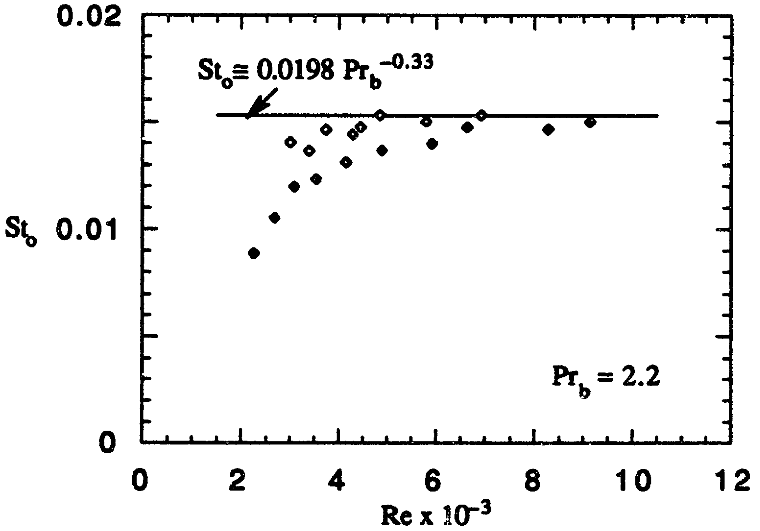

Figure 1.14.d. Reduced Stanton number vs Reynolds number for $Pr_b = 2.2$. See Table 1.2 for symbols.

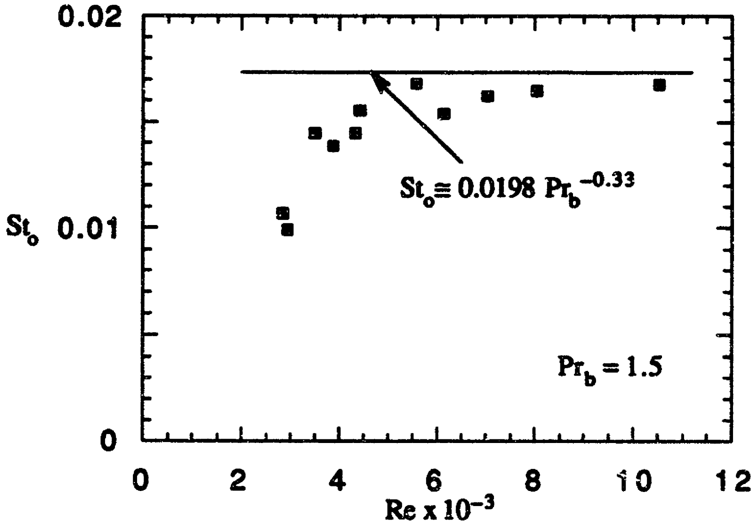

Figure 1.14.e. Reduced Stanton number vs Reynolds number for $Pr_b = 1.5$. See Table 1.2 for symbols.

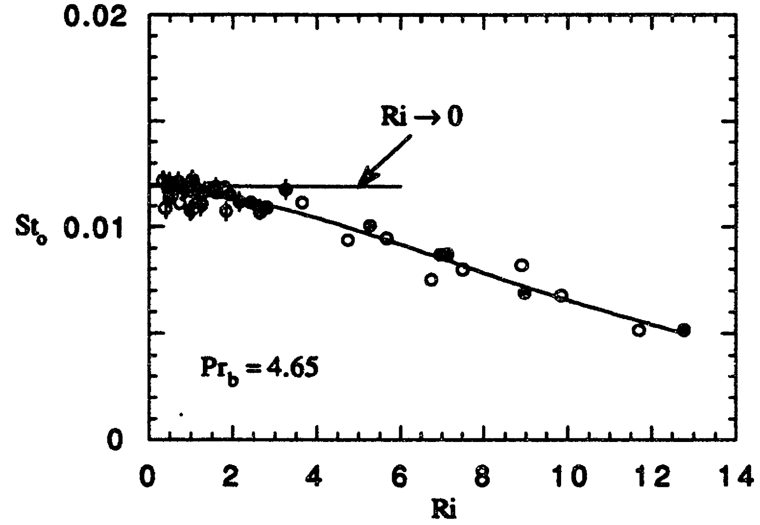

Figure 1.15.a. Reduced Stanton number vs Richardson number for $Pr_b = 4.65$. See Table 1.2 for symbols.

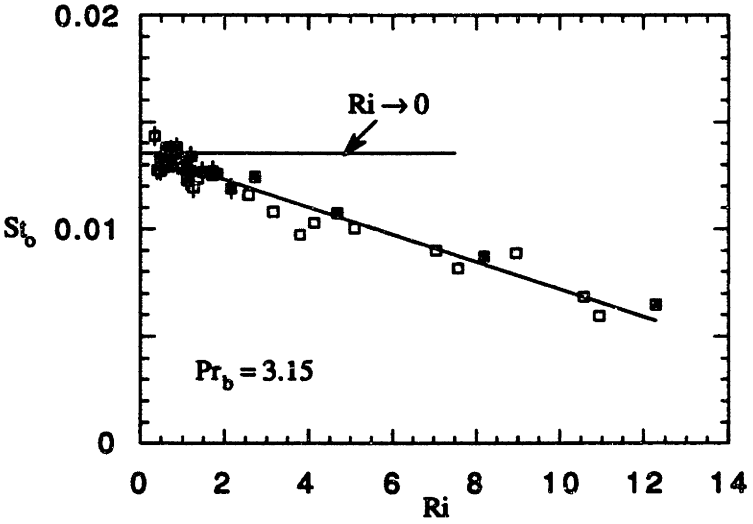

Figure 1.15.b. Reduced Stanton number vs Richardson number for $Pr_b = 3.15$. See Table 1.2 for symbols.

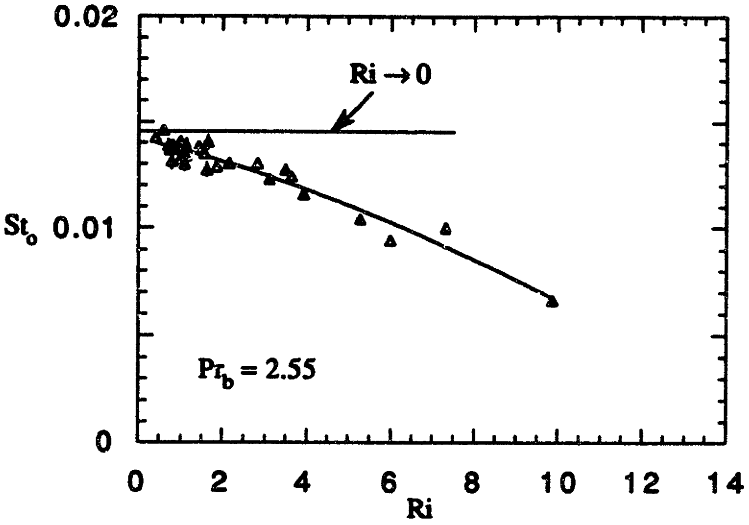

Figure 1.15.c. Reduced Stanton number vs Richardson number for $Pr_b = 2.55$. See Table 1.2 for symbols.

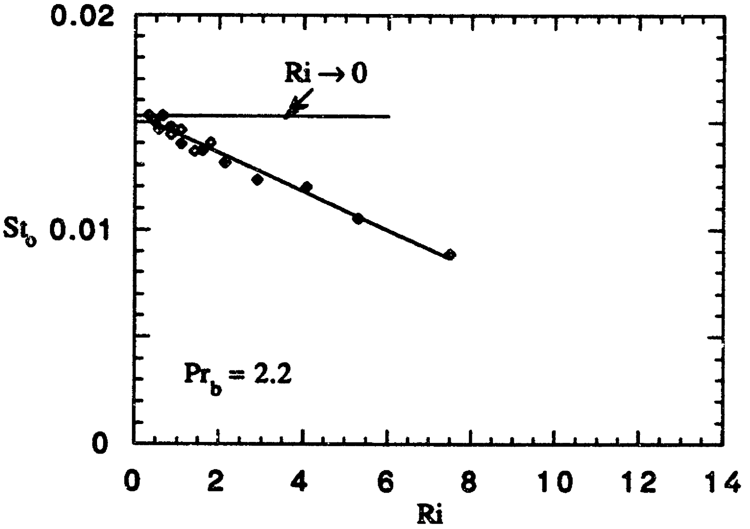

Figure 1.15.d. Reduced Stanton number vs Richardson number for $Pr_b = 2.2$. See Table 1.2 for symbols.

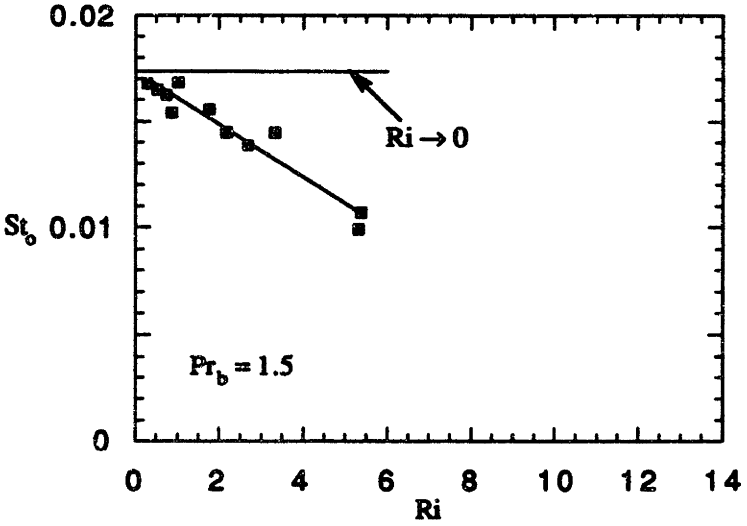

Figure 1.15.e. Reduced Stanton number vs Richardson number for $Pr_b = 1.5$. See Table 1.2 for symbols.

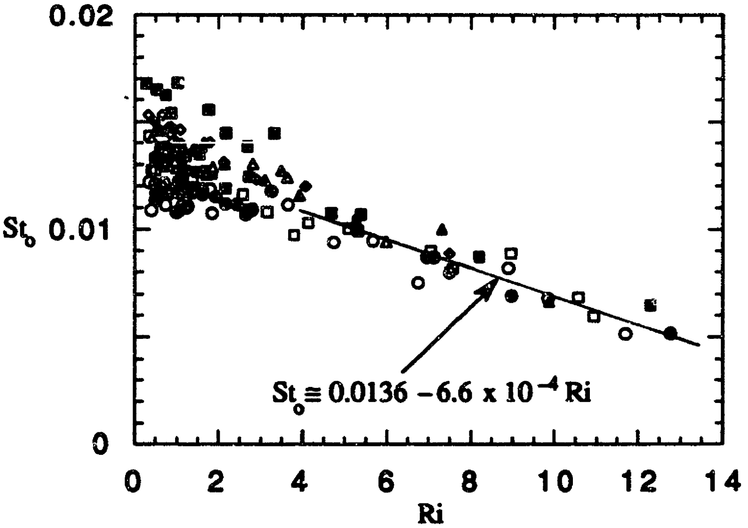

Figure 1.16. Reduced Stanton number vs Richardson number. See Table 1.2 for symbols.

depends mainly on the system diameter via A_b.

All the data plots show the same trend. For given system size, the Stanton number reaches a constant (maximum) value at sufficiently high Re or sufficiently low Ri, but declines sharply when Re is reduced below a critical value, or when Ri becomes significant compared with unity. The decline may in principle be due to high Richardson number (i.e. damping of the turbulence by thermal stratification near the surface), low Reynolds number (i.e. damping of the turbulence by viscous effects), or both. A comparison of the data taken in the large and small systems suggests that viscous damping can be ruled out: both systems exhibit the same maximum values, and no decline from the maximum value occurs in the small system at Reynolds numbers where a decline was observed in the large system. On the Richardson number plots, the data from both systems collapse onto the same curve. The figures clearly imply that, at least in the range of Reynolds numbers investigated, the Stanton number depends on Richardson number and bulk Prandtl number but not on Reynolds number. In addition, the plots against Ri show no difference between the two values of saturation Prandtl number. The present data thus suggest that

$$\begin{gathered} St_o \equiv St_o(Ri, Pr_b) \\ 350 < Re < 11000 \\ 1.3 < Pr_s < 1.7 \\ 1.5 < Pr_b < 5 \\ 0.03 < Ja < 0.2 \end{gathered} \tag{1.46}$$

The functional form of equation (1.46) is defined in Figure 1.15, and summarized in Figure 1.16.

The effect of thermal stratification was visible to the naked eye, particularly at low bulk temperatures and with back lighting which tended to give rise to a shadowgraph effect. At turbulence intensities where Ri was of the order 1 – 3, say, one could observe a hot layer at the surface, a few millimeters thick, which was formed and then periodically swept away by an energetic eddy. At still lower v_b ($Ri \sim 10$), the turbulence was not intense enough to overcome the damping effects of the thermal stratification, and the hot layer would no longer be swept away. At the lowest turbulence intensities ($Ri \sim 50$), stagnant hot layers of the order 3 cm thick were observed beneath the interface.

The limit $Ri \rightarrow 0$ where the effect of thermal stratification is negligible may be obtained by extrapolating the data to $Ri = 0$. The result is shown in Figure 1.17, and can be expressed by the equation

$$St_o = 0.0198 Pr_b^{-0.33} \qquad (Ri \rightarrow 0) \qquad (1.47)$$

The bars in Figure 1.17 represent an assessment of the uncertainty in determining the limit $Ri \rightarrow 0$ from the data in Figure 1.15.

At $Ri > 3.5$, on the other hand, the data for all Pr_b tend to fall approximately on a common curve (Figure 1.16), which can be represented as

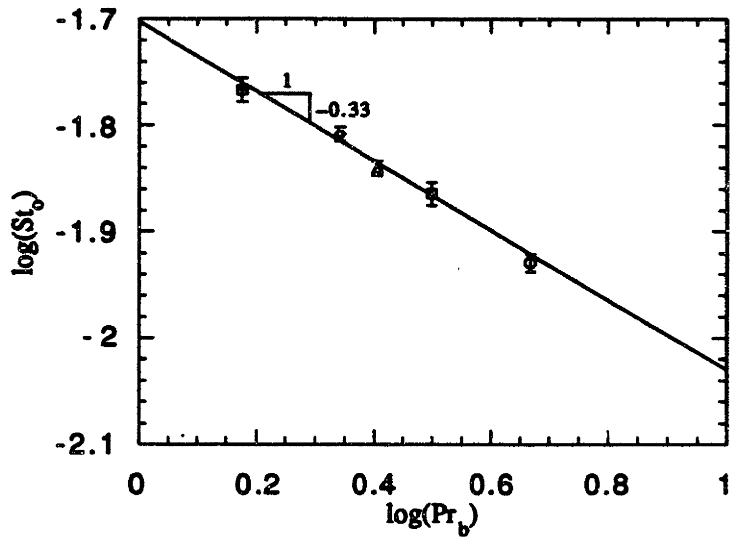

Figure 1.17. Reduced Stanton number, extrapolated to Ri → 0, vs bulk Prandtl number.

$$\mathrm{St}_o \cong 0.0136 - 6.6 \times 10^{-4}\,\mathrm{Ri} \qquad (3.5 < \mathrm{Ri} < 15) \tag{1.48}$$

Finally, some comments about the assumption that the modified Stanton number defined in equation (1.43) is independent of Jakob number, which would suggest that the Stanton number should depend on Ja according to

$$\mathrm{St} \cong \mathrm{St}_o\left(1 - \frac{\mathrm{Ja}}{2}\right) \qquad (\mathrm{Ja} \ll 1) \tag{1.49}$$

Figure 1.18 shows three data sets of St vs. Ja. Each set is taken at constant Pr_b and essentially constant Re. The Jakob number was varied by changing the saturation

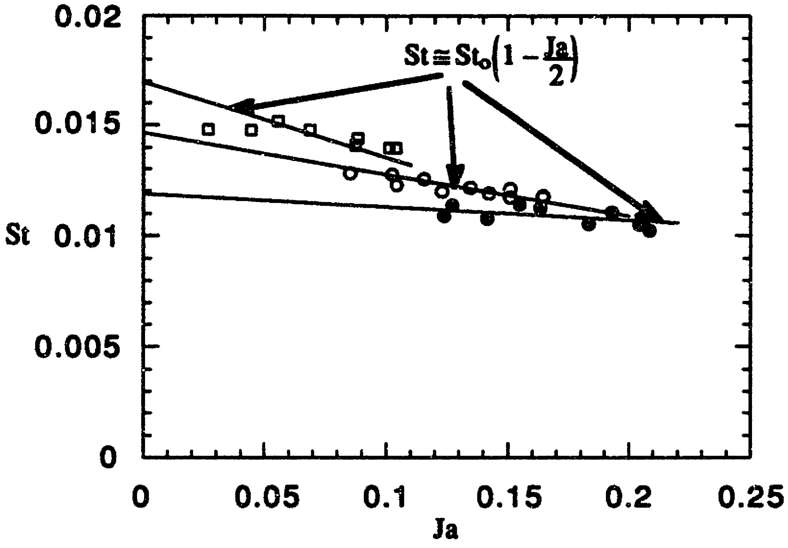

Figure 1.18. Condensation Stanton number as a function of Jakob number. Data obtained by varying saturation temperature. See Table 1.3 for test conditions.

Table 1.3. Test conditions for Figure 1.18.

Symbol	T_b (°C)	Re	Ri
□	88	4370 ± 135	0.6 – 2.3
○	57	3020 ± 70	1.5 – 2.8
●	37	2300 ± 80	1.2 – 2.1

temperature from 140 to 102°C (Pr_s from 1.25 to 1.7). Within each set the Richardson number varies with the Jakob number, but remains relatively small throughout the data range (see Table 1.3), so that its effect on St_o is not large. Also shown on the figure are "theoretical" curves based on equation (1.49) with St_o taken from Figure 1.15. The agreement between experiment and "theory" is satisfactory. However, the dependence on Ja is so slight in our data that it is almost masked by the data scatter. We can say only that equation (1.49) appears to fit the data somewhat better than an assumption that St is independent of Ja.

1.8. Concluding Remarks

The present data suggest a condensation rate correlation of the form

$$St = St_c(Ri, Pr_b)\left(1 - \frac{Ja}{2}\right) \qquad (1.50)$$

where the modified Stanton number is given in Figure 1.15. The data correlation should be applicable for

$$\begin{gathered} 350 < Re < 11000 \\ Ri < 15 \\ 1 < Pr_b < 6 \\ 1 < Pr_s < 2 \\ Ja < 0.2 \end{gathered} \qquad (1.51)$$

These conditions apply not only to steam and water but also to most cryogenic fluids at normal pressures.

In the limit of $Ri \rightarrow 0$ of negligible buoyancy effects, St_0 is given by equation (1.47), and the condensation heat transfer process can be represented in terms of a Reynolds-averaged energy equation with a turbulent diffusivity given near the interface by

$$\frac{\alpha_T}{\nu} = 9.67 \times 10^{-4} \left(\frac{v_b y}{\nu}\right)^2 Pr_b^{0.34} \qquad (1.52)$$

Equation (1.52) follows from equations (1.37), (1.41) and (1.47). The Stanton number begins to fall below equation (1.47) when Ri reaches values of the order 1/2. This is consistent with studies of turbulence structure in stably stratified flows [Mizushina et al. (1978); Komori et al. (1983); Ogino (1986); Hopfinger and Toly (1976); Hopfinger and Hopfinger (1986)]. At $Ri > 3.5$, St_0 appears to become relatively insensitive to the bulk liquid Prandtl number and is given approximately by equation (1.48).

The Prandtl number dependence in equation (1.47) differs from the correlation proposed by Sonin et al. (1986), which had no dependence on Pr_b. Most of the data on which their correlation was based were taken at relatively low bulk temperatures, where Pr_b had values approximately 4 – 6. At $Pr_b = 5$, equation (1.47) gives $St_0 \cong 0.0116$, in good agreement with Sonin et al. if one compensates for the fact that their correlation was based on the centerline r.m.s. velocity while the present one is based on the average value, which is 10% lower. Their conclusion about the lack of Pr_b dependence, however, was based on a small additional subset of data (their Figure 11) which was taken at high bulk temperatures. The apparent insensitivity to bulk temperature was probably caused by the systematic thermistor error which was found present at high temperatures in the thermal method which Sonin et al. used for measuring the condensation flux (see Section 1.4).

The dependence on Prandtl number has not been previously measured for condensation at a turbulent free surface. The present data indicates that at Prandtl numbers in the range 1.5 – 5, the index in $St \sim Pr_b^{-n}$ is about 1/3. Note that the analogous exponent for the Schmidt number dependence in gas absorption at a liquid free surface is usually taken as $n \cong 1/2$ [see for example Ledwell (1984) and also Khoo (1988), who performed mass transfer experiments in the same type of test cell as used in the present work], although exponents as high as unity have been suggested [Davies et al. (1964)]. Gas absorption is, however, a high Schmidt number transport problem, with $Sc \sim 500$. At a solid boundary, the Stanton number based on the friction velocity u_* is proportional to $Pr_b^{-2/3}$ at high Prandtl numbers [Petukhov (1970)].

Insofar as a quantitative comparison is possible [Brown et al. (1989)], the present correlation is essentially in agreement with the steam condensation data of Thomas (1979), where the turbulence was generated from below the interface. The present correlation is strictly speaking not intended for flows like Jensen and Yuen's (1982), where the liquid-side turbulence is generated by shear at the free surface itself. Such turbulence is anisotropic and varies strongly near the surface, and cannot necessarily be adequately characterized by quantities v_b, Λ_b and μ_b. Nevertheless, if a direct comparison is attempted [Sonin et al. (1986)], one obtains agreement within a factor of two.

The Stanton number correlation presented here expresses the free surface condensation rate in terms of fluid properties and two local attributes of the liquid-side turbulence below the interfacial layer, the r.m.s. velocity v_b and a macroscale Λ_b. These two parameters must be available if the correlation is to be applied in a particular case. In principle, v_b and Λ_b can be obtained (only v_b is required if Ri is small) from empirical scaling relations, where available, or from a computation of the liquid-side flow field based on a turbulence model. If Λ_b is required, it becomes necessary to first establish how this quantity is related to whatever macroscale appears in the particular empirical correlation or turbulence model that is being used. Λ should be proportional to any other definition of a macroscale, say l. The coefficient of proportionality can be obtained from a single calibration. If l is obtained from an experimental correlation, one must have available one simultaneous measurement of both l and Λ, or predict the relationship theoretically. If l is derived from a turbulence model, it will often lack a physical definition. In that case a numerical calibration is necessary for the ratio of Λ and l. The calibration can be achieved by exercising the chosen turbulence model on the test cell, and comparing the predicted l with the experimental calibration for Λ given in equation (1.11). For example Sonin et al. (1986) made an attempt to determine the k-ε model length scale $L \equiv k^{3/2}/\varepsilon$ in the system of Figure 1.1 by fitting a one-dimensional analytic solution of the k-ε model to their data for the axial distribution of v. They obtained the result that $L \cong 1.1D$ for $3 < z/D < 4$, which suggested that $\Lambda_b \cong 0.22L$. Their calibration can, however, be criticized on the grounds that a one-dimensional model neglects radial diffusion of turbulent kinetic energy to the walls. Recently, Hasan and Lin (1989) solved the k-ε model for the complete axisymmetric system of Figure 1.1, including the entire flow field from the nozzle exit upward. Their results indicate that with the free surface at $s/D = 3.67$, L ranges from about 0.4D to 0.6D at the centerline, depending on depth below the interface, and drops to lower values near the walls. However, Hasan and Lin's calculations are not without problems of their own, and show what appear to be unrealistic predictions for large z/D. They apparently stem from the difficulty one encounters in applying proper boundary conditions for k and ε at the free surface. If the present correlation is to be applied to cases where the Richardson number is not small, a means of predicting Λ is required. Further work is clearly needed in order to establish the ratio between Λ and the length scales that appear in the turbulence models which are applicable to free surface problems.

References

Brown, J.S., Helmick, M.R. and Sonin, A.A., "Vapor Condensation at a Turbulent Liquid Surface in Systems with Possible Space-Based Applications," AIAA Paper 89-2846, 1989.

Brown, J.S., Khoo, B.C. and Sonin, A.A., "Rate Correlation for Condensation of Pure Vapor on Turbulent, Subcooled Liquid," *Int. J. Heat Mass Transfer*, Vol. 33, pp. 2001-2018, 1990.

Chun, J.-H., "Condensation Rate at Highly Agitated Steam-Water Interfaces," Ph.D. Thesis, Department of Mechanical Engineering, M.I.T., 1983.

Chun, J.-H., Shimko, M.A. and Sonin, A.A., "Vapor Condensation onto a Turbulent Liquid - II. Condensation Burst Instability at High Turbulence Intensities," *Int. J. Heat Mass Transfer*, Vol. 29, pp. 1333-1338, 1986.

CRC Handbook of Chemistry and Physics (Edited by R.C. Weast), CRC Press Inc., Boca Raton, Florida, 1984.

Coles, D., "The Law of the Wake in the Turbulent Boundary Layer," *J. Fluid Mech.*, Vol. 1, pp. 191-226, 1956.

Davies, J.T., Kilner, A.A. and Ratcliff, G.A., "The Effect of Diffusivities and Surface Films on Rates of Gas Absorption," *Chem. Engng Sci.*, Vol. 19, pp. 583-590, 1964.

Fortescue, G.E. and Pearson, J.R.A., "On Gas Absorption into a Turbulent Liquid," *Chem. Engng Sci.*, Vol, 22, pp. 1163-1176, 1967.

Hasan, M.M. and Lin, C.-S., "Axisymmetric Confined Turbulent Jet Directed Towards the Liquid Surface From Below," AIAA Paper 89-0172, 1989.

Helmick, M.R., Khoo, B.C., Brown, J.S. and Sonin, A.A., "Vapor Condensation Rate at a Turbulent Liquid Interface, for Application to Cryogenic Hydrogen," AIAA Paper 88-0559, 1988.

Helmick, M.R., "Vapor Condensation on a Turbulent Liquid Interface for Application in Low-Gravity Environments," S.M. Thesis, Departments of Mechanical and Nuclear Engineering, M.I.T., 1988.

Henstock, W.H. and Hanratty, T.J., "Gas Absorption by a Liquid Layer Flowing on the Wall of a Pipe," *A.I.Ch.E. Jl*, Vol. 25, pp. 122-131, 1979.

Hildebrand, J.H., "Motion of Molecules in Liquids: Viscosity and Diffusivity," *Science*, Vol. 174, pp. 490-493, 1971.

Hildebrand, J.H., *Viscosity and Diffusion: A Predictive Treatment*, Wiley, New York, 1977.

Hinze, J.O., *Turbulence*, 2nd Edition, McGraw-Hill, New York, 1975.

Hopfinger, E.J. and Toly, J.A., "Spatially Decaying Turbulence and its Relation to Mixing Across Density Interfaces," *J. Fluid Mech.*, Vol. 78, pp. 155-175, 1976.

Hopfinger, X.E. and Hopfinger, E.J., "On Mixing Across an Interface in Stably Stratified Fluid," *J. Fluid Mech.*, Vol. 166, pp. 227-244, 1986.

Jensen, R.J. and Yuen M.C., "Interphase Transport in Horizontal Stratified Concurrent Flow," U.S. Nuclear Regulatory Commission Report NUREG/CR-2334, 1982. Also in *Proc. 7th Int. Heat Transfer Conf.*, Vol. 5, pp. 95-100, 1982.

Khoo, B.C., "A Numerical and Experimental Study of the Scalar Transport at a Turbulent Liquid Free Surface," Ph.D. Thesis, Department of Mechanical Engineering, M.I.T., 1988.

Khoo, B.C., Patera, A.T. and Sonin, A.A., "Direct Numerical Simulation of Pure Vapor Condensation at a Turbulent Liquid Interface: an Extracted-Subdomain Approach." In *Heat Transfer With Phase Change* (Edited by I.S. Habib and R.N. Dallman), ASME HTD-Vol. 114, Book No. H00517, 1989.

King, C.J., "Turbulent Liquid Phase Mass Transfer at a Free Gas-Liquid Interface," *Ind. Engng Chem. Fundam.*, Vol. 5, pp. 1-8, 1966.

Kishinevsky, M.Kh., "Two Approaches to the Theoretical Analysis of Absorption Processes," *J. Appl. Chem. USSR*, Vol. 28, pp. 881-886, 1955 (translation pagination).

Komori, S., Ueda, H., Ogino, F. and Mizushina, T., "Turbulence Structure and Transport Mechanism at the Free Surface in an Open Channel Flow," *Int. J. Heat Mass Transfer*, Vol. 25, pp. 513-521, 1982.

Komori, S., Ueda, H., Ogino, F. and Mizushina, T., " Turbulence Structure in Stably Stratified Open-Channel Flow," *J. Fluid Mech.*, Vol. 130, pp. 13-26, 1983.

Kreith, F. and Black, W.Z., *Basic Heat Transfer*, Harper & Row, Publishers, New York, 1980.

Lamont, J.C. and Scott, D.S., "An Eddy Cell Model of Mass Transfer into the Surface of a Turbulent Liquid," *A.I.Ch.E. Jl*, Vol. 16, pp. 513-519, 1970.

Ledwell, J.J., "The Variation of the Gas Transfer Coefficient with Molecular Diffusivity." In *Gas Transfer at Water Surfaces* (Edited by W. Brutsaert and G.H. Jirka), pp. 293-302, Reidel, Dordrecht, 1984.

Levich, V.G., *Physicochemical Hydrodynamics*, Prentice-Hall, Englewood Cliffs, New Jersey, 1962.

Lienhard, J.H., *A Heat Transfer Textbook*, Prentice-Hall, Inc., Englewood Cliffs, New Jersey, 1981.

Mizushina, T., Ogino, F., Ueda, H. and Komori, S., "Buoyancy Effect on Eddy Diffusivities in Thermally Stratified Flow in an Open Channel," *Proc. 6th Int. Heat Transfer Conf.*, Vol. 1, pp. 91-96, 1978.

Ogino, F., "Turbulent Flow and Heat Transfer with Buoyancy Effect," *Proc. 8th Int. Heat Transfer Conf.*, Vol. 1, pp. 69-78, 1986.

Petukhov, B.S., "Heat Transfer and Friction in Turbulent Pipe Flow with Variable Physical Properties." In *Advances in Heat Transfer* (Edited by J.P. Hartnett and T.F. Irvine, Jr.), Vol. 6, pp. 503-564, Academic Press, New York, 1970.

Shimko, M.A., "Scalar Transport at a Turbulent Liquid Free Surface," S.M. Thesis, Department of Mechanical Engineering, M.I.T., 1985.

Sonin, A.A., Shimko, M.A. and Chun, J.-H., "Vapor Condensation onto a Turbulent Liquid - I. The Steady Condensation Rate as a Function of Liquid-Side Turbulence," *Int. J . Heat Mass Transfer*, Vol. 29, pp. 1319-1332, 1986.

Tennekes, H. and Lumley, J.L., *A First Course in Turbulence*, MIT Press, Cambridge, MA, 1972.

Theofanous, T.G., "Conceptual Models of Gas Exchange." In *Gas Transfer at Water Surfaces* (Edited by W. Brutsaert and G.H. Jirka), pp. 271-281, Reidel, Dordrecht, 1984.

Theofanous, T.G., Houze, R.N. and Brumfield, L.K., "Turbulent Mass Transfer at Free, Gas-Liquid Interfaces, with Application to Open-Channel, Bubble and Jet Flows," *Int. J. Heat Mass Transfer*, Vol. 19, pp. 613-624, 1976.

Thomas, R.M., "Condensation of Steam on Water in Turbulent Motion," *Int. J. Multiphase Flow*, Vol. 5, pp. 1-15, 1979.

Ueda, H., Moller, R., Komori, S. and Mizushina, T., "Eddy Diffusivity Near the Free Surface of Open Channel Flow," *Int. J. Heat Mass Transfer*, Vol. 20, pp. 1127-1136, 1977.

Wark, K., *Thermodynamics*, McGraw-Hill, New York, 1983.

Table 1.4. Raw data for Figures 1.14 – 1.16.

Pr_b	Pr_s	D	Re	Ri	Ja	St_o
1.5	1.3	0.102	2832	5.37	0.06	0.0107
1.5	1.3	0.102	2932	5.32	0.05	0.0099
1.5	1.3	0.102	3493	3.33	0.05	0.0145
1.5	1.3	0.102	3871	2.69	0.05	0.0139
1.5	1.3	0.102	4323	2.17	0.05	0.0145
1.5	1.3	0.102	4415	1.76	0.05	0.0156
1.5	1.3	0.102	5567	1.03	0.04	0.0168
1.5	1.3	0.102	6134	0.86	0.04	0.0154
1.5	1.3	0.102	7026	0.74	0.04	0.0162
1.5	1.3	0.102	8042	0.52	0.04	0.0165
1.5	1.3	0.102	10532	0.26	0.03	0.0168
2.2	1.3	0.102	2261	7.50	0.11	0.0089
2.2	1.3	0.102	2680	5.30	0.11	0.0105
2.2	1.3	0.102	3078	4.07	0.11	0.0120
2.2	1.3	0.102	3541	2.90	0.11	0.0123
2.2	1.3	0.102	4136	2.13	0.11	0.0131
2.2	1.3	0.102	4879	1.59	0.11	0.0137
2.2	1.3	0.102	5908	1.09	0.11	0.0140
2.2	1.3	0.102	6630	0.86	0.11	0.0148
2.2	1.3	0.102	8274	0.56	0.11	0.0147
2.2	1.3	0.102	9128	0.47	0.11	0.0150
2.2	1.7	0.102	3001	1.78	0.04	0.0140
2.2	1.7	0.102	3380	1.41	0.04	0.0136
2.2	1.7	0.102	3731	1.08	0.04	0.0146
2.2	1.7	0.102	4283	0.84	0.04	0.0144
2.2	1.7	0.102	4446	0.82	0.04	0.0148
2.2	1.7	0.102	4845	0.66	0.04	0.0153
2.2	1.7	0.102	5791	0.46	0.04	0.0150
2.2	1.7	0.102	6917	0.31	0.04	0.0153
2.55	1.3	0.102	1808	9.87	0.12	0.0066
2.55	1.3	0.102	2134	7.31	0.12	0.0100
2.55	1.3	0.102	2504	5.27	0.12	0.0104
2.55	1.3	0.102	2934	3.93	0.12	0.0116

Pr_b	Pr_s	D	Re	Ri	Ja	St_o
2.55	1.3	0.102	3080	3.48	0.12	0.0127
2.55	1.3	0.102	3209	3.10	0.12	0.0123
2.55	1.3	0.102	3970	2.15	0.12	0.0130
2.55	1.3	0.102	4568	1.55	0.12	0.0135
2.55	1.3	0.102	5392	1.12	0.12	0.0134
2.55	1.3	0.102	5737	0.98	0.12	0.0141
2.55	1.3	0.102	6500	0.80	0.12	0.0139
2.55	1.3	0.038	984	1.65	0.12	0.0140
2.55	1.3	0.038	1020	1.62	0.12	0.0127
2.55	1.3	0.038	1225	1.14	0.12	0.0139
2.55	1.3	0.038	1243	1.09	0.12	0.0130
2.55	1.3	0.038	1286	1.02	0.12	0.0137
2.55	1.3	0.038	1432	0.78	0.12	0.0131
2.55	1.3	0.038	1568	0.70	0.12	0.0139
2.55	1.7	0.102	1692	5.99	0.06	0.0094
2.55	1.7	0.102	2158	3.64	0.06	0.0124
2.55	1.7	0.102	2435	2.81	0.06	0.0130
2.55	1.7	0.102	2977	1.86	0.06	0.0129
2.55	1.7	0.102	3412	1.43	0.06	0.0138
2.55	1.7	0.102	4185	0.96	0.06	0.0131
2.55	1.7	0.102	4747	0.73	0.06	0.0137
2.55	1.7	0.102	5301	0.59	0.06	0.0146
2.55	1.7	0.102	6443	0.40	0.06	0.0142
3.15	1.3	0.102	806	37.26	0.15	0.0000
3.15	1.3	0.102	945	27.14	0.15	0.0032
3.15	1.3	0.102	1158	18.10	0.15	0.0043
3.15	1.3	0.102	1395	12.29	0.15	0.0065
3.15	1.3	0.102	1688	8.19	0.15	0.0087
3.15	1.3	0.102	2222	4.67	0.15	0.0107
3.15	1.3	0.102	2895	2.72	0.15	0.0124
3.15	1.3	0.102	3579	1.82	0.15	0.0126
3.15	1.3	0.102	4442	1.18	0.15	0.0127
3.15	1.3	0.102	4517	1.10	0.15	0.0129
3.15	1.3	0.102	5374	0.81	0.15	0.0135
3.15	1.3	0.102	5810	0.69	0.15	0.0129

Pr_b	Pr_s	D	Re	Ri	Ja	St_o
3.15	1.3	0.102	6074	0.62	0.15	0.0138
3.15	1.3	0.038	768	2.15	0.15	0.0119
3.15	1.3	0.038	855	1.71	0.15	0.0127
3.15	1.3	0.038	903	1.47	0.15	0.0127
3.15	1.3	0.038	1001	1.20	0.15	0.0134
3.15	1.3	0.038	1008	1.14	0.15	0.0126
3.15	1.3	0.038	1049	1.10	0.15	0.0123
3.15	1.3	0.038	1148	0.99	0.15	0.0128
3.15	1.3	0.038	1183	0.86	0.15	0.0138
3.15	1.3	0.038	1382	0.63	0.15	0.0136
3.15	1.3	0.038	1453	0.60	0.15	0.0136
3.15	1.3	0.038	1490	0.52	0.15	0.0133
3.15	1.7	0.102	1121	10.94	0.09	0.0068
3.15	1.7	0.102	1133	10.58	0.09	0.0060
3.15	1.7	0.102	1276	8.96	0.09	0.0890
3.15	1.7	0.102	1356	7.57	0.09	0.0082
3.15	1.7	0.102	1434	7.05	0.09	0.0090
3.15	1.7	0.102	1659	5.09	0.09	0.0100
3.15	1.7	0.102	1819	4.14	0.09	0.0103
3.15	1.7	0.102	1933	3.79	0.09	0.0097
3.15	1.7	0.102	2082	3.15	0.09	0.0108
3.15	1.7	0.102	2278	2.58	0.09	0.0116
3.15	1.7	0.102	2822	1.70	0.09	0.0125
3.15	1.7	0.102	3159	1.37	0.09	0.0124
3.15	1.7	0.102	3598	1.05	0.09	0.0129
3.15	1.7	0.102	3838	0.91	0.09	0.0132
3.15	1.7	0.102	4304	0.73	0.09	0.0131
3.15	1.7	0.102	4800	0.59	0.09	0.0134
3.15	1.7	0.102	5320	0.48	0.09	0.0133
3.15	1.7	0.038	763	1.26	0.09	0.0119
3.15	1.7	0.038	1010	0.72	0.09	0.0137
3.15	1.7	0.038	1258	0.47	0.09	0.0127
3.15	1.7	0.038	1344	0.40	0.09	0.0127
3.15	1.7	0.038	1501	0.33	0.09	0.0143

Pr_b	Pr_s	D	Re	Ri	Ja	St_o
4.65	1.3	0.102	402	59.23	0.19	0.0000
4.65	1.3	0.102	565	31.48	0.19	0.0025
4.65	1.3	0.102	716	19.54	0.19	0.0038
4.65	1.3	0.102	885	12.77	0.19	0.0052
4.65	1.3	0.102	1031	8.97	0.19	0.0069
4.65	1.3	0.102	1170	7.13	0.19	0.0087
4.65	1.3	0.102	1239	6.95	0.19	0.0087
4.65	1.3	0.102	1340	5.27	0.19	0.0101
4.65	1.3	0.102	1845	2.80	0.19	0.0109
4.65	1.3	0.102	2075	2.43	0.19	0.0111
4.65	1.3	0.102	2345	1.93	0.19	0.0115
4.65	1.3	0.102	2538	1.61	0.19	0.0116
4.65	1.3	0.102	2932	1.26	0.19	0.0111
4.65	1.3	0.102	3093	1.06	0.19	0.0117
4.65	1.3	0.102	3359	0.84	0.19	0.0117
4.65	1.3	0.038	427	3.26	0.19	0.0118
4.65	1.3	0.038	473	2.64	0.19	0.0109
4.65	1.3	0.038	534	2.17	0.19	0.0112
4.65	1.3	0.038	598	1.59	0.19	0.0119
4.65	1.3	0.038	643	1.34	0.19	0.0117
4.65	1.3	0.038	694	1.23	0.19	0.0110
4.65	1.3	0.038	730	1.06	0.19	0.0109
4.65	1.3	0.038	738	1.04	0.19	0.0119
4.65	1.3	0.038	754	1.04	0.19	0.0122
4.65	1.3	0.038	789	1.00	0.19	0.0108
4.65	1.3	0.038	842	0.78	0.19	0.0117
4.65	1.3	0.038	1004	0.55	0.19	0.0118
4.65	1.3	0.038	1099	0.48	0.19	0.0114
4.65	1.7	0.102	776	11.70	0.12	0.0051
4.65	1.7	0.102	826	9.85	0.12	0.0068
4.65	1.7	0.102	957	8.90	0.12	0.0082
4.65	1.7	0.102	973	7.49	0.12	0.0080
4.65	1.7	0.102	996	6.74	0.12	0.0075
4.65	1.7	0.102	1118	5.67	0.12	0.0095
4.65	1.7	0.102	1266	4.74	0.12	0.0094
4.65	1.7	0.102	1439	3.65	0.12	0.0111
4.65	1.7	0.102	1640	2.65	0.12	0.0107

Pr_b	Pr_s	D	Re	Ri	Ja	St_o
4.65	1.7	0.102	1934	1.79	0.12	0.0118
4.65	1.7	0.102	2304	1.42	0.12	0.0118
4.65	1.7	0.102	2426	1.13	0.12	0.0111
4.65	1.7	0.102	2854	0.93	0.12	0.0118
4.65	1.7	0.102	3027	0.73	0.12	0.0111
4.65	1.7	0.102	3378	0.62	0.12	0.0120
4.65	1.7	0.102	3748	0.50	0.12	0.0117
4.65	1.7	0.038	462	1.84	0.12	0.0108
4.65	1.7	0.038	574	1.16	0.12	0.0118
4.65	1.7	0.038	758	0.70	0.12	0.0121
4.65	1.7	0.038	899	0.48	0.12	0.0121
4.65	1.7	0.038	1004	0.39	0.12	0.0109
4.65	1.7	0.038	1030	0.34	0.12	0.0122

Part II

Nomenclature

A_c	interfacial area (m^2)
c_p	specific heat at constant pressure $(J\ kg^{-1}\ K^{-1})$
c_v	specific heat at constant volume $(J\ kg^{-1}\ K^{-1})$
d	nozzle exit diameter (m)
D	test cell inner diameter for axial jet system (m)
g	acceleration due to gravity $(m\ s^{-2})$
h	liquid depth in channel flow (m)
h_{fg}	latent heat of condensation $(J\ kg^{-1})$
Ja	Jakob number, equation (2.3)
$\langle K \rangle$	average condensation heat transfer coefficient, eqn. (2.20) $(J\ m^{-2}\ s^{-1}\ K^{-1})$
m	mesh spacing (m)
$\dot{m}$	condensation mass flux across interface $(kg\ s^{-1}\ m^{-2})$
$\dot{m}_{av}$	average condensation mass flux across interface $(kg\ s^{-1}\ m^{-2})$
p	pressure $(N\ m^{-2})$
Pr	Prandtl number
q	heat input into the vapor space resulting from use of wall heaters $(kg\ s^{-3})$
Q	volume flow rate circulating through system $(m^3\ s^{-1})$
$\dot{Q}$	heat input rate into the vapor space $(kg\ m^2\ s^{-3})$
r	radial coordinate (m)
r_*	radial location at which radial jet begins (m)
Re	Reynolds number, equation (2.6)
Re_g	Reynolds number in grid-channel flow, $Re_g \equiv U_g m/\nu$
Re_n	nozzle Reynolds number, $Re_n \equiv U_n d/\nu$
Ri	Richardson number, equation (2.5)
s	nozzle submergence in axial jet system (m)
St	Stanton number, equation (2.2)
t	time (s)
T	absolute temperature (K)
ΔT	liquid subcooling, $T_s - T_b$ (K)
ΔT_o	liquid subcooling at outflow, $T_s - T_o$ (K)
u	fluid velocity $(m\ s^{-1})$
U_g	superficial velocity in channel flow $(m\ s^{-1})$
U_m	maximum (centerline) mean velocity at elevation z associated with a turbulent free jet $(m\ s^{-1})$
U_n	nozzle exit velocity $(m\ s^{-1})$
U_s	mean velocity at the free surface due to turbulent radial jet $(m\ s^{-1})$
V	vapor volume (m^3)
V_b	liquid volume (m^3)
v_b	r.m.s. value of either the horizontal or vertical turbulent fluctuating velocity component extrapolated from the bulk liquid to the surface disregarding the interfacial layer $(m\ s^{-1})$

$(v_b)_{av}$	average value of v_b over the surface (m s^{-1})
y	coordinate measured vertically downward from the surface into the bulk liquid (m)
z	coordinate measured vertically upward from the nozzle exit into the bulk liquid (m)

Greek symbols

α	thermal diffusivity (m^2 s^{-1})
β	coefficient of thermal expansion (K^{-1})
β_1, β_2	empirical coefficients
δ	thermal layer thickness (m)
γ	ratio of specific heats
κ_T	isothermal compressibility (m s^2 kg^{-1})
Λ	integral turbulence length scale (m)
μ	viscosity (kg m^{-1} s^{-1})
ν	kinematic viscosity (m^2 s^{-1})
Π	dimensionless condensation rate parameter, equation (2.9)
ρ	density (kg m^{-3})
τ	characteristic time (s)
τ_c	steady-state or condensation controlled time (s)
τ_{mix}	turbulent mixing time (s)

Subscripts

b	liquid at bulk temperature (extrapolated to the interface)
g	vapor
n	nozzle exit plane in axial jet system
o	outflow conditions
s	liquid at saturation temperature

2.1. Introduction

Here the condensation rate correlation of Brown et al. (1990) is used to predict the transport rate in three different turbulent liquid flow systems in which the condensation rates have been measured, and is then compared with the experimental data. The first system is a vertical, cylindrical vessel in which turbulent mixing is induced by an axial submerged jet. This flow is of direct interest in space applications where it has been proposed as a way of controlling system pressure in cryogenic storage tanks in a micro-gravity environment [Aydelott (1967, 1976, 1979, 1983); Hochstein et al. (1987)]. The condensation rate and the flow field in an axial jet system have been studied by Thomas (1979) at low jet submergences and by Sonin et al. (1986), Helmick et al. (1988), and Brown et al. (1990) at high jet submergences. Some new data is presented here for low jet submergences. The second system is a horizontal channel flow with grid-induced turbulence studied by Thomas (1979). The third set of data is for transient condensation in a cylindrical system with an axial submerged jet providing the mixing. This flow is also of direct interest in space applications (e.g. filling of a closed cryogenic storage tank in a micro-gravity environment).

While all the data discussed here are from ground-based laboratory tests, comparisons are restricted to conditions of low Richardson number, where the local condensation rate per unit area at the liquid surface is not affected by buoyancy (i.e. gravitational) effects.

2.2. Local Condensation Rate Correlation

Brown et al. (1990) showed that at conditions where buoyancy effects are insignificant, the condensation mass flux of a pure vapor at the turbulent surface of its liquid is given by

$$St \cong 0.0198(1 - Ja/2)Pr_b^{-0.33} \qquad (2.1)$$

where

$$St \equiv \frac{\dot{m}h_{fg}}{\rho_b c_{pb} \Delta T v_b} \qquad (2.2)$$

is a condensation Stanton number based on the condensation heat flux $\dot{m}h_{fg}$, h_{fg} being the latent heat of condensation, ρ_b and c_{pb} the bulk liquid density and specific heat, ΔT the local bulk liquid subcooling and v_b the local r.m.s. value of the turbulent velocity fluctuations (see Brown et al. for more rigorous definitions of the local "bulk" values). Pr_b is the bulk liquid Prandtl number, and

$$Ja \equiv \frac{c_{pb}\Delta T}{h_{fg}} \qquad (2.3)$$

is the Jakob number based on bulk liquid subcooling. Equation (2.1) represents a data correlation valid for

$$\begin{gathered} Ri < 1 \\ 1 < Pr_s < 2 \\ 1 < Pr_b < 6 \\ Ja < 0.2 \\ 350 < Re < 11000 \end{gathered} \tag{2.4}$$

where Pr_s is the saturation liquid Prandtl number,

$$Ri \equiv \frac{g\beta_b \Delta T \Lambda_b}{v_b^2} \tag{2.5}$$

is the Richardson number, and

$$Re \equiv \frac{\rho_b v_b \Lambda_b}{\mu_b} \tag{2.6}$$

is the Reynolds numbers. Here β_b is the bulk liquid's coefficient of thermal expansion, g is the acceleration of gravity and Λ_b is a turbulent eddy macroscale which is defined more precisely by Brown et al. (1990).

Equation (2.1) applies only at small Richardson numbers (Ri < 1/2, say), where gravitational effects are negligible. Gravity gives rise to buoyancy effects which tend to dampen the turbulence near the interface and cause thermal stratification, thus reducing the condensation rate. The reduction becomes significant as the Richardson number approaches unity [Brown et al. (1990)].

Equation (2.1) provides an expression for the local condensation rate per unit surface area, at conditions where buoyancy effects are negligible, in terms of the local turbulence intensity and the local subcooling of the turbulent liquid flow. To apply the equation in a particular case with turbulent flow on the liquid side, one must first predict the turbulence intensity distribution at the liquid surface and then solve the energy equation for the fully turbulent flow on the liquid side, using equation (2.1) as the heat-flux boundary condition at the free surface. Equation (2.1) provides a heat transfer coefficient for the free surface, and allows the prediction of the condensation mass flux without the need to resolve the very thin thermal diffusion layer which actually occurs next to the interface.

2.3. Condensation Rate Correlation for Axial Jet System

The system shown on Figures 2.1 and 2.2. consists of a vertical pyrex tube of inside diameter D, partially filled with a liquid (tap water in this study) and with its vapor (steam in this study) supplied to the space above the liquid. A steady turbulence is created on the liquid side by circulating the liquid through an axial nozzle of diameter d, located at a submergence s below the interface. Cooling (warming) is provided by a tube and shell heat exchanger and a thermal steady state is assumed to be established. In what follows, it is assumed that the nozzle Reynolds number is high enough for the jet to be fully turbulent, and that the jet is small compared with the nozzle submergence ($d \ll s$), so that the turbulent velocity field on the liquid side is controlled only by the

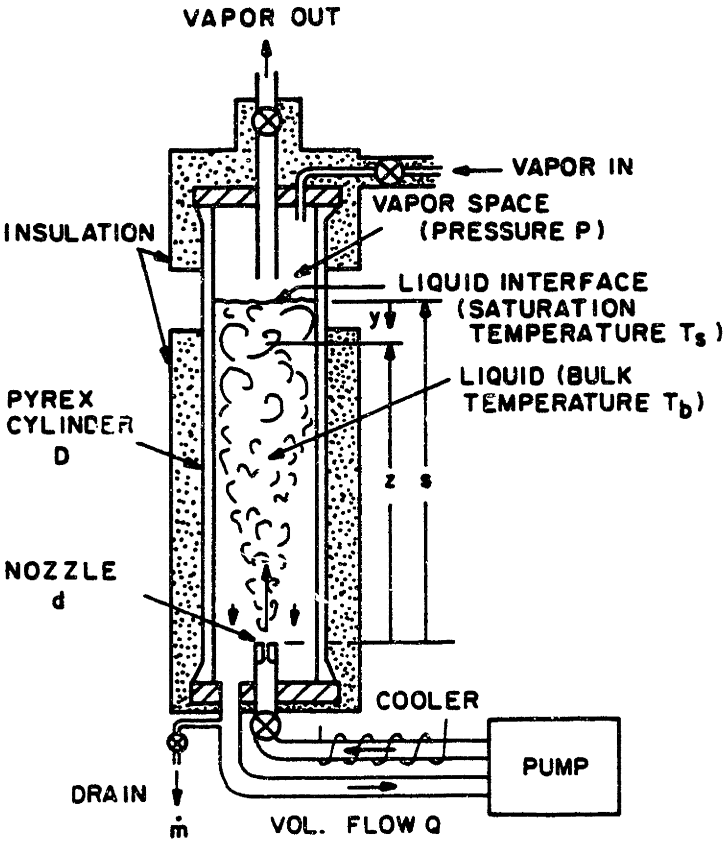

Figure 2.1. Axial jet system with large jet submergence (s/D > 3).

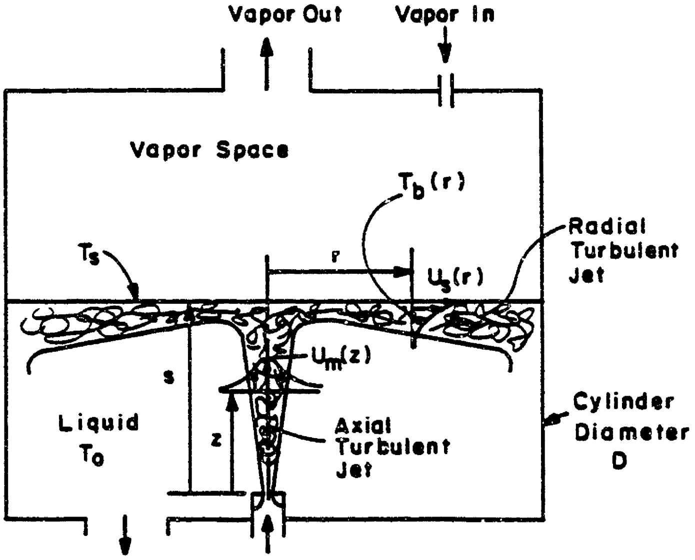

Figure 2.2. Axial jet system with small jet submergence (s/D < 1.3).

system geometry (D, d, s) and the nozzle momentum flow rate $\rho_b U_n^2 \pi d^2/4$, where U_n is the nozzle flow speed.

2.3.a. *High Nozzle Submergence*

With high nozzle submergence (s/D > 3), the jet spreads to fill the entire cross section before it reaches the interfacial region, as sketched in Figure 2.1, and the turbulence near the interface is fairly uniform over the cross section and approximately bulk-flow-free (i.e. the r.m.s. velocity is much greater than the mean velocity), with a characteristic macroscale proportional to the cylinder diameter D [Sonin et al. (1986); Brown et al. (1990)]. This is the system used by Sonin et al. and Brown et al. for establishing the local condensation rate correlation. The average turbulence intensity v_b over the free surface has been determined by Brown et al. to be

$$(v_b)_{av} = 21.1 \frac{Q}{Dd} \exp(-1.2s/D) \tag{2.7}$$

where Q is the volume flow rate circulating through the system. Equation (2.7) is based on data in the submergence range 3.1 < s/D < 4.2. Based on equations (2.1) and (2.7), the condensation rate can be expressed as

$$\Pi = 0.418 \exp(-1.2s/D) \tag{2.8}$$

where

$$\Pi \equiv \frac{\dot{m}_{av} h_{fg} D d \mathrm{Pr}_b^{0.33}}{\rho_b c_{pb} Q \Delta T_o (1 - \mathrm{Ja}/2)} \tag{2.9}$$

is a dimensionless system condensation rate, $\dot{m}_{av}$ being the average condensation mass flow rate per unit area at the interface, and

$$\Delta T_o \equiv T_s - T_o \tag{2.10}$$

is the subcooling of the bulk liquid, the temperature T_0 being the liquid temperature in the bulk and at the outflow point.

2.3.b. *Low Nozzle Submergence*

The case of low nozzle submergence ($s/D < 1.3$) has been investigated by Thomas (1979). Here the turbulent velocity field is quite different from the high nozzle submergence case, as shown in Figure 2.2. A turbulent jet spreads from the nozzle, but remains confined to the region near the system axis. The axial jet impinges on the free surface, which is kept approximately horizontal by gravity, and the bulk flow associated with it turns radially outward and forms a radial jet just below the interface. The radial jet thickens and loses mean velocity (as well as turbulence intensity) as it moves outward, and is eventually deflected down into the bulk liquid at the wall, after which it mixes with the bulk liquid below. Mean flow in the bulk liquid outside the jet regions is low, though of course some circulation and mixing does result from entrainment into the two jet regions and the return flow toward the outlet port.

In this case the turbulence intensity will vary significantly over the interface, and the condensation mass flux has to be evaluated by integrating equation (2.1) over the surface. The turbulence intensity has not been measured directly for low nozzle submergences, and must therefore be estimated by analysis. Following Thomas (1979), the turbulence intensity distribution $v_b(r)$ at the interface is modeled as

$$\begin{aligned} v_b &= \beta_1 U_m(s) && r < 0.343s \\ &= \beta_2 U_s(r) && 0.343s < r < D/2 \end{aligned} \qquad (2.11)$$

where

$$U_m(z) = 6.5 U_n d/z \qquad (2.12)$$

is the maximum (centerline) mean velocity at elevation z associated with a free turbulent jet at the axis, and

$$U_s(r) = 2.6 U_n d/r \qquad (2.13)$$

is the mean velocity at the interface associated with the radial turbulent jet. Equation (2.12) is derived from Rodi (1975), and has a coefficient slightly different from the one used by Thomas. Equation (2.13) is the expression obtained by Thomas.

β_1 and β_2 are empirical coefficients which express the fact that in a free turbulent shear flow the local turbulence intensity is expected to be some fraction of the maximum mean velocity excursion across the shear flow [Prandtl (1942)]. By analogy with other free flows, these coefficients are expected to be of order 0.1 – 0.3, say [Rodi (1975)]. The demarcation r/s = 0.343 which separates the axial and radial turbulent jets at the interface is slightly different from the value 0.3 suggested by Thomas. The present value conserves mass flow between the two jet regions where they meet, and fits Thomas' data about as well as his own value (see Appendix 2.A.).

The average value of the turbulence intensity v_b over the free surface is obtained from integrating equation (2.11) as

$$(v_b)_{av} = \frac{U_n d}{z}\left[10.4\beta_2 - \left(7.14\beta_2 - 3.06\beta_1\right) s/D\right] \tag{2.14}$$

The average condensation mass flux at the interface must be obtained by integrating equation (2.1)

$$\dot{m}_{av} h_{fg} = \rho_b c_{pb} \frac{4}{\pi D^2} \int_0^{D/2} St\, v_b(r)\left[T_s - T_b(r)\right] 2\pi r\, dr \tag{2.15}$$

Here, T_b is the local "bulk" temperature of the turbulent jet flow near the interface, as defined by Brown et al. (1990). $T_b(r)$ must in general be evaluated by solving the energy equation for the turbulent jet flows. That solution (see Appendix 2.A.) shows, however, that, provided $s \gg d$,

$$\Delta T = T_s - T_b(r) \cong \Delta T_o \qquad (2.16)$$

in this type of system, that is, the temperature of the liquid in the turbulent jet region near the surface is only slightly lower than that of the bulk liquid region below, with the difference being negligible as far as the subcooling is concerned. It follows that the average Stanton number for the system is simply the Stanton number based on ΔT_o and $(v_b)_{av}$. Alternatively, using equation (2.1) for St, equation (2.16) for ΔT and equation (2.11) for the turbulence intensity distribution, equation (2.15) can be integrated to obtain

$$\Pi \cong 0.26\beta_2 - (0.18\beta_2 - 0.077\beta_1)s/D \qquad (2.17)$$

where Π is defined by equation (2.9). Equation (2.17) should be valid for fully turbulent nozzle Reynolds numbers and for $s/D < 1.3$, the upper limit in Thomas' investigation of the flow field.

2.3.c. *General Correlation*

Equation (2.15) expresses the condensation rate in terms of an integral over St, v_b

and the local subcooling of the turbulent flow at the interface. At small Richardson number, St depends on bulk liquid Prandtl number alone, and the local subcooling is everywhere essentially equal to the bulk or outlet subcooling ΔT_0 (see Appendix 2.A.). Equation (2.1) thus reduces to an integral over the turbulence intensity alone. Now dimensional arguments show [Sonin et al. (1986)] that, provided the axial jet is fully turbulent and s » d, the average value of the turbulence intensity at the interface can be expressed in the form

$$(v_b)_{av} = \frac{Q}{Dd} f(s/D) \qquad (2.18)$$

where f is some function of s/D. Equation (2.15) thus suggests that the general correlation for the condensation rate, for arbitrary s/D, has the form

$$\Pi = \Pi(s/D) \qquad (2.19)$$

Equations (2.8) and (2.17) show that the dimensionless condensation rate Π declines linearly with s/D below 1.3, and exponentially at s/D between about 3 and 4.

2.4. Comparison with Experiment

2.4.a. *Thomas' Data*

For s/D < 1.3, equations (2.9) and (2.17) yield an average condensation heat transfer coefficient which can be written as

$$
\begin{aligned}
\langle K \rangle &\equiv \frac{\dot{m}_{av} h_{fg}}{\Delta T_o} \\
&= \frac{\mu_b c_{pb}}{D} Pr_b^{-0.33} (1 - Ja/2) Re_n \left[0.20\beta_2 - (0.14\beta_2 - 0.06\beta_1) s/D \right]
\end{aligned}
\tag{2.20}
$$

where $Re_n \equiv \rho_b U_n d/\mu_b$ is the nozzle Reynolds number, and μ_b is the liquid viscosity at the bulk (i.e. system outlet) temperature. Equation (2.20) predicts an average heat transfer coefficient directly proportional to nozzle Reynolds number, in agreement with Thomas' data [and in disagreement with the theoretical model of Theofanous et al. (1976), to which Thomas attempted to fit his data]. Figure 2.3 shows a comparison of all of Thomas' data with equation (2.20), with empirical coefficients taken as

$$
\beta_1 = 0.16 \text{ and } \beta_2 = 0.20 \tag{2.21}
$$

and the liquid properties evaluated at the nominal outlet temperature 91.6°C ($Pr_b = 1.9$). Thomas' system diameter was $D = 0.30$ m.

The best-fit β values are reasonable in the sense that equation (2.11) gives r.m.s. to mean velocity ratios typical of free turbulent flows [Rodi (1975)], and the agreement with the data is clearly excellent - the lines which represent equation (2.20) are virtually identical to the best-fit lines drawn by Thomas himself, the only exception being the case with s/D = 0.32, where the submergence was so low that significant surface breakup was observed at almost all operating conditions (the arrowheads on the abscissa indicate

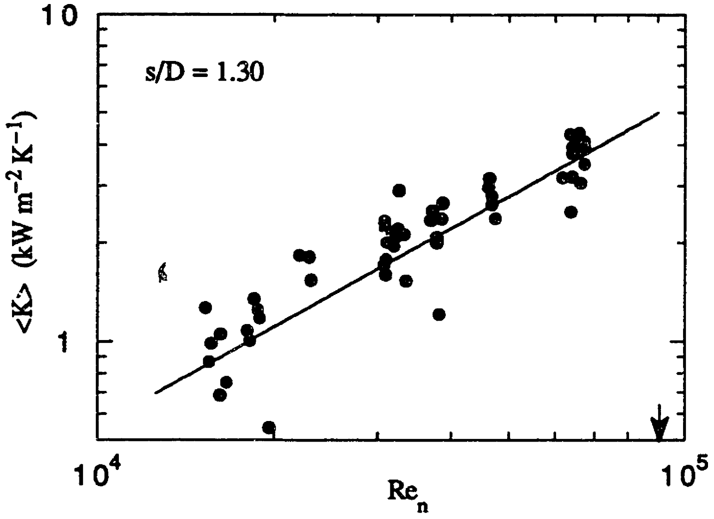

Figure 2.3.a. Thomas' axial jet system with s/D = 1.30. Solid line represents equation (2.20) with $\beta_1 = 0.16$ and $\beta_2 = 0.20$.

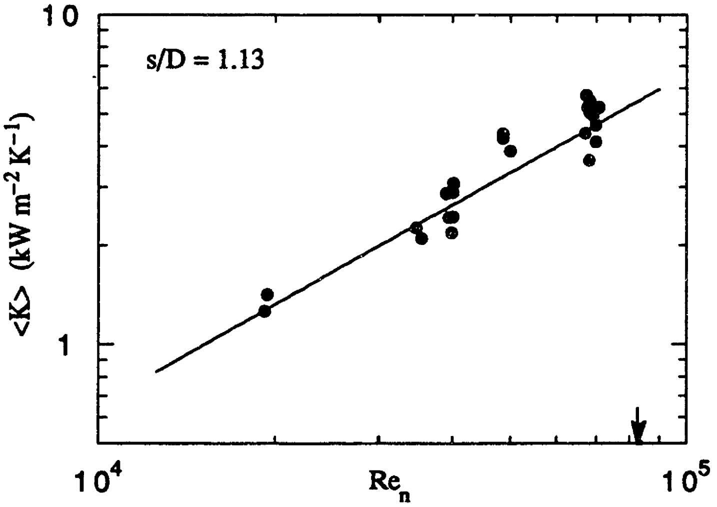

Figure 2.3.b. Thomas' axial jet system with s/D = 1.13. Solid line represents equation (2.20) with $\beta_1 = 0.16$ and $\beta_2 = 0.20$.

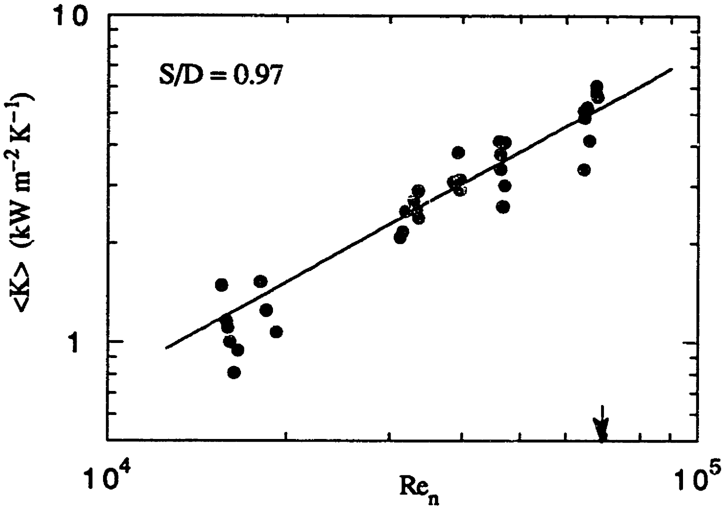

Figure 2.3.c. Thomas' axial jet system with s/D = 0.97. Solid line represents equation (2.20) with $\beta_1 = 0.16$ and $\beta_2 = 0.20$.

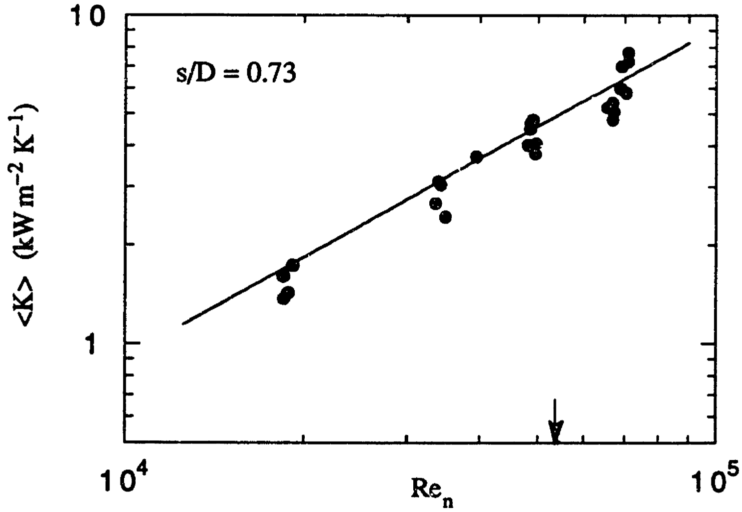

Figure 2.3.d. Thomas' axial jet system with s/D = 0.73. Solid line represents equation (2.20) with $\beta_1 = 0.16$ and $\beta_2 = 0.20$.

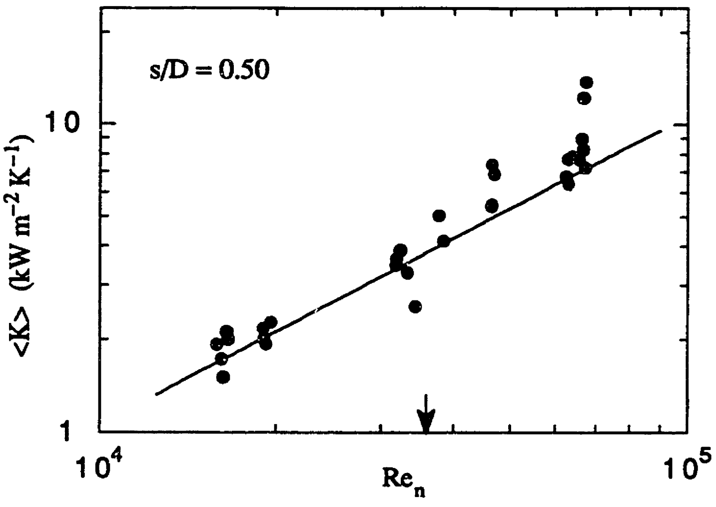

Figure 2.3.e. Thomas' axial jet system with s/D = 0.50. Solid line represents equation (2.20) with $\beta_1 = 0.16$ and $\beta_2 = 0.20$.

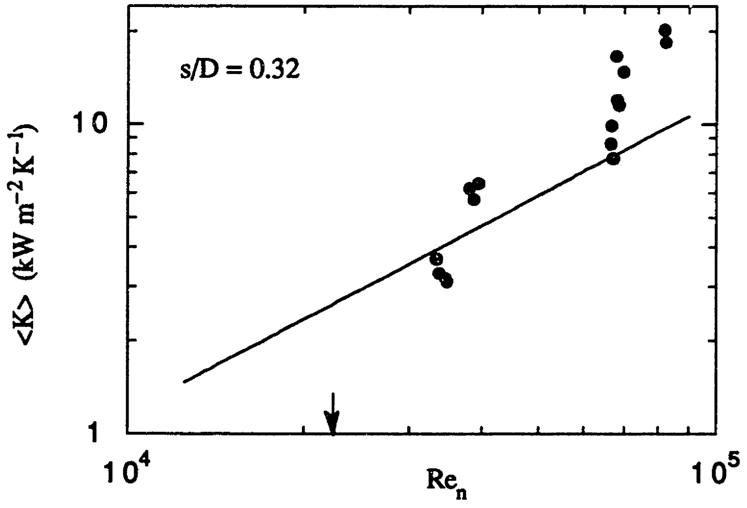

Figure 2.3.f. Thomas' axial jet system with s/D = 0.32. Solid line represents equation (2.20) with $\beta_1 = 0.16$ and $\beta_2 = 0.20$.

Thomas' estimate of the onset of surface breakup by the axial jet).

The Richardson number in Thomas' data is typically small. For example, at a nozzle Reynolds number of 4×10^4, which is at the midpoint of his data, one obtains Richardson numbers of the order of 0.1 – 1, based on the average v_b of equation (2.14) and a length scale taken as about 1/5 of the average radial jet thickness Λ defined by Thomas. The Richardson number may become significant at the lower Reynolds number end, but correcting for it becomes difficult without a more precise study of the macroscale distribution in this kind of a system, and it is not attempted here. There is in any case significant scatter in the data.

Figure 2.4 shows equation (2.20) replotted in terms of the dimensionless condensation rate Π of equation (2.9), with the coefficients taken from equation (2.21).

2.4.b. *Present Data*

Also shown on the "universal" correlation of Figure 2.4 [see equation (2.19)] is the line segment which corresponds to the Brown et al. (1990) data at higher submergences, $s/D > 3$, and $Ri = 0$, as given by equation (2.8), and some new data which have been taken with $s/D < 3$ in the larger of the two systems used by Brown et al. ($D = 0.102$ m).

The new data points for lower s/D were obtained with steam at 1.13 bar (T_s = 103°C), and water at bulk temperatures corresponding to Prandtl numbers in the range 2.3 to 5.1. Two nozzles were used in these new experiments, one with $D/d = 24$ as in Sonin et al. (1986), Helmick et al. (1988) and Brown et al. (1990), and the other with

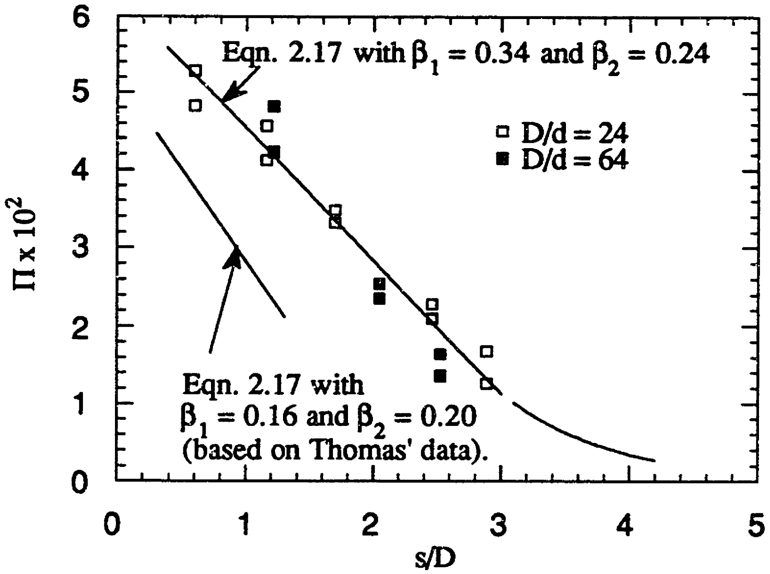

Figure 2.4. "Universal" submerged jet correlation.

D/d = 64. The two different nozzles give somewhat different correlations, possibly because s/d was not quite as large as it should have been to ensure that the surface was in the axial jet's far field [Rodi (1975)]. The major difference, however, occurs between the new data and that of Thomas. The present data at smaller s/D is correlated with equation (2.17) with the coefficients given by

$$\beta_1 = 0.34 \text{ and } \beta_2 = 0.24 \qquad (2.22)$$

which are significantly higher than equation (2.21). Based on the literature on free turbulent flows [e.g. Rodi (1975)], one would expect β_1 and β_2 to be universal coefficients, not system-dependent. It is possible that the difference between Thomas' data and the present data arises from inaccuracies in one or the other set of condensation rate measurements. Note, however, that the new data fair smoothly into the data of Brown et al. at higher s/D. Considerable care was taken by Brown et al. to minimize errors, and their correlation has also been confirmed with systems of different diameter (3.8 cm and 15.3 cm). In addition, Wygnanski and Fiedler (1969) measured the axial turbulence intensity for a free turbulent jet and found that $\beta_1 \cong 0.28 - 0.30$, in agreement with the current data.

Meserole et al. (1987) have presented some data for the condensation of Freon 11 in a 0.254 m diameter axial jet system with relatively low s/D. Their data is not included on Figure 2.4 because some assumptions are required to transform their published results to the current form, but it appears that their data fall somewhat below Thomas'. They do note, however, that their measurements may have suffered from the presence of noncondensable gases, which may have reduced the condensation rate.

2.5. Condensation in Horizontal Channel

One other flow system among those investigated by Thomas (1979) had low Richardson number conditions. This was a horizontal channel, 1.09 m long and 0.10 m wide, carrying water 0.05 m deep, and having turbulence produced mainly by a grid placed at the channel entrance. Based on hot-wire measurements, Thomas estimated the r.m.s. value of the flow-wise velocity fluctuations to be $(v_b)_{av} \cong 0.19U_g$ where U_g is the superficial flow speed in the channel. Again, the subcooling of the turbulent water was to a good approximation equal to the subcooling based on the outlet temperature, the temperature rise between the inlet and outlet being small compared with the subcooling.

Figure 2.5 compares Thomas' data with the correlation of Brown et al. (1990). The solid line on the figure corresponds to equations (2.1) and (2.2), with the average turbulence intensity taken as $0.13U_g$ rather than $0.19U_g$ as recommended by Thomas. This difference is not necessarily significant, considering (a) Thomas expressed doubts about the accuracy of his turbulence intensity measurement, (b) a channel flow has almost a factor of two higher flow-wise than vertical r.m.s. velocity

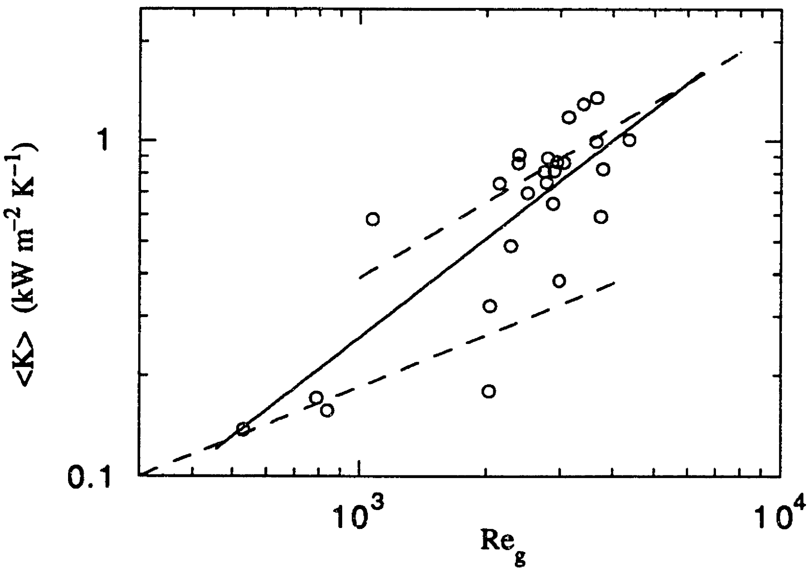

Figure 2.5. Thomas' horizontal channel flow with grid induced turbulence. Solid line represents equations (2.1) and (2.2) with average turbulence intensity taken as $0.13U_g$.

[Komori et al. (1982)], while Brown et al.'s condensation correlation is based on approximately isotropic liquid-side turbulence, and (c) there is considerable scatter in Thomas' data. The current prediction is almost identical to Thomas' own best-fit line (not shown). The broken lines represent Thomas' attempt to fit his data with the low and high Reynolds number versions of the correlation of Theofanous et al. (1976). The Richardson number for these data was small : based on the average turbulence intensity and a macroscale taken as one-fifth of the liquid level h, $Ri \cong 0.03$ at $Re_g = 4 \times 10^4$, where $Re_g \equiv U_g m/\nu$, and m is the mesh spacing.

2.6. Test Cell for Transient Condensation Experiments

The correlation described above is for systems operating in steady state. In order to investigate how well this correlation represents the instantaneous condensation rate under transient flow conditions, such as those which occur when a cylindrical tank is being filled with liquid via an axial nozzle, a series of tests were conducted in the system shown on Figure 2.6. The test cell being filled was a pyrex tube of inside diameter 15.3 cm with a 0.64 cm diameter nozzle [$D/d = 24$, as in the experiments of Sonin et al. (1986), Helmick et al. (1988) and Brown et al. (1989,1990)], connected to a similar smaller cell that was used to fill the larger one. Prior to a test, the water level in each cell was raised to an elevation close to that of the steam exhaust port, and then at least 50 system volumes of steam was flushed through each cell to purge them of any non-condensables. The water level in the 15.3 cm was then lowered to its operating level of

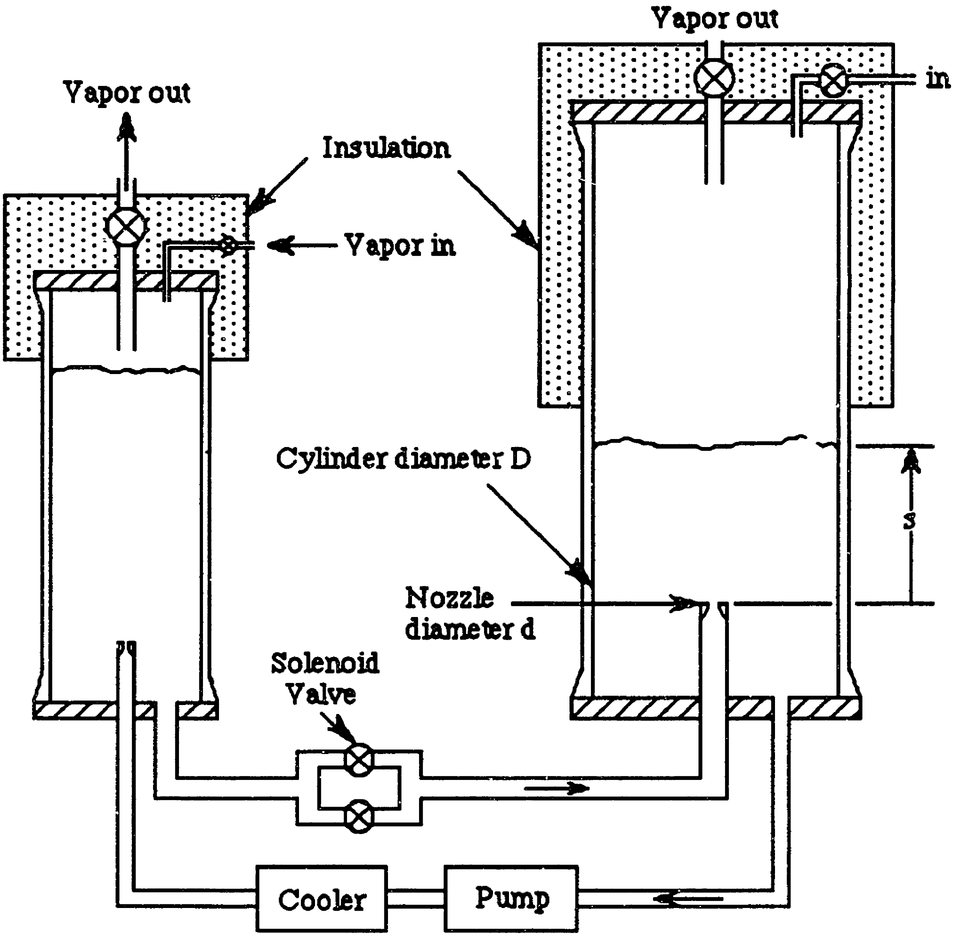

Figure 2.6. Schematic of test cell.

s/D = 1.0 and the water was circulated between the two cells through a heat exchanger and brought to a common initial temperature. The cells were then isolated from one another and the pump was turned off. The initial pressure in the 15.3 cm cell was adjusted to p (typically 0.15 MPa), while the pressure in the smaller driver cell was set at p + Δp (Δp typically 0.19 MPa), and both the inlet and outlet steam valves of the 15.3 cm cell were closed off. The large cell was able to maintain its initial pressure because the steam lines and the upper portion of the cell were heated with strip heaters and thoroughly insulated to prevent condensation from occurring away from the interface and also because the interfacial region contained a layer of stratified fluid of the order of 2 – 3 cm thick. The depressurization stage began when a solenoid valve was opened, allowing water to flow from the smaller cell into the larger one. The incoming liquid had to sweep the hot stratified layer away from the interfacial region before a quasi-steady condensation heat transfer process could be established (see Section 2.8). The volume flow rate Q entering the large cell through its nozzle would typically increase slightly with time as the pressure difference Δp increased as a result of condensation in the large cell; however, the initial Δp was chosen so that Q would remain approximately constant throughout the test.

Type T (copper-constantan) thermocouples enclosed in inconel sheaths (diameter 0.16 cm) with an accuracy of ±0.5 K were used to measure both the water and steam temperatures. A Bourdon tube gauge (0.0 – 0.3 MPa) was used to monitor the steady state system pressure and a differential pressure transducer (0.0 – 0.20 MPa), located on the water side, with a maximum time response of 1.0 ms, was used to record the time dependent system pressure. The differential pressure transducer was calibrated (Figure 2.7) at steady state and the data can be fitted with

$$p = 0.0343V - 0.0475 \qquad (2.23)$$

where V is the output of the transducer in volts and p has units of MPa.

The volume flow rate Q circulating through the nozzle of the 15.3 cm cell was measured using a differential pressure transducer whose output was directly proportional to the pressure drop across the nozzle. Figure 2.8 shows the results of the calibration and the data can be fitted with

$$\frac{Q}{Dd} = 0.187\sqrt{V} - 0.0096 \qquad (2.24)$$

where V is the output of the transducer in volts and Q/Dd has units of m/s.

The time varying system pressure p and the time varying flow velocity Q/Dd were recorded using a Masscomp 5450 computer.

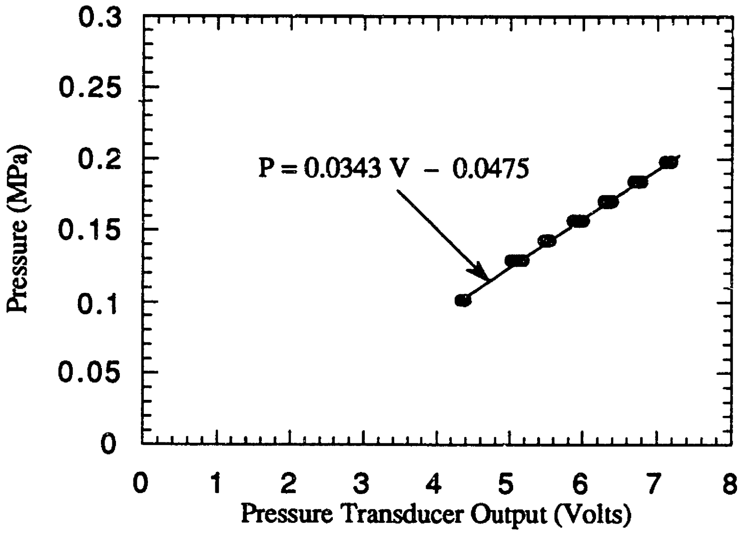

Figure 2.7. Differential pressure transducer calibration.

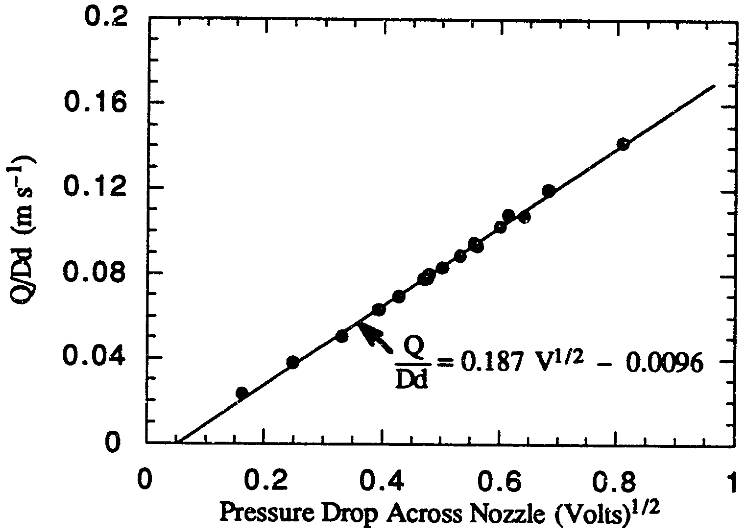

Figure 2.8. Flow rate calibration.

2.7. Scaling Relations for Transient Condensation Experiments

Consider a fixed amount of pure vapor, with temperature T_g and saturation temperature T_s, in contact with its subcooled autogenous liquid. The vapor is quiescent, but drifts toward the liquid surface, where it condenses and releases its latent heat h_{fg} to the liquid. The liquid is in turbulent agitation as the result of some mixing process or shear flow in the bulk of the liquid, deep below the surface, and not due to surface shear exerted by a horizontal vapor flow. The liquid-side turbulence and the condensation heat transfer process are not in statistically steady states, and the saturation temperature and pressure are changing as a result of condensation. The vapor space is subjected to an external heat source and the volume of the vapor space may change with time (e.g. as a result of filling).

With the above assumptions, system pressure is controlled mainly by what happens to the vapor phase. Using the energy and mass conservation equations and the thermal and caloric equations of state, the pressurization rate dp/dt and the temperature rise rate dT/dt of a homogenous vapor region with no mass inflow can be written as

$$\rho V \kappa_T \frac{c_v}{c_p}\frac{dp_s}{dt} = -\rho\frac{dV}{dt} + \frac{\dot{Q}\beta}{c_p} - \dot{m}_{av}A_c \tag{2.25}$$

$$\frac{dT_s}{dt} = -\frac{\beta T_s}{\rho\kappa_T c_v V}\frac{dV}{dt} + \frac{\dot{Q}}{\rho c_v V} - \frac{\beta T_s}{\rho^2 V \kappa_T c_v}\dot{m}_{av}A_c \tag{2.26}$$

where ρ is the vapor density, V is the vapor volume, κ_T is the vapor isothermal compressibility, c_v is the vapor specific heat at constant volume, c_p is the vapor specific heat at constant pressure, p_s is the vapor saturation pressure, t is time, β is the vapor coefficient of thermal expansion, $\dot{Q}$ is the heat input rate into the vapor space, T_s is the saturation temperature, $\dot{m}_{av}A_c$ is the total rate of mass loss from the vapor space due to condensation, A_c being the interfacial area and $\dot{m}_{av}$ being the average condensation rate over A_c. A complete set of equations is obtained if equations (2.25) and (2.26) are complemented with a heat input rate equation, with the required thermodynamic constitutive equations and with an interfacial condensation rate equation. The complete set can then be solved for the pressure change (and temperature change) as a function of time, for given system geometry, heat input rate, volume displacement rate – dV/dt and initial conditions.

Here equations (2.25) and (2.26) are not solved for specific cases, but are used to determine the scaling relations for the times that are involved. The analysis is for a system with a single axisymmetric jet which has been studied experimentally by Sonin et al. (1986) , Meserole et al. (1987) and Brown et al. (1989, 1990), and theoretically by Lin (1989). For an axial jet system operating in steady state, the condensation mass flux can be obtained for laminar jets from Lin, and for turbulent jets from Brown et al.'s empirical correlation. These rate equations are expressed in terms of the nozzle volume flow rate, the system geometry and the fluid properties. First consider the scaling for the characteristic time τ required to condense an initial volume of vapor V at constant volume assuming that the flow on the liquid side is in steady or quasi-steady state, both in terms of the flow field and in terms of the temperature distribution. Using the computational results of Lin (1989) for a laminar jet and the correlation of Brown et al. (1989) for a turbulent jet the following characteristic times τ, which are based on the interfacial condensation rate being the rate-limiting step, are obtained from equations (2.25) and (2.26):

Laminar jet:

$$\tau_c = \frac{\Delta p}{\gamma p} \frac{\rho}{\rho_b} \frac{h_{fg}}{c_{pb}(T_s - T_n)} \frac{V}{Q} \tag{2.27}$$

Turbulent jet:

$$\tau_c = \frac{\Delta p}{\gamma p} \frac{\rho}{\rho_b} \frac{h_{fg}}{c_{pb}(T_s - T_n)} \frac{V}{Q} \frac{4d}{\pi D} Pr_b^{0.33} \frac{1}{(1 - Ja/2)\Pi_1} \qquad (2.28)$$

Here the subscript "c" is used to denote the steady state, or condensation-controlled, estimate of the time, Δp is the change in system pressure, $\gamma \equiv c_p/c_v$ is the ratio of the vapor specific heats, p is the initial system pressure, ρ is the vapor density, ρ_b is the bulk liquid density, h_{fg} is the latent heat of condensation, c_{pb} is the bulk liquid specific heat, T_s is the saturation temperature, T_n is the temperature of the incoming liquid at the nozzle exit, V is the volume of the vapor space, Q is the volume flow rate circulating through the nozzle, d is the nozzle diameter, D is the test cell diameter, Pr_b is the bulk liquid Prandtl number, Ja is the Jakob number, Π_1 is the dimensionless function $\Pi(s/D)$ defined in equation (2.19), evaluated at $s/D = 1$ (a reference value, consistent with τ being a characteristic time) and s is the nozzle submergence. Equations (2.27) and (2.28) give characteristic times, which are scaling factors for the actual times in particular cases. The actual time in a particular case would be the characteristic time multiplied by some number of order unity. In addition, these equations are derived on the assumption that the steady-state condensation rate equations apply, which implies that the time required to attain steady state must be small compared with τ_c.

Since most systems of practical interest, as well as the experimental results in Section 2.8, fall into the turbulent flow regime, some further insight can be gained by comparing the relative magnitudes of τ_c computed on the assumption of steady state, and the time τ_{mix} required for turbulent mixing to determine which time is the rate-limiting one. The chemical engineering literature on mixing with turbulent jets suggests that τ_c is proportional to $V_b d/QD$, where V_b is the volume of the liquid in the system. The data obtained by Meserole et al. (1987) with an axial jet system shows that the coefficient is approximately unity, i.e.

$$\tau_{mix} \cong \frac{V_b}{Q}\frac{d}{D} \tag{2.29}$$

The ratio of the two time scales given in equations (2.28) and (2.29) is

$$\tau_c/\tau_{mix} \cong \frac{4}{\pi}\frac{\Delta p}{\gamma p}\frac{\rho}{\rho_b}\frac{h_{fg}}{c_{pb}\Delta T}\frac{V}{V_b}\frac{1}{\Pi_1}Pr_b^{0.33} \tag{2.30}$$

which is independent of Q/Dd and inversely proportional to the subcooling ΔT.

If the ratio in equation (2.30) is greater than unity, then mixing will occur faster than condensation, and the condensation will occur in a quasi-steady state. In other words, the condensation time will be controlled by the turbulent interfacial condensation rate. If on the other hand, the ratio in equation (2.30) is less than unity, then the actual condensation time will be controlled by the fluid mixing, that is, by the time it takes for the injected subcooled liquid to reach the interface, spread out over it, and mix the bulk liquid. Clearly, the characteristic time τ for condensation is controlled by the larger of the two quantities, that is,

$$\begin{aligned} \tau &\cong \tau_c \quad (\tau_{mix} < \tau_c) \\ &\cong \tau_{mix} \quad (\tau_{mix} > \tau_c) \end{aligned} \tag{2.31}$$

2.8. Transient Condensation Results

The experimental variables over which control was exercised were three: initial bulk liquid temperature T_b (via the heat exchanger), initial saturation temperature T_s (via system pressure) and the liquid-side flow velocity Q/Dd (via the pressure difference between the two cells).

Table 2.1 lists the initial conditions for experiments chosen from the three subcoolings investigated: $\Delta T \cong 80°C$, $\Delta T \cong 38°C$ and $\Delta T \cong 6°C$. These tests are typical examples chosen to illustrate the data. Table 2.2 lists the corresponding ratio τ_c/τ_{mix} for the same data.

Figure 2.9 shows a typical trace of system pressure vs. time when the wall heaters were not used. The broken line is the actual output from the pressure transducer and the solid line was calculated using equation (2.25), assuming $\dot{Q} = 0$ and that the condensation term is given by equation (2.17), which would be the case if $\tau_{mix} < \tau_c$. The slope of the depressurization portion of the "predicted" curve is approximately three times that of the actual data and the predicted final pressure is significantly lower than the measured value. One possible source of the error is the presence of

Table 2.1. Initial conditions for Figures 2.9 – 2.18.

Figure	Q/Dd	T_b (°C)	T_s (°C)	ΔT (°C)	P_s (MPa)
2.9	0.125	31	111	80	0.152
2.10 – 2.12	0.125	30	115	85	0.172
2.13 – 2.14	0.060	73	111	38	0.150
2.15 – 2.16	0.093	102	108	6	0.136
2.17 – 2.18	0.130	101	107	6	0.130

Table 2.2. τ_c/τ_{mix} for Figures 2.9 – 2.18.

Figure	τ_c/τ_{mix}
2.9	0.34
2.10 – 2.12	0.45
2.13 – 2.14	0.6
2.15 – 2.16	1.2
2.17 – 2.18	1.2

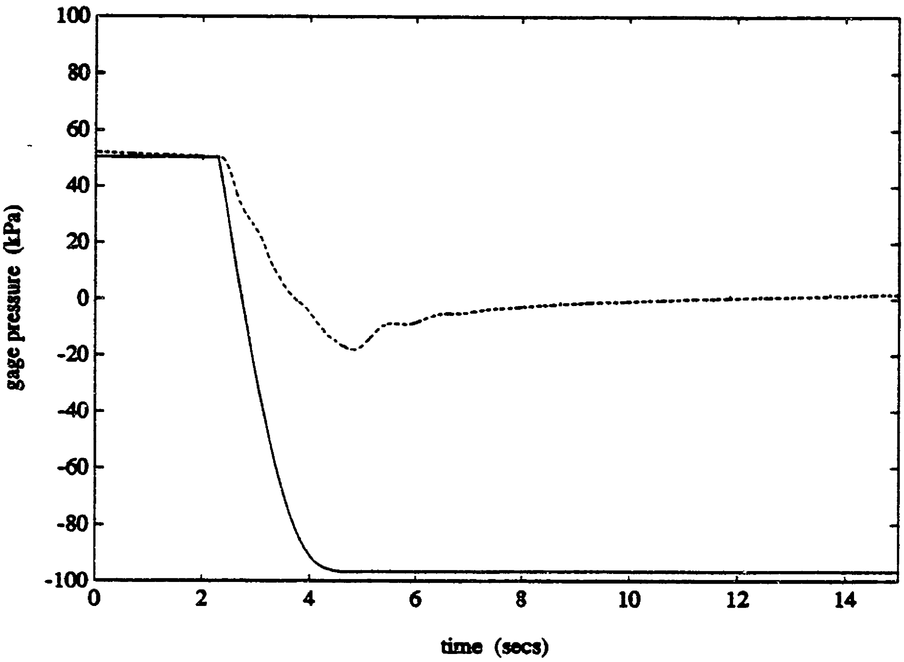

Figure 2.9. Broken line is a typical trace of system pressure vs. time when the wall heaters were not used and solid line is the predicted curve calculated using equation (2.25) with $\dot{Q} = 0$. See Tables 2.1 and 2.2 for conditions.

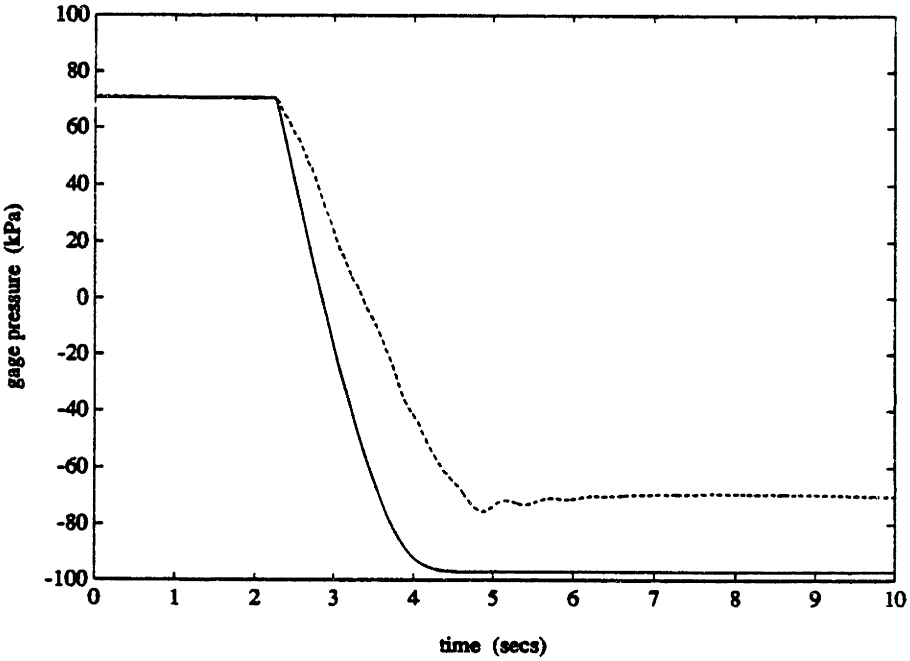

Figure 2.10. Experiment of Figure 2.9 repeated with the wall heaters turned on. See Tables 2.1 and 2.2 for conditions.

air or other non-condensable gases in the system. Hence, a simple test was performed to estimate the amount of air present in the system after it had been purged. The large test cell was flushed according to the procedure outlined in Section 2.6 and then the water level was lowered to s/D = 1.0. The initial system pressure was set and both the inlet and outlet steam valves were closed off. The pressure dropped as a result of condensation (caused by heat losses from the test cell), eventually dropping below atmospheric pressure. A valve was then opened allowing water to flow into the cell from a reservoir. After the flow had stopped, the system was full of water and void of any air, which suggested that air in the system was not the cause for the discrepancy between the measured and predicted data. Another possible source of the error is the evaporation, as the system pressure drops, of any condensate initially present on the cold walls. The experiment of Figure 2.9 was repeated, but this time the wall heaters were used (Figure 2.10). The slope of the depressurization portion of the predicted curve is now approximately twice that of the actual data and the predicted final pressure is much closer to the measured value. Thus, the discrepancy in Figure 2.9 between the predicted and measured curves is attributed at least in large measure to condensation of steam on the side walls prior to the start of depressurization and subsequent evaporation of that condensate.

All the data collected showed the same trend: the predicted depressurization rate calculated assuming that $\dot{Q} = 0$ was always greater than the measured depressurization rate, and the system pressure always increased after the flow had stopped.

Recall that the predicted pressure curves in Figures 2.9 and 2.10 were calculated using equation (2.25), and assuming that $\dot{Q} = 0$. This latter assumption is, however, an approximation since the side walls and the test cell ceiling were heated. A simple estimate of the heat input into the vapor space which resulted from the use of the heaters is given by

$$q = \frac{\alpha \rho c_p \Delta T}{\delta} \tag{2.32}$$

where α is the steam thermal diffusivity, ρ is the steam density, c_p is the steam specific heat at constant pressure, ΔT is the temperature difference between the wall and the bulk of the steam space and δ is the characteristic length over which the temperature drop occurs. As an approximation δ is taken from Rayleigh's solution which yields $\delta = \sqrt{\pi \alpha t}$, where t is time. Figure 2.11 shows the data of Figure 2.10, where the predicted curve has been corrected using equation (2.32) and assuming that the wall temperature is given by the temperature at which the heaters were set and that the bulk steam temperature is given by the saturation temperature. The predicted curve is in closer agreement with the measured data, but the slope of the predicted curve still overestimates the measured slope by about 60%. The ratio τ_c/τ_{mix} for Figures 2.10 and 2.11 is 0.45, so that according to equation (2.31) the condensation time is controlled by the mixing time and the steady state condensation rate correlation given in equation (2.17) will overestimate the actual condensation rate. Figure 2.12 shows the data of Figure 2.11 plotted as condensation mass flux vs. time. Some other measured data and predicted curves which have also been corrected using equation (2.32) are shown in Figures 2.13 and 2.14 for $\Delta T \cong 38°C$ and in Figures 2.15 – 2.18 for $\Delta T \cong 6°C$, plotted first as system pressure vs. time and then as condensation mass flux vs. time. In Figure 2.13, the slope of the predicted curve overestimates the measured slope by about 60% and the ratio τ_c/τ_{mix} is 0.6, so again the condensation time is controlled by the mixing time. Figure 2.14 shows the data of Figure 2.13 plotted as condensation mass flux vs. time. The agreement between the measured and predicted pressure curves in Figures 2.15 – 2.18 is clearly excellent. Here the ratio τ_c/τ_{mix} is 1.2 and according to equation (2.31) the condensation rate correlation of equation (2.17) should apply. Hence, agreement between the computed and measured curves may be expected if

$$\tau_c/\tau_{mix} > 1 \qquad (2.33)$$

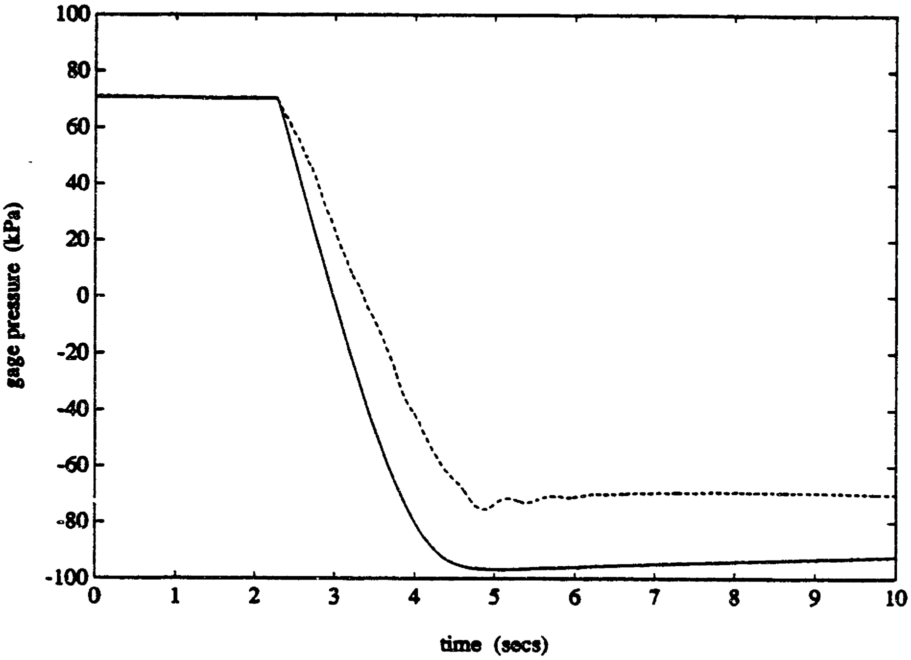

Figure 2.11. Data of Figure 2.10 where the predicted pressure curve has been corrected using equation (2.32). See Tables 2.1 and 2.2 for conditions.

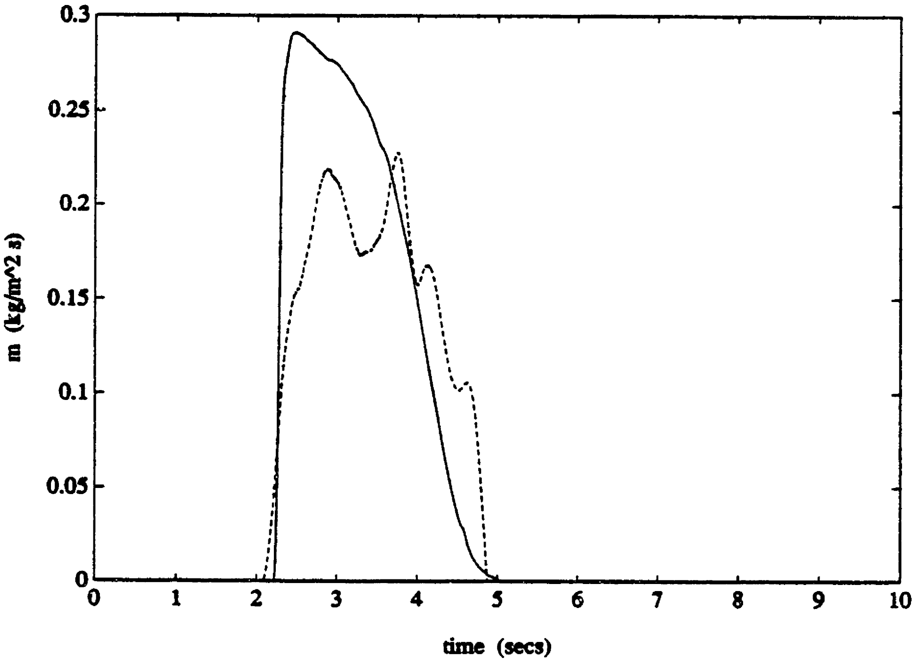

Figure 2.12. Data of Figure 2.11 plotted as $\dot{m}_{av}$ vs. time. See Tables 2.1 and 2.2 for conditions.

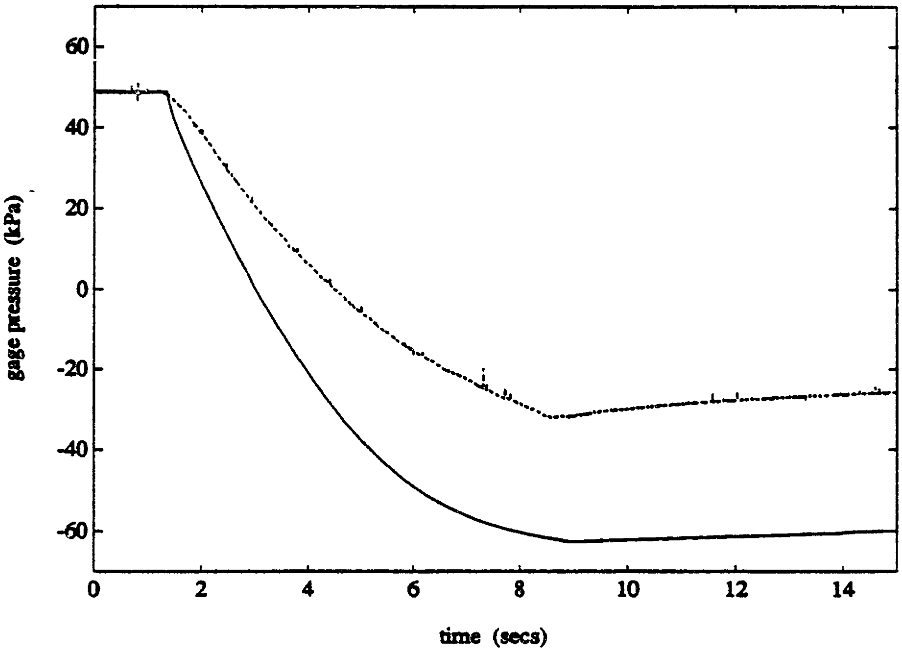

Figure 2.13. Broken line is a typical system pressure vs. time for ΔT ≅ 38°C. Solid line is the predicted pressure curve corrected using equation (2.32). See Tables 2.1 and 2.2 for conditions.

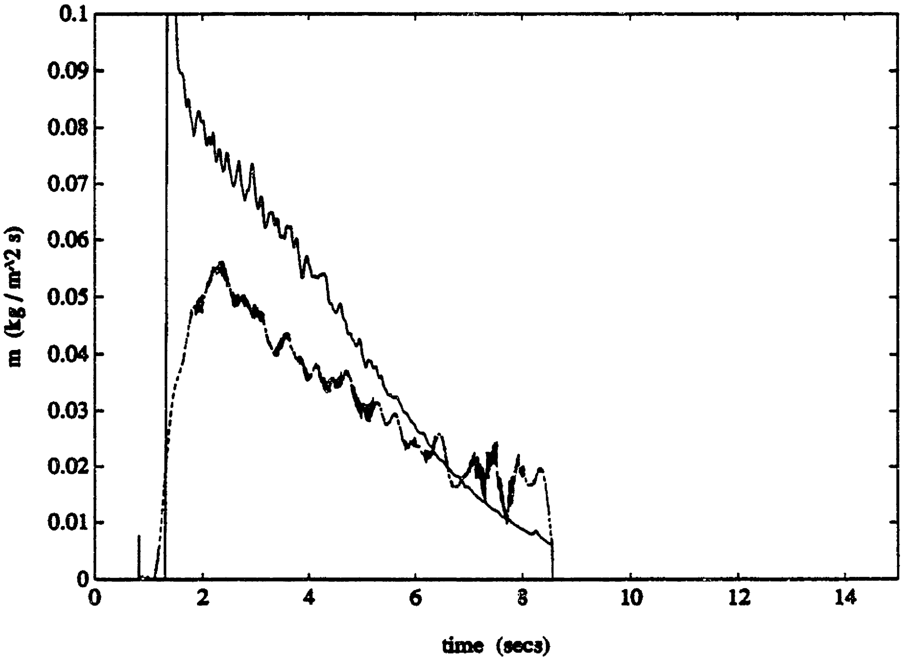

Figure 2.14. Data of Figure 2.13 plotted as $\dot{m}_{av}$ vs. time. See Tables 2.1 and 2.2 for conditions.

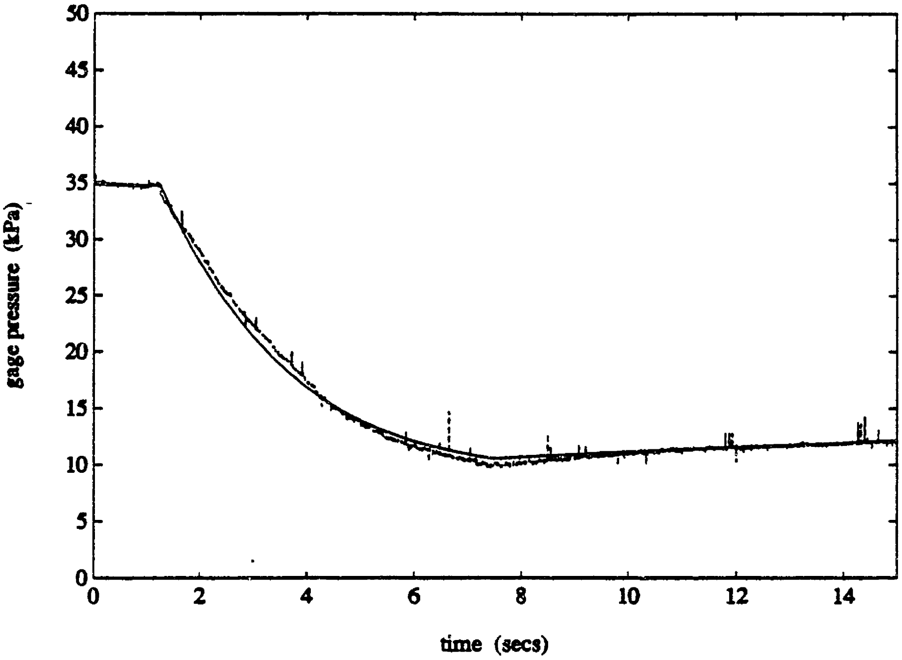

Figure 2.15. Broken line is a typical system pressure vs. time for $\Delta T \cong 6°C$. Solid line is the predicted pressure curve corrected using equation (2.32). See Tables 2.1 and 2.2 for conditions.

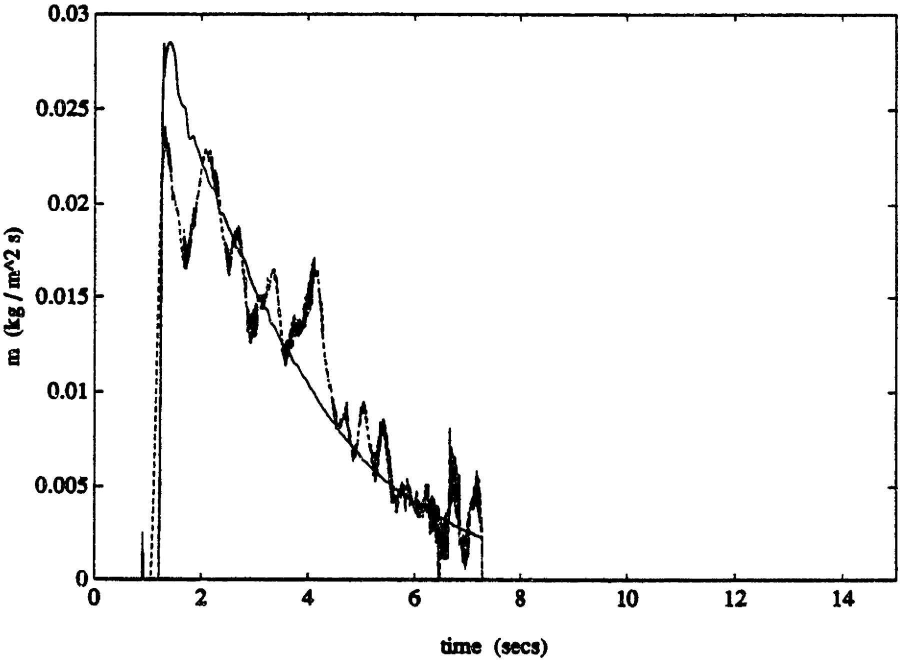

Figure 2.16. Data of Figure 2.15 plotted as $\dot{m}_{av}$ vs. time. See Tables 2.1 and 2.2 for conditions.

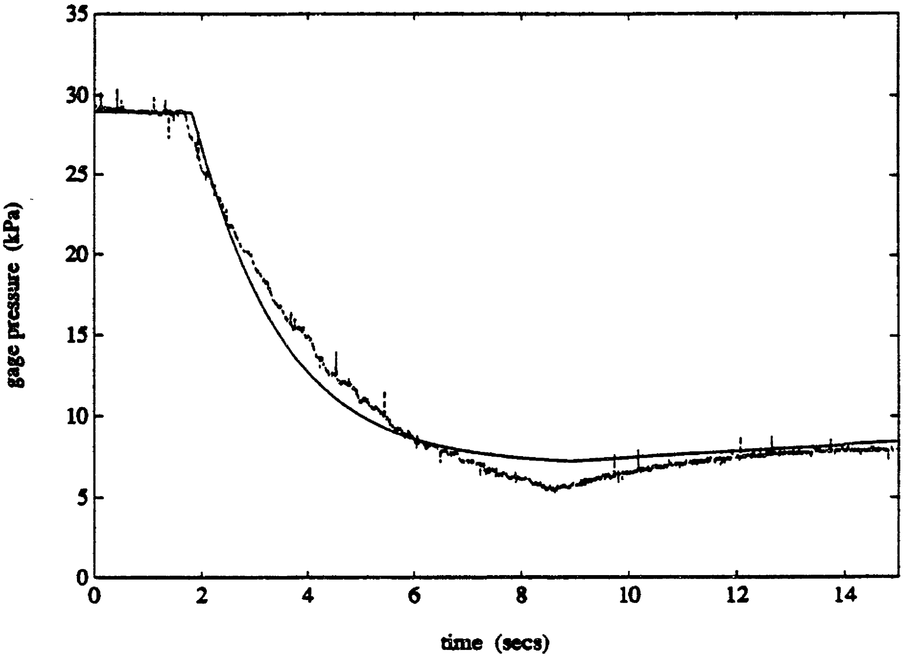

Figure 2.17. Broken line is another typical system pressure vs. time for $\Delta T \cong 6°C$. Solid line is the predicted pressure curve corrected using equation (2.32). See Tables 2.1 and 2.2 for conditions.

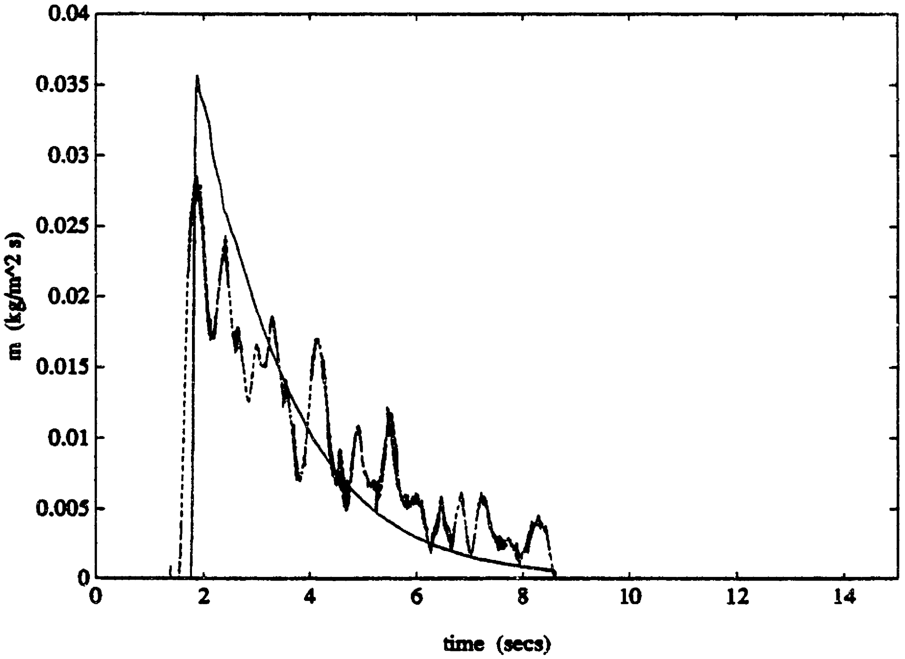

Figure 2.18. Data of Figure 2.17 plotted as $\dot{m}_{av}$ vs. time. See Tables 2.1 and 2.2 for conditions.

2.9. Concluding Remarks

The condensation rate correlation of Brown et al. (1990), equations (2.1) and (2.2), has been compared with data from three different systems in which pure vapor was condensed on a turbulent liquid surface. The agreement is good for steady state systems and also for transient systems when $\tau_c/\tau_{mix} > 1$. All the data support the linear dependence of the condensation rate on the r.m.s. value of the fluctuating velocity, and where the turbulence intensity has had to be estimated in order to apply the rate correlation, absolute agreement is obtained with very reasonable modeling assumptions.

Brown et al.'s correlation is in universal dimensionless form. When coupled with a model for the turbulent flow field and mean temperature distribution on the liquid side, it will in principle yield a prediction for the condensation rate in any system with any working fluid.

References

Aydelott, J.C., "Normal Gravity Self-Pressurization of 9-inch- (23-cm) Diameter Spherical Liquid Hydrogen Tankage," NASA TN D-4171, 1967.

Aydelott, J.C., "Axial Jet Mixing of Ethanol in Spherical Containers during Weightlessness," NASA TM X-3380, 1976.

Aydelott, J.C., "Axial Jet Mixing of Ethanol in Cylindrical Containers during Weightlessness," NASA TP-1487, 1979.

Aydelott, J.C., "Modeling of Space Vehicle Propellant Mixing," NASA TP-2107, 1983.

Aydelott, J.C. and Rudland, R.S., "Technology Requirements to be Addressed by the NASA Lewis Research Center Cryogenic Fluid Management Facility Program," AIAA Paper 85-1229, 1985.

Aydelott, J.C., Carney, M.J. and Hochstein, J.I., "NASA Lewis Research Center Low-Gravity Fluid Management Technology Program, " NASA Technical Memorandum 87145. Also AIAA/GNOS Paper 85-002, 1985.

Brown, J.S., Khoo, B.C. and Sonin, A.A., "Rate Correlation for Condensation of Pure Vapor on Turbulent, Subcooled Liquid," *Int. J. Heat Mass Transfer*, Vol. 33, pp. 2001-2018, 1990.

CRC Handbook of Chemistry and Physics (Edited by R.C. Weast), CRC Press Inc., Boca Raton, Florida, 1984.

Hasan, M.M. and Lin, C.-S., "Axisymmetric Confined Turbulent Jet Directed Towards the Liquid Surface From Below," AIAA Paper 89-0172, 1989.

Helmick, M.R., Khoo, B.C., Brown, J.S. and Sonin, A.A., "Vapor Condensation Rate at a Turbulent Liquid Interface, for Application to Cryogenic Hydrogen," AIAA Paper 88-0559, 1988.

Hinze, J.O., *Turbulence*, 2nd Edition, McGraw-Hill, New York, 1975.

Hochstein, J.I., Ji, H.-C. and Aydelott, J.C., "Temperature Fields Due to Jet Induced Mixing in a Typical OTV Tank," AIAA Paper 87-2017, 1987.

Komori, S., Ueda, H., Ogino, F. and Mizushina, T., "Turbulence Structure and

Transport Mechanism at the Free Surface in an Open-Channel Flow," *Int. J. Heat Mass Transfer*, Vol. 25, pp. 513-521, 1982.

Kreith, F. and Black, W.Z., *Basic Heat Transfer*, Harper & Row, Publishers, New York, 1980.

Lin, C.-S., "Numerical Studies of the Effects of Jet-Induced Mixing on Liquid-Vapor Interface Condensation," AIAA Paper 89-1744, 1989.

Meserole, J.S., Jones, O.S., Brennan, S.M. and Fortini, A., "Mixing-Induced Ullage Condensation and Fluid Destratification," AIAA Paper 87-2018, 1987.

Prandtl, L., "Bemerkungen zur Theorie der freien Turbulenz," *Zeitschrift fur angewandte Mathematik und Mechanik*, Vol. 22, pp. 241-243, 1942.

Rodi, W., "A Review of Experimental Data of Uniform Density Free Turbulent Boundary Layers," in *Studies in Convection* (Edited by B.E. Launder), pp. 79-165, Academic Press, New York, 1975.

Schlichting, H., *Boundary Layer Theory*, 7th Edition, McGraw-Hill, New York, 1979.

Sonin, A.A., Shimko, M.A. and Chun, J.-H., "Vapor Condensation onto a Turbulent Liquid - I. The Steady State Condensation Rate as a Function of Liquid-Side Turbulence," *Int. J. Heat Mass Transfer*, Vol. 29, pp. 1319-1332, 1986.

Theofanous, T.G., Houze, R.N. and Brumfield, L.K., "Turbulent Mass Transfer at Free, Gas-Liquid Interfaces, with Application to Open-Channel, Bubble, and Jet Flows," *Int. J. Heat Mass Transfer*, Vol. 19, pp. 613-624, 1976.

Thomas, R.M., "Condensation of Steam on Water in Turbulent Motion," *Int. J. Multiphase Flow*, Vol. 5, pp. 1-15, 1979.

Wark, K., *Thermodynamics*, McGraw-Hill, New York, 1983.

Wygnanski, I. and Fiedler, H., "Some Measurements in the Self-Preserving Jet," *J. Fluid Mech.*, Vol. 38, pp. 577-612, 1969.

Appendix 2.A.

Thomas (1979) has shown that for s/D < 1.3, the axial jet system produces a flow field like the one sketched in Figure 2.2. There is a vertical, or axial, turbulent jet near the centerline. When it reaches the interface this jet turns itself into a radial turbulent jet. The radial jet thickens and slows with increasing r, and eventually is deflected down at the cylinder wall, and is mixed with the bulk liquid below. If the vertical jet is modeled as an unconfined axisymmetric jet in an infinite atmosphere, its maximum axial mean speed will be given by equation (2.12), and its volume flow rate at an elevation z will be [Rodi (1975)]

$$Q_z(z) = \int_0^\infty u 2\pi r dr = 0.363 U_n dz \qquad (2.A.1)$$

In the radial jet region, Thomas' data for the mean radial velocity can be fitted with the equation

$$u(y,r) = U_s(r) \exp(-15.4y/r) \qquad (2.A.2)$$

where U_s, the mean radial velocity at the interface (Figure 2.2), is given by equation (2.13) and y is the depth below the interface. Equations (2.A.2) and (2.13) yield the radial volume flow rate per unit breadth as

$$Q_r(r) = \int_0^\infty u dy = 0.169 U_n d \qquad (2.A.3)$$

The radial jet begins at some point r_* which may be estimated by the requirement that the vertical volume flow rate in the axial jet at $z = s$ is equal to the total radial volume flow rate at $r = r_*$, that is,

$$Q_r(r_*) 2\pi r_* = Q_z(s) \qquad (2.A.4)$$

This yields

$$r_* = 0.343s \qquad (2.A.5)$$

which is somewhat higher than the value $r_* = 0.3s$ suggested by Thomas.

The temperature in the jet regions can be estimated by applying the energy equation. For the present purposes it is adequate to model the jet regions as having a uniform mean temperature T over their (axial or radial) cross sections. It is also assumed that the temperature in the liquid outside the jet regions is well mixed at a temperature T_o.

With equation (2.A.1), an energy balance applied to the axial jet yields

$$T_o - T(z) = (T_o - T_n)(2.17d/z) \qquad (2.A.6)$$

where T_n is the nozzle exit temperature. Equation (2.A.6) shows that, because of entrainment of hot fluid at temperature T_o, the liquid in the axial jet will reach a temperature much closer to T_o than to T_n by the time it reaches the surface (not the assumption $s \gg d$).

The energy equation for the radial jet has a source term from the condensation heat flux at the interface:

$$\frac{1}{r}\frac{d}{dr}\left[(T_o - T(r))\,Q_r(r)\,r\right] = -\frac{\dot{m}h_{fg}}{\rho_b c_{pb}} \qquad (2.A.7)$$

where, according to equations (2.2) and (2.11),

$$\frac{\dot{m}h_{fg}}{\rho_b c_{pb}} = 2.6\beta_2 \mathrm{St}\frac{U_n d}{r}\left[\Delta T_o + (T_o - T(r))\right] \qquad (2.A.8)$$

With $Q_r(r)$ taken from equation (2.A.3), the solution of equations (2.A.7) and (2.A.8) is

$$\frac{T_o - T(r)}{\Delta T_o} = \frac{15.4\beta_2 \mathrm{St}}{1 + 15.4\beta_2 \mathrm{St}}\left[\left(\frac{D}{2r}\right)^{1 + 15.4\beta_2 \mathrm{St}} - 1\right] \qquad (2.A.9)$$

Equations (2.A.6) and (2.A.9) give the temperature distribution in the turbulent jet regions near the interface, equation (2.A.6) applying at $r < 0.343s$ and equation (2.A.9) at $r > 0.343s$. The temperature T_o of the bulk liquid can be determined straightforwardly in terms of the nozzle exit temperature T_n: one needs only equate the enthalpy outflow rate in the radial jet at $r = 0.343s$ to the sum of the vertical enthalpy flow rate in the axial jet at $z = s$ and the condensation heat input from the interface at

$r < 0.343s$. For the present purposes, however, it suffices to note that the quantity $15.4\beta_2 St$ will be small compared with unity, since $St = O(10^{-2})$ and $\beta_2 = O(10^{-1})$. Equation (2.A.9) therefore implies that $(T_o - T) \ll \Delta T_o$ everywhere at the surface. In other words, the subcooling of the turbulent liquid is essentially constant everywhere and given by

$$\Delta T \equiv T_s - T(r) \cong \Delta T_o \qquad (2.A.10)$$

This is the assumption that was used to derive equation (2.17).

Table 2.3. Raw data for Figure 2.4.

Pr_b	Pr_s	D	D/d	s/D	Re_n	Ja	Π
2.3	1.7	0.102	24	1.70	16300	0.05	0.0174
2.5	1.7	0.102	24	2.89	34800	0.06	0.0063
2.6	1.7	0.102	24	1.16	13900	0.06	0.0228
2.6	1.7	0.102	24	0.60	7700	0.06	0.0264
2.9	1.7	0.102	24	1.16	10300	0.08	0.0206
3.1	1.7	0.102	24	2.46	20700	0.09	0.0105
3.1	1.7	0.102	24	2.89	36100	0.08	0.0084
3.7	1.7	0.102	24	0.60	6500	0.10	0.0241
4.1	1.7	0.102	24	1.70	10400	0.11	0.0166
4.9	1.7	0.102	24	2.46	12100	0.13	0.0105
5.1	1.7	0.102	24	2.46	13000	0.13	0.0114
2.5	1.7	0.102	64	1.21	10600	0.06	0.0241
2.6	1.7	0.102	64	2.04	16600	0.06	0.0118
2.7	1.7	0.102	64	1.21	12000	0.07	0.0211
2.9	1.7	0.102	64	2.52	23600	0.08	0.0068
3.3	1.7	0.102	64	2.04	15300	0.09	0.0127
4.1	1.7	0.102	64	2.52	17600	0.11	0.0082

Part III

Nomenclature

d	nozzle exit diameter (m)
D	test cell inner diameter (m)
f	physical frequency of the disturbance (s^{-1})
l	laminar length, Figure 3.3 (m)
l_n	nozzle length (m)
Q	volume flow rate circulating through system, Figure 3.1 ($m^3\ s^{-1}$)
Re_n	nozzle Reynolds number, $U_n d/\nu$
s	nozzle submergence, Figure 3.1 (m)
U_n	nozzle exit velocity ($m\ s^{-1}$)
z	distance from nozzle exit to liquid level in constant-head tank (m)

Greek symbols

β	dimensionless frequency, equation (3.2)
ν	kinematic viscosity ($m^2\ s^{-1}$)

3.1. Introduction

The critical Reynolds number at which an axisymmetric submerged jet undergoes transition from laminar to turbulent flow conditions is of fundamental interest in transport problems, because the enhanced mixing associated with turbulent flow leads to increased transport rates.

Linear stability theory has been applied to submerged 2-D jets by Curle (1957), Howard (1958), Tatsumi and Kakutani (1958) and Clenshaw and Elliott (1960) and to axisymmetric jets by Batchelor and Gill (1962) and Mollendorf and Gebhart (1973). The critical Reynolds number for transition from stable to unstable flow for 2-D jets was found to be Re ~ 4 and for axisymmetric jets was found to be Re ~ 40. Experimental investigations of the stability of submerged jets were conducted for the 2-D case by Sato and Sakao (1964) and for the axisymmetric case by Viilu (1962), Reynolds (1962), McNaughton and Sinclair (1966) and Mollendorf and Gebhart (1973). The critical Reynolds numbers found experimentally ranged from Re ~ 10 to Re of several hundred. Because of the inconsistency in the literature between the theoretical predictions and the experimental observations, experiments are presented here for axisymmetric liquid-into-liquid jets to determine the critical Reynolds number at which the flow undergoes transition from laminar to turbulent flow. The question, simply asked, is the following: for a given Reynolds number, at what distance from the nozzle exit does an axisymmetric jet undergo transition from laminar to turbulent flow under normal operating conditions (i.e. when the flow is not artificially perturbed)?

3.2. Test Cell

Experiments were conducted in a tall cylindrical pyrex tank (Figure 3.1) of inside diameter D, partially filled with liquid (tap water in this study), with air occupying the region above the free surface. Water was injected into the cell through an axisymmetric nozzle of exit diameter d located at a submergence s below the free surface. Two ways

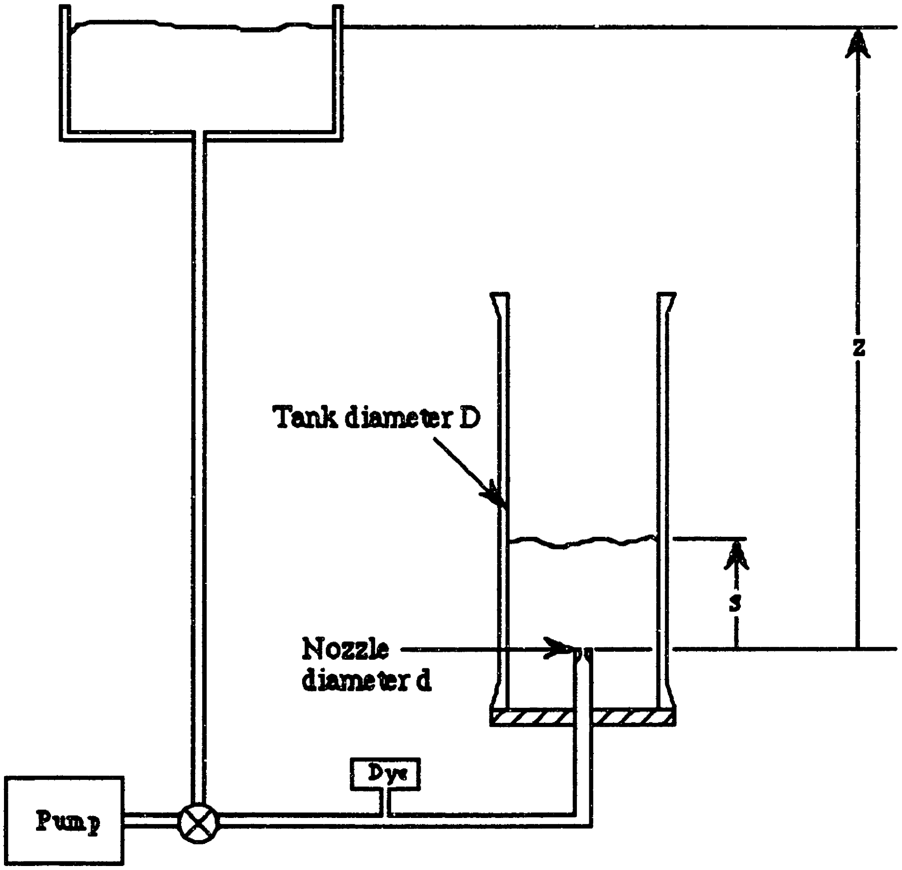

Figure 3.1. Schematic of test cell.

of injection were used: (1) with a centrifugal pump or (2) flow from a constant-head reservoir (used to avoid introducing perturbations into the flow). Artificially induced disturbances were not introduced into the flow, but no particular care was taken to try to eliminate naturally occurring external disturbances (e.g. normal vibrations in the room). The free surface was allowed to rise during a test. Writing ink (specific gravity 0.98 gm/ml) in concentrations of approximately 1% by volume was injected (for visualization purposes) into the jet just upstream of the nozzle once a statistically steady state was established. Two types of "nozzles" were used: (1) "short" nozzles and (2) long tubes with developed velocity profiles at the exit. The short nozzles had exit diameters d of 1.6 mm, 4.2 mm and 6.4 mm. These nozzles had a length to diameter of $l_n/d \sim 7$, and an inlet rounded to a radius of curvature of approximately 0.5d. For the Reynolds numbers in the current experiments, it may be expected that at the exit, the velocity had an approximately inviscid core region with thin boundary layers along the wall. To create a fully developed parabolic profile a length to diameter ratio $l_n/d \sim 0.08$ Re [White (1974)] is needed. The long tubes had diameters d of 3.2 mm and 6.4 mm and ln/d ratios of 250 and 150, respectively. Hence, the exit velocity profiles in the long tubes were fully developed for Reynolds numbers up to about 2000.

3.3. Present Experiments

The range of Reynolds numbers in the current experiments was $300 < Re_n < 7000$.

Here

$$Re_n = \frac{4Q}{\pi d \nu} \tag{3.1}$$

is the nozzle Reynolds number, where d is the nozzle diameter, ν is the liquid kinematic viscosity and Q is the volume flow rate circulating through the nozzle. The temperatures of the jet and the ambient fluid were kept equal (i.e. there were no thermal buoyancy effects). Data were taken at jet submergence s to cell diameter D ratios in the range $1 < s/D < 3$, with most of the data taken at $s/D = 1$. The jets are classified into three categories: (i) A fully laminar jet (Figure 3.2) is one that passes straight through the bulk liquid to the free surface and then diverges radially outward in a thin layer along the free surface, with very little mixing of the ambient fluid. (ii) A semi-turbulent jet (Figure 3.3) is one that passes a certain distance into the ambient fluid as a smooth jet and then breaks up into a turbulent jet. Good mixing of the ambient fluid is observed in the turbulent region of the jet. Note that the large jet spreading angle in Figure 3.3 is caused in part by the presence of the free surface. (iii) A fully turbulent jet (Figure 3.4) is one that breaks up in a distance of less than about 3d (typically in the range 0d – 3d) from the nozzle exit.

Roughly speaking, fully laminar jets were observed below $Re_n \sim 600$, semi-turbulent jets in the range $600 < Re_n < 2500$ and fully turbulent jets above $Re_n \sim 2500$. The data for the "short" nozzles are shown in Figure 3.5 plotted as a laminar length (distance from nozzle exit to the point of transition from stable to unstable flow, see Figure 3.3) vs. Re_n. Figure 3.6 shows similar data for the long tubes. The two types of nozzles gave somewhat different results. For $Re_n \sim 2000$, the long tubes yield a

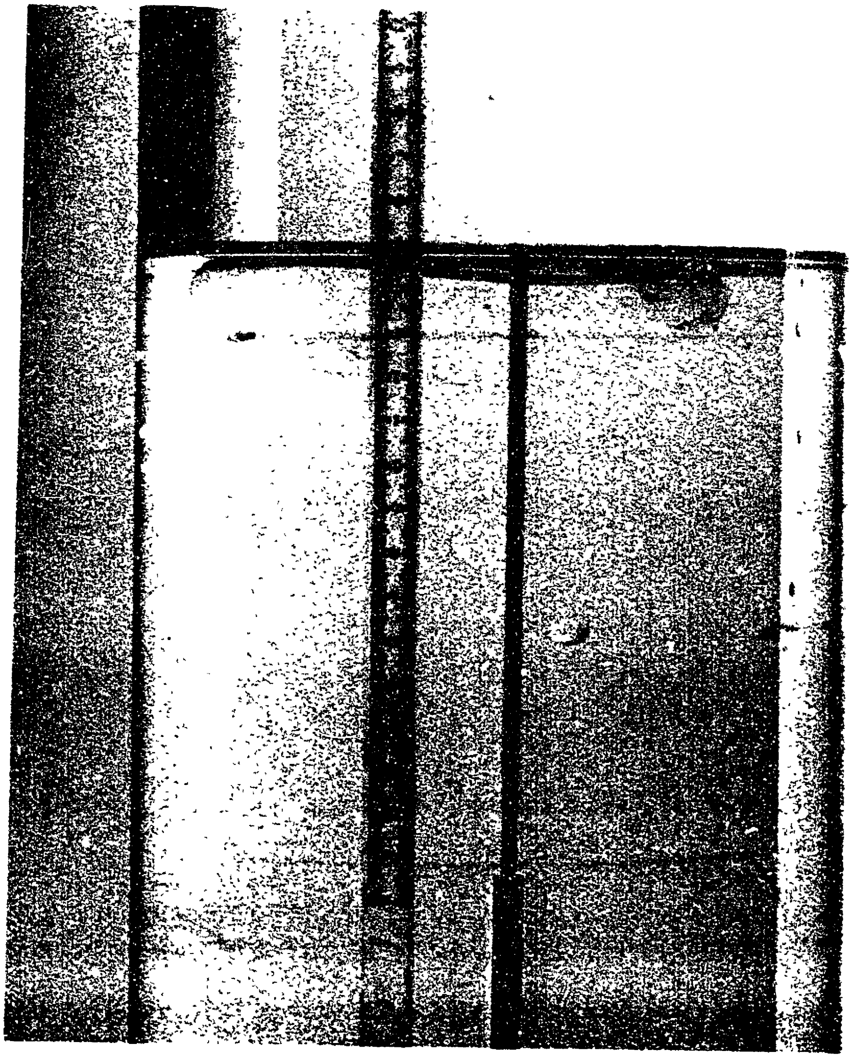

Figure 3.2. Fully laminar jet issuing from "long" nozzle with $Re_n \cong 460$, $D/d = 48$ and $s/D = 1.0$. Distance between markings on scale: 1 cm.

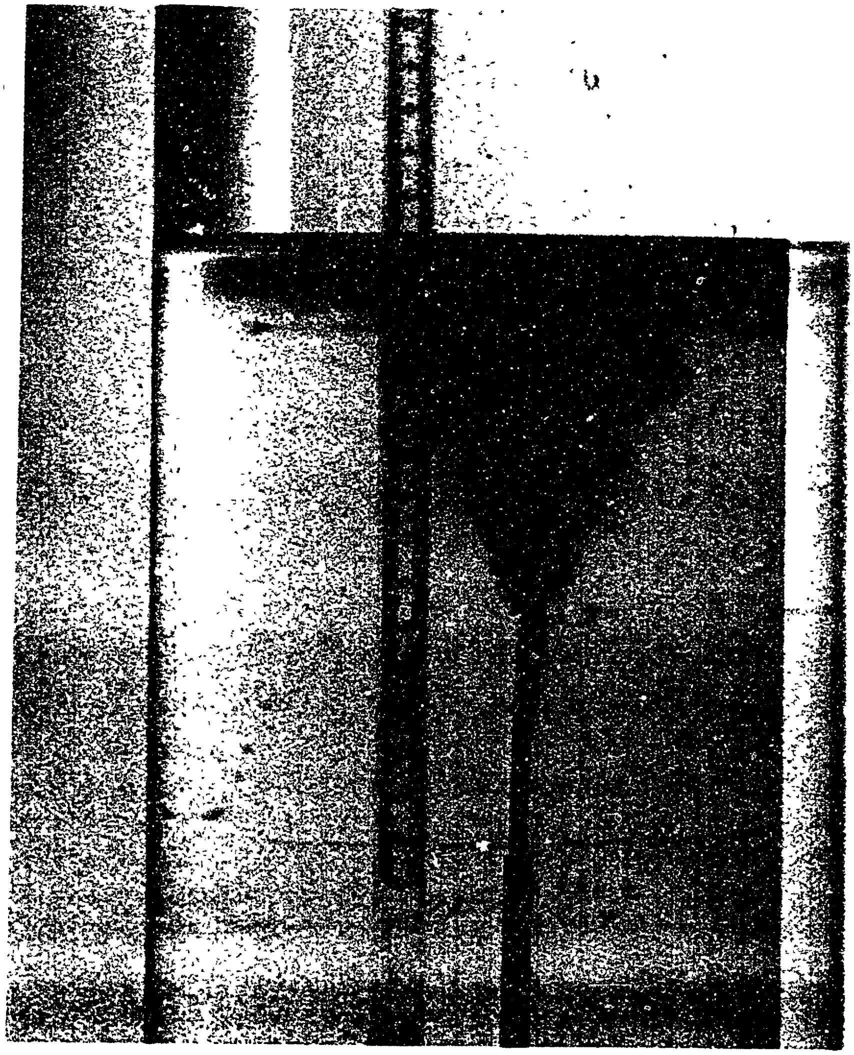

Figure 3.3. Semi-turbulent jet issuing from "long" nozzle with $Re_n \cong 1550$, $D/d = 48$ and $s/D = 1.0$. Distance between markings on scale: 1 cm.

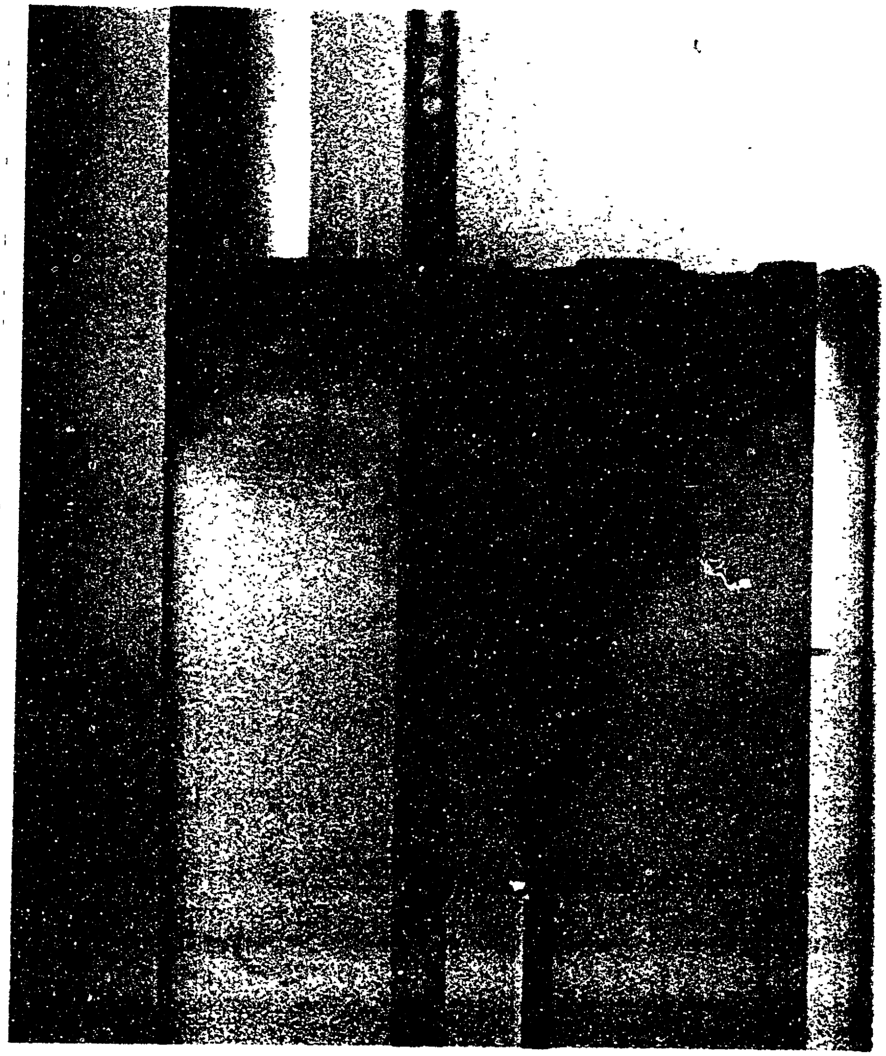

Figure 3.4. Fully turbulent jet issuing from "long" nozzle with $Re_n \cong 5980$, $D/d = 48$ and $s/D = 1.0$. Distance between markings on scale: 1 cm.

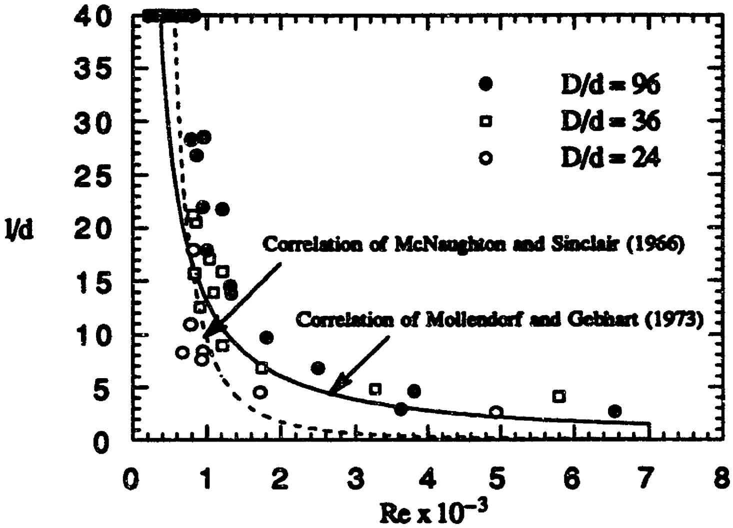

Figure 3.5. Laminar length vs Reynolds number for "short" nozzles.

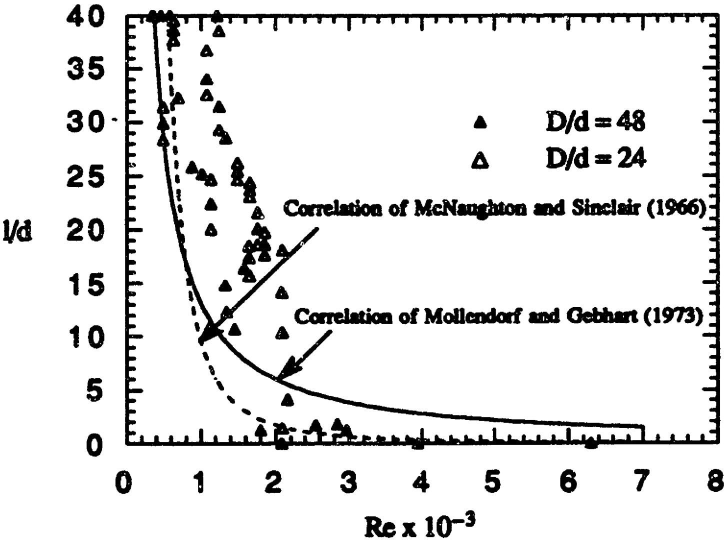

Figure 3.6. Laminar length vs Reynolds number for "long" nozzles.

laminar length of approximately 1d, whereas the short nozzles yield a laminar length of approximately 7d. The difference is attributed to the flow not being fully developed in the short nozzles. For $Re_n < 2000$, the long tubes yield a somewhat larger laminar length than do the short nozzles. This is probably due to the fact that the flow from the short nozzles had a higher velocity gradient, at the boundary between the jet and the ambient fluid, than did the flow from the long tubes. In the long tubes for $Re_n \sim 1800 - 2100$, the distance from the nozzle exit to the point where the jet broke up fluctuated between 0d and 15d at approximately 4 – 5 Hz (see Figure 2.7). Similar observations have been made over the same range of Reynolds numbers in pipe flows, where the intermittency is attributed to turbulent spots which appear in the boundary layer and then propagate into the surrounding non-turbulent fluid forming a plug of turbulent fluid [Tritton (1977)]. The plugs die out and the process then repeats itself at approximately 2 – 3 Hz [Rotta (1956)], the frequency being dependent upon the particular experiment (e.g. wall roughness, entrance region, etc.). No intermittency was, however, observed in the short nozzles. This is probably due to the boundary layers being thin and the small nozzle length being too short for the turbulent spots to form and propagate into the surrounding non-turbulent fluid.

3.4. Comparison with Other Work

Recall that the stability analysis for 2-D jets yields a critical Reynolds number of approximately 4. For the axisymmetric case, Batchelor and Gill (1962) solved the inviscid Orr-Sommerfeld equation, but their inviscid analysis did not yield a critical

Figure 3.7. Intermittency at $Re_n \cong 1990$, $D/d = 24$ and $s/D = 1.0$. Time between frames is approximately 0.25 seconds. Distance between markings on scale: 1 cm.

Reynolds number. Mollendorf and Gebhart (1973) later solved the full viscous Orr-Sommerfeld equation and determined the critical Reynolds number for the first onset of instability to be approximately 40 at a dimensionless frequency $\beta = 0.1$, where

$$\beta \equiv \frac{128\pi f l^2}{\nu \mathrm{Re}_n^3} \tag{3.2}$$

and f is the physical frequency of the disturbance and l is the distance from the nozzle exit to the point where the jet becomes unstable. The present results can not be compared directly with the calculations of Mollendorf and Gebhart since for a given fluid (ν) there are three parameters (f, l, Re_n) in equation (3.2), whereas in the current experiments only the parameters l and Re_n were investigated. For the values $\mathrm{Re}_n = 40$ and $\beta = 0.1$ given by Mollendorf and Gebhart and using $\nu = 10^{-6}$ m^2/s and d = 0.64 cm, equation (3.2) yields

$$l/d = 0.63 f^{-1/2} \tag{3.3}$$

Equation (3.2) also shows that for given β, f, ν and Re_n, l/d is inversely proportional to d, which is qualitatively consistent with the data of Figure 3.5 for Re_n less than about 1500. It is, however, difficult to draw the same conclusion from Figure 3.6 because of the scatter in the data.

The first experimental investigation of the critical Reynolds number for the axisymmetric case was conducted by Viilu (1962), who found that his jets ceased to have the expected laminar form at a Reynolds number of approximately 10. He states that the density difference between his jet and the ambient fluid was small, but does not quantify the difference. At these low Reynolds numbers, however, the buoyancy force can be large compared with the jet momentum, which may lead to the jet becoming unstable [McNaughton and Sinclair (1966)]. Reynolds (1962) conducted experiments similar to Viilu's but extended the range of Re_n to approximately 300. He observed that it was difficult to maintain a long, steady jet for $10 < Re_n < 30$, consistent with Viilu's observations, but that at higher Re_n, in the range $150 < Re_n < 300$, long (up to 3800d), steady jets could again be maintained. At $Re_n \sim 300$, however, an abrupt transition occurred that resulted in the jet becoming disordered near the nozzle. Reynolds did not exactly quantify what he meant by "near the nozzle" except to say that it was within a few centimeters. The nozzle diameter was d = 0.033 cm which implies that the length at which turbulence began in Reynolds' experiments could have been as large as several hundred nozzle diameters. (Note that the maximum nozzle submergence in the present experiments was approximately 100d, well below the stable lengths seen by Reynolds). Neither Viilu nor Reynolds provided any photographs, but gave only qualitative descriptions of the various types of jets observed. Both authors' jets were directed vertically downward along the test cell's axis, with the nozzle inserted just below the free surface.

McNaughton and Sinclair (1966) conducted similar experiments but with an apparatus that had an inlet and an outlet at the test cell's axis at opposite ends of the tank, with water entering at the bottom and exiting at the top. There was no free surface. They found fully laminar jets for $300 < Re_n < 1000$, semi-turbulent jets for $1000 < Re_n < 3000$ and fully turbulent jets for $Re_n > 3000$ in qualitative agreement with the present results. They also made the important observation that a density difference between the jet and the ambient fluid significantly affected the results at the lower Reynolds numbers ($Re_n \sim 200$). They state that positive buoyancy (the amount is not quantified) resulted in a thinning of the jet and thus to an increase in the Reynolds number. This produced semi-turbulent jets when fully laminar jets were expected. Likewise, negative buoyancy (again not quantified) resulted in buoyancy forces which dissipated the jet momentum. Their laminar length correlation is shown on Figure 3.5 and agrees reasonably well with the present data for the lower Reynolds numbers despite the different test cell geometry.

Mollendorf and Gebhart (1973) investigated the stability of positively buoyant jets issuing vertically upwards. Their data are in qualitative agreement with the present data despite the presence of positive buoyancy in their experiments, while the present data are for slightly negatively buoyant jets. Their laminar length correlation is shown on Figure 3.5 and agrees reasonably well with the present results at large Reynolds numbers but predicts a smaller laminar length at smaller Reynolds numbers. When the Reynolds number was large enough (~ 300) in their experiments, the transition point between laminar and turbulent flow was not significantly affected by the level of buoyancy in their experiments. The experiments of McNaughton and Sinclair, Mollendorf and Gebhart and the ones reported here yield roughly the same order of magnitude for the Reynolds number at which the jet becomes fully turbulent, although there is significant scatter in the data.

3.4. Conclusions

The linear stability analysis does not correctly predict the critical Reynolds number for the transition between stable and unstable flow conditions. The experimental results of Viilu (1962) and Reynolds (1962) which predicted a low critical Reynolds number were probably influenced by buoyancy forces. The current experiments show that laminar jets (with lengths over 100d) can be maintained up to Reynolds numbers of several hundred ($Re_n \sim 600$) and that fully turbulent jets, with the turbulence evident at a few nozzle diameters, occur at Reynolds numbers of $Re_n > 2500$. For the intermediate Reynolds number range, the jet passes for a certain distance (typically between about 5d and 40d) into the fluid as a smooth jet before breaking up into a fully turbulent jet. Figures 2.5 and 2.6 summarize the results.

References

Batchelor, G.K. and Gill, A.E., "Analysis of the Stability of Axisymmetric Jets," *J. Fluid Mech*, Vol. 14, pp. 529-551, 1962.

Clenshaw, C.W. and Elliott, D., "A Numerical Treatment of the Orr-Sommerfeld equation in the Case of a Laminar Jet," *Quart. J. Mech. Appl. Math.*, Vol. 13, pp. 300-313, 1960.

Curle, N., "On Hydrodynamic Stability in Unlimited Fields of Viscous Flow," *Proc. Roy. Soc. London A*, Vol. 238, pp. 489-501, 1957.

Howard, L.N., "Hydrodynamic Stability of a Jet," *J. Math. Phys.*, Vol. 37, pp. 283-298, 1958.

McNaughton, K.J. and Sinclair, C.G., "Submerged Jets in Short Cylindrical Flow Vessels," *J. Fluid Mech.*, Vol. 25, pp. 367-375, 1966.

Mollendorf, J.C. and Gebhart, B., "An Experimental and Numerical Study of the Viscous Stability of a Round Laminar Vertical Jet with and without Thermal Buoyancy for Symmetric and Asymmetric Disturbances," *J. Fluid Mech.*, Vol. 61, pp. 367-399, 1973.

Reynolds, A.J., "Observations of a Liquid-Into-Liquid Jet," *J. Fluid Mech.*, Vol. 14, pp. 552-556, 1962.

Rotta, J., "Experimenteller Beitrag zur Entstehung Turbulenter Stromung im Rohr," *Ingenieur–Archiv*, Vol. 24, pp. 258-281, 1956.

Tritton, D.J., *Physical Fluid Dynamics*, Van Nostrand Reinhold Co., New York, 1977.

Sato, H. and Sakao, F., "An Experimental Investigation of the Instability of a Two-Dimensional Jet at Low Reynolds Numbers," *J. Fluid Mech.*, Vol. 20, pp. 337-352, 1964.

Tatsumi, T. and Kakutani, T., "The Stability of a Two-Dimensional Laminar Jet," *J. Fluid Mech.*, Vol. 4, pp. 261-275, 1958.

Viilu, A., "An Experimental Determination of the Minimum Reynolds Number for Instability in a Free Jet," *J. Applied Mech.*, Vol. 29, pp. 506-508, 1962.

White, F.M., *Viscous Fluid Flow*, McGraw-Hill, New York, 1974.